

NASA/CR—2010-216329



Aerodynamic Design and Computational Analysis of a Spacecraft Cabin Ventilation Fan

Daniel L. Tweedt
AP Solutions, Inc., Solon, Ohio

December 2010

NASA STI Program . . . in Profile

Since its founding, NASA has been dedicated to the advancement of aeronautics and space science. The NASA Scientific and Technical Information (STI) program plays a key part in helping NASA maintain this important role.

The NASA STI Program operates under the auspices of the Agency Chief Information Officer. It collects, organizes, provides for archiving, and disseminates NASA's STI. The NASA STI program provides access to the NASA Aeronautics and Space Database and its public interface, the NASA Technical Reports Server, thus providing one of the largest collections of aeronautical and space science STI in the world. Results are published in both non-NASA channels and by NASA in the NASA STI Report Series, which includes the following report types:

- **TECHNICAL PUBLICATION.** Reports of completed research or a major significant phase of research that present the results of NASA programs and include extensive data or theoretical analysis. Includes compilations of significant scientific and technical data and information deemed to be of continuing reference value. NASA counterpart of peer-reviewed formal professional papers but has less stringent limitations on manuscript length and extent of graphic presentations.
- **TECHNICAL MEMORANDUM.** Scientific and technical findings that are preliminary or of specialized interest, e.g., quick release reports, working papers, and bibliographies that contain minimal annotation. Does not contain extensive analysis.
- **CONTRACTOR REPORT.** Scientific and technical findings by NASA-sponsored contractors and grantees.

- **CONFERENCE PUBLICATION.** Collected papers from scientific and technical conferences, symposia, seminars, or other meetings sponsored or cosponsored by NASA.
- **SPECIAL PUBLICATION.** Scientific, technical, or historical information from NASA programs, projects, and missions, often concerned with subjects having substantial public interest.
- **TECHNICAL TRANSLATION.** English-language translations of foreign scientific and technical material pertinent to NASA's mission.

Specialized services also include creating custom thesauri, building customized databases, organizing and publishing research results.

For more information about the NASA STI program, see the following:

- Access the NASA STI program home page at <http://www.sti.nasa.gov>
- E-mail your question via the Internet to help@sti.nasa.gov
- Fax your question to the NASA STI Help Desk at 443-757-5803
- Telephone the NASA STI Help Desk at 443-757-5802
- Write to:
NASA Center for AeroSpace Information (CASI)
7115 Standard Drive
Hanover, MD 21076-1320

NASA/CR—2010-216329



Aerodynamic Design and Computational Analysis of a Spacecraft Cabin Ventilation Fan

Daniel L. Tweedt
AP Solutions, Inc., Solon, Ohio

Prepared under Contract NNC06BA07B, Task 190

National Aeronautics and
Space Administration

Glenn Research Center
Cleveland, Ohio 44135

December 2010

Acknowledgments

Final report submitted to ASRC Aerospace Corporation for purchase order number AS6461, NASA Glenn Research Center prime contract number NNC06BA07B, Task 190. The author would like to thank Dr. Rodrick V. Chima of the NASA Glenn Research Center for the many helpful discussions regarding computational fluid dynamics code development and application.

Trade names and trademarks are used in this report for identification only. Their usage does not constitute an official endorsement, either expressed or implied, by the National Aeronautics and Space Administration.

Level of Review: This material has been technically reviewed by expert reviewer(s).

Available from

NASA Center for Aerospace Information
7115 Standard Drive
Hanover, MD 21076-1320

National Technical Information Service
5301 Shawnee Road
Alexandria, VA 22312

Available electronically at <http://gltrs.grc.nasa.gov>

Aerodynamic Design and Computational Analysis of a Spacecraft Cabin Ventilation Fan

Daniel L. Tweedt
AP Solutions, Inc.
Solon, Ohio 44139

Abstract

Quieter working environments for astronauts are needed if future long-duration space exploration missions are to be safe and productive. Ventilation and payload cooling fans are known to be dominant sources of noise, with the International Space Station being a good case in point. To address this issue in a cost-effective way, early attention to fan design, selection, and installation has been recommended. Toward that end, NASA has begun to investigate the potential for small-fan noise reduction through improvements in fan aerodynamic design. Using tools and methodologies similar to those employed by the aircraft engine industry, most notably computational fluid dynamics (CFD) codes, the aerodynamic design of a new cabin ventilation fan has been developed, and its aerodynamic performance has been predicted and analyzed. The design, intended to serve as a baseline for future work, is discussed along with selected CFD results.

Introduction

Quieter working environments for astronauts are needed if future long-duration space exploration missions are to be safe and productive. Ventilation and payload cooling fans are known to be dominant sources of noise, with the International Space Station being a good case in point. Noise management by using externally applied mechanisms, such as surface acoustic treatments and mufflers, is common and effective, but tends to be costly in terms of subsystem performance and weight (Refs. 1 and 2). To address this issue in a cost-effective way, early attention to fan design, selection, and installation has been recommended.

The work described herein is part of a larger effort by NASA to examine the potential for small-fan noise reduction through improvements in fan aerodynamic design. Prior work, considered preliminary to the current task, involved a detailed computational analysis of a spacecraft cabin ventilation fan designed by Hamilton Sundstrand. That fan, designated here as the reference fan, was numerically simulated using computational fluid dynamics (CFD) codes, for the purpose of examining and quantifying various aspects of its aerodynamics and performance (Ref. 3). Most of the investigation was done for the design operating condition, although some off-design flow rates were also simulated.

The current task involves the aerodynamic design of a new cabin ventilation fan complying with the same requirements as specified for the reference fan, with the goal of improving aerodynamic and acoustic performance. In this context, aerodynamic performance is seen as affecting acoustic performance, largely through the generation of broadband noise. Using tools and methodologies similar to those employed by the aircraft engine industry, most notably CFD codes, a successful design has been developed, and its aerodynamic performance has been predicted and analyzed. The new design will serve as a baseline for future research and development, including possible use as a test bed for investigating noise-reduction concepts.

This report presents basic information about the new fan design along with selected CFD results. An extensive and detailed comparison with the reference fan design is beyond the scope of this presentation, so such comparisons are minimal, being limited to relevant design parameters, constraints, and some overall performance quantities.

Fan Design Methodology

The general process employed for the aerodynamic design of the new fan involved two basic steps that were iterated until a satisfactory design was achieved. In the first step, a candidate fan design was generated using a modified version of a NASA-developed compressor design program (Ref. 4) called NCDP. Then, as the second step, the design was analyzed and assessed using CFD methods. Examination and interpretation of the CFD results provided the information needed to adjust the NCDP input to better reflect the aerodynamic performance characteristics of the fan and to advance the design toward the design objectives. Input quantities such as the hub and tip endwall contour coordinates, annulus area blockages, blade-row loss coefficients, blade-row aerodynamic solidity distributions, blade incidence and deviation angles, and blade profile shapes as specified by chordwise camber angle and thickness distributions, were updated based on the CFD results. Adjustments to the hub and tip endwall contours and the annulus area blockages were made in early iterations of the design, with the related streamwise variations in meridional flow area indirectly controlled by these adjustments.

Progress on the design was based on reasonable and experienced aerodynamic interpretations of the CFD results, and on the appropriate incorporation of that information back into the design so as to improve performance while maintaining acceptable operating characteristics. Convergence to the final design was fairly rapid, and was not overly sensitive to small changes in the design input variables.

Preliminary and intermediate design activity involved some exploratory work aimed at narrowing the design space by eliminating various ideas and establishing or confirming ranges for several of the design parameters. For example, a shrouded rotor was examined and found to be vastly inferior to a standard (unshrouded) rotor with a rotating tip clearance. Most of the intermediate design work, where the rotor and stator blade row designs were being refined, involved CFD simulations for each blade row separately, thereby facilitating and expediting the design process. As the design was being finalized, however, the entire integrated fan system was aerodynamically simulated; that is, all system components were coupled together for aerodynamic simulations at the operating conditions of interest.

Structural and aeroelastic analyses were not performed on the final design, at least not as of the time of this report. It was considered unnecessary for a couple of reasons; namely, the rotor tip speed is relatively low (less than 175 ft/sec), and the fabrication material is aluminum. Compared to the reference Hamilton Sundstrand design, the tip speed is significantly lower, while blade structural qualities such as thickness and camber are generally similar, if not enhanced. Since the reference fan is a production design, it is presumed to be structurally and aeroelastically acceptable. The new fan is expected to have stiffer blades, with entirely negligible deflection magnitudes, and to have material stress levels that are well below acceptable limits.

Fan Aerodynamic Design

The aerodynamic design of the new fan involved two fundamental approaches that reflect the basic design philosophy and provided direction in the design process. The first is low rotational speed, ideally the lowest possible speed needed to achieve the design flow and pressure rise, while maintaining good aerodynamic performance and acceptable operating margins. The second is adherence to aerodynamically clean (streamlined) flow path contours, not only within the fan, but also both upstream and downstream of it (Ref. 5).

Low rotational speed is expected to minimize mechanical (electric motor) noise, as well as broadband aerodynamic noise. The anticipated benefit for broadband noise is related to lower relative velocities through the rotor blade row, although any such benefit is realizable only if blade aerodynamic loading is held to a reasonable level. Blade surface boundary layer separations of significant magnitude and/or extent could easily offset any gains, as could an excessively strong rotor tip clearance gap generated flow and vortex.

In general, designing for a lower rotational speed tends to increase blade loading for both the rotor and stator. To offset this in the rotor, the through-flow area in the streamwise direction was contracted,

unloading the blade row by decreasing its static pressure rise. The contraction was achieved by increasing the area at the rotor inlet, rather than decreasing it at the exit. The rotor blade loading was also reduced by increasing its aerodynamic solidity (ratio of blade chord length to blade tangential spacing) over most of the span, but especially at the tip. Similarly, stator blade loading was controlled by increasing the aerodynamic solidity over its entire span.

Several design parameters and constraints for the new design were taken from the reference design. These included the volumetric flow rate of 150.3 ft³/min at 70 °F and 14.7 psia, the system total-pressure rise of 3.64 in. of water, the rotor tip clearance of 0.009 in., and the device overall size envelope. For the total-pressure rise specification, the system is defined as including the fan, a flow straightener upstream of the fan, a flow diffuser downstream of the fan, and a flow discharge at the exit of the diffuser where the centerbody is truncated. The overall size envelope for the fan system is a cylinder 9 in. long and 4 in. in diameter.

Preliminary design studies indicated that, compared to the reference fan, a substantial reduction in fan rotational speed would be achievable, possibly as much as 30 percent.¹ Further work resulted in the selection of 12 000 rpm as the design speed at 70 °F, which is 75 percent of the reference fan design speed. The corresponding blade-tip speed is 165 ft/sec at the rotor inlet, and 173 ft/sec at the rotor exit. Specific speed, N_s , is a dimensionless parameter commonly used for selecting the appropriate type of fan for a particular application. It can be defined as $N\sqrt{Q}/(\Delta p_t/\rho)^{3/4}$, where N is rotational speed, Q is volumetric flow rate, Δp_t is the total-pressure rise, and ρ is the fluid density (Ref. 6). Although specific speed is dimensionless when a consistent unit system is used in its evaluation, it is typically expressed in dimensional form. For the new fan design, the dimensionless value of specific speed is 2.36, which corresponds to a value of 6450 in U.S. customary units (rpm $\sqrt{\text{gpm}/\text{ft}^{3/4}}$). This value falls in the middle of the range normally associated with mixed-flow fan designs.² For the reference design, the specific speed in U.S. customary units is 8600, which falls at the high end of the mixed-flow range, and at the low end of the axial-flow range.

The number of rotor blades is the same as for the reference design and was determined by the desired blade-row axial length of nominally 0.7 in. in conjunction with the aerodynamic solidity values needed for the amount of aerodynamic loading. Note that the axial length was taken from the reference design at the hub. Formally specified as NCDP input were the number of blades, equal to nine, the rotor tip solidity with a value of 0.975, and the spanwise distribution of blade chord length normalized by blade chord length at the tip. A linear chord-length distribution was specified, with the hub chord 15 percent shorter than the tip chord. The resulting nominal blade chord length is 1.05 in., and the blade aspect ratio is 0.61.

The number of stator blades, equal to eleven, is also the same as for the reference design. This number was determined from an analysis performed by Koch (Ref. 7) at the NASA Glenn Research Center, using Tyler-Sofrin and Sofrin-Mathews relations to evaluate the acoustic modes for rotor/stator interaction tone noise (Refs. 8 and 9). Stator axial length was not constrained, and stator chord length was specified as uniform from hub to tip, with a stator tip solidity of 1.15. The resulting blade chord length is 1.15 in., and the blade aspect ratio is 0.39. The axial location of the stator is similar to that of the reference design, but was adjusted to maintain a reasonably large rotor/stator blade-row spacing. At midspan the blade-row spacing is 1.40 in., which is equal to 1.94 meridional-chord lengths of the rotor blade.

A uniform spanwise distribution of total-pressure loss coefficient was specified in the NCDP input for each blade row. For the rotor, a value of 0.05 was used, which matched CFD results over most of the span, excluding the tip region (outer 20 percent of span) where the computed losses were relatively much larger. For the stator, a value of 0.10 was used as a representative-average value based on CFD results. Annulus area blockages were also input, with an unexpectedly large value needed at the rotor exit. The blockage there is critical because it has a large impact on rotor blade camber, and therefore on rotor work. At the rotor trailing edge station, the total area-blockage was determined from CFD analysis to be about 18.5 percent,

¹Reference fan design rotational speed is 16 000 rpm at 70 °F.

²As summarized in Reference 6, the approximate specific speed range for efficient mixed-flow designs is between 4000 and 9000, in U.S. customary units.

which for the NCDP input was distributed as 1.0 percent hub blockage, 5.5 percent tip blockage, and 12.0 percent circumferential blockage. Note that this high blockage is thought to be a low-Reynolds-number effect, related to the laminar viscous flow in and around the blade tip clearance. Less critical, but still important, were the blockages at the rotor inlet (0.5 percent hub and 1.0 percent tip), and at the stator inlet and exit (2.5 percent hub, 4.0 percent tip, and 1.5 percent circumferential).

Spanwise distributions of diffusion factor, a parameter commonly used to quantify blade aerodynamic loading, are part of the NCDP standard output for each blade row. Similar distributions were also calculated from the CFD solutions; they are considered more accurate and will be presented later in graphical form along with other CFD results. In general, the NCDP- and CFD-based distributions are roughly the same, except in the rotor tip region where the computed diffusion factors, like the total-pressure losses, are relatively much larger. Rotor diffusion factor values range from around 0.10 at the hub to 0.37 near the tip, excluding the tip region, and stator diffusion factor values range from around 0.43 at the hub to 0.38 at the tip. By conventional standards these values represent low to moderate aerodynamic loading, but at the relatively low Reynolds numbers associated with the small fan size and flow velocities, the aerodynamic loading is effectively higher. Much of the boundary layer flow is laminar at these conditions, and laminar boundary layers, as is well known, are much less resistant to separation during diffusion³ than are turbulent boundary layers. Also, when transition to turbulence does occur in the boundary layer, it tends to occur more gradually, and the resulting turbulence (eddy) viscosity levels tend to increase more slowly. Furthermore, at these conditions the boundary layers, laminar and turbulent, are thicker relative to the geometric length scale.

A drawing of the fan system flow path is shown in Figure 1, which also depicts the blade row locations. Apparent is the substantial annulus area contraction through the rotor blade row, with the through-flow area decreasing almost linearly by about 22 percent. Rotor aerodynamic loading is reduced by this contraction, as discussed earlier, and also by the increasing radius from rotor inlet to exit, especially at the hub where the slope angle is initially 30°. The positively sloping hub contour also integrates well the fan inlet. These features are generally consistent with the specific speed of 6450, and correspond to an intermediate type of rotor that could be classified as either mixed-flow or axial-flow.

Immediately downstream of the rotor, the through-flow area decreases by another 6 percent before becoming constant in and through the stator. Contraction of the flow path within the stator blade row was not necessary, and would not have been beneficial from a system standpoint since any reduced flow diffusion (static pressure rise) in the stator would need to be compensated for by more diffusion downstream of the stator. The fan exit diffuser, consisting of a long, gradually diverging duct downstream of the stator, utilizes all of the remaining length available to the fan system to maximize static pressure recovery. The diffuser was designed to decelerate the flow as much as possible, while maintaining attached boundary layers, before dumping into a tubular section that begins at the location where the hub/centerbody is truncated. It should be noted that the hub surface in the stator and diffuser was maintained at radii larger than that of the reference fan to ensure adequate room for the electric drive motor.

In the NCDP design program, blade element and section shapes are laid out on conic surfaces and are specified by chordwise polynomial functions for camber angle and blade thickness. The functional distributions consist of two segments, each with its own polynomial of degree four or less, with the polynomials joined at specified chordwise locations. The thickness distribution polynomial involves a special square-root term that forces the first derivative to be zero at the transition point where the polynomials join, thus locating the maximum thickness there. For the current fan design, all elements of the rotor and stator blades have the transition point for both the camber-angle and thickness distributions located at 35 percent of blade chord. First degree (linear) camber-angle distributions were used for the rotor polynomial segments, giving double circular arc camber-angle distributions, and third-degree camber-angle polynomials were used for the stator polynomial segments. Fourth-degree polynomials were used for all thickness polynomial segments.

³Diffusion is synonymous with flow deceleration accompanied by increasing static pressure. Flow diffusion and aerodynamic loading are related concepts.

Drawings of several rotor and stator blade section profiles are shown in Figure 2. The profiles were generated using an orthographic projection in the blade stacking direction, and only two stator section profiles are shown for the sake of clarity. The stator tip profile (not shown) is almost the same as the hub profile.

The rotor blade maximum thickness was specified as 10 percent of blade chord at the hub, decreasing linearly to 8 percent of blade chord at the tip. Note, however, that since the hub chord was specified to be 15 percent shorter than the tip chord, the actual blade thickness decrease from hub to tip is fairly small. The maximum thickness for the stator blade was specified as 10 percent of blade chord for all elements. Leading and trailing edge radii were also specified as a fraction (discussed here as a percent) of blade chord for the rotor and stator blade rows. The leading edge shape is elliptical, with an ellipse aspect ratio reciprocal of 3.0 for the rotor blade and 2.5 for the stator blade, and with the specified edge radius corresponding to the minimum radius-of-curvature on the ellipse. The trailing edge shape is circular for both blade rows. At the rotor tip the leading and trailing edge radii are 0.500 and 0.625 percent, respectively, increasing linearly to 1.00 and 1.25 percent, respectively, at the hub. The stator leading and trailing edge radii are 1.00 and 1.50 percent, respectively, for all blade elements.

Graphs showing several design-related blade parameters are presented in Figure 3, which shows spanwise distributions of normalized chord length, aerodynamic solidity, blade incidence angle, and blade deviation angle. Spanwise distributions of blade leading edge (LE) and trailing edge (TE) angles are shown in Figure 4. Note that the incidence and deviation angle distributions were those specified as input to NCDP, and that they were used along with the internally generated streamline curvature through-flow solution to calculate the blade leading and trailing edge angles. They do not necessarily represent the actual incidence and deviation angle distributions, however, as may become apparent later when CFD solution results are discussed. Noteworthy in this regard is the relatively large variation in stator incidence near the tip. The specified incidence reduction substantially improves the actual incidence there by providing better blade alignment with the flow. Such an indirect approach to incidence matching was necessary because the highly nonuniform spanwise flow variations generated by the rotor tip are not modeled in the NCDP through-flow solution.

Blade camber-angle and thickness distributions for the rotor and stator are shown in Figures 5 and 6, respectively. Five blade sections, equally spaced in the spanwise direction, are represented for the rotor, but for the stator only the midspan section is represented since the other section distributions are similar when appropriately normalized. The geometric data used for these graphs, as well as those in Figures 3 and 4, were reverse-engineered from the final blade geometries, rather than being taken directly from the NCDP standard input or output. This was done for a couple of reasons. First, it facilitates and improves any future comparisons with other blade geometries, especially ones not generated using NCDP. It does this by allowing a standardized method for extracting the geometric information; that is, the same procedure can be applied to every blade, regardless of source. Second, the geometric properties so obtained more generically characterize the final geometry, because none of the assumptions and peculiarities inherent to a particular design system are embedded in them. For example, the NCDP program lays blade elements out on conic sections, even though the endwalls and aerodynamic stream surfaces are generally curved. Therefore, a blade designed using double circular arc camber-angle distributions, such as the rotor blade (see Fig. 5, top graph), will not appear to conform exactly to that specification when the camber-angle distributions are reversed engineered using the naturally existing curved surfaces (of revolution). This effect can be most clearly seen in the camber-angle distribution at the rotor hub.

A computer-generated, three-dimensional picture of the entire fan system, excluding the inlet flow straightener, is shown in Figure 7. A small gap in the hub downstream of the rotor indicates where the rotating hub ends and the stationary hub begins. This location is also indicated in Figure 1 by a vertical dashed line below the hub contour, at axial coordinate -0.150 in. Because the size of the gap is not exactly specified for the aerodynamic design, this coordinate should be interpreted as the location where the stationary surface begins.

The inlet flow straightener (not shown) is located just upstream of the fan inlet, where the outer duct wall (shown as a transparent surface in Fig. 7) ends. In the coordinate system of Figure 1, the downstream

side of the straightener is located at axial coordinate -2.000 in. For the results presented herein, the straightener is assumed to be the same as that in the reference system, where it consists of a honeycomb structure with an effective flow path diameter of 3.50 in., a thickness of 0.9375 in., and a cell size (or center-to-center cell spacing) of 0.1875 in.

Computational Fluid Dynamics

Two different CFD codes were used to simulate the airflow through the fan system: an axisymmetric viscous solver, called AVCS, and a three-dimensional viscous turbomachinery solver, called TSWIFT. Multiple solution domains (grid blocks) were used, with axisymmetric solutions coupled to three-dimensional solutions at mixing-planes by means of a separate computer program, called SMPI, developed as a companion program for AVCS and TSWIFT. SMPI was also used to couple rotating and stationary three-dimensional solutions together at mixing-planes. In general, the three-dimensional TSWIFT solver was used for computational domains in and near blade rows, and the axisymmetric AVCS solver was used for computational domains upstream and downstream of the fan, sufficiently far away from the blade rows.⁴

The AVCS and TSWIFT codes use similar numerical algorithms; both solve the Reynolds-averaged Navier-Stokes equations on body-fitted grids using an explicit, finite-difference scheme. The codes include viscous terms in all grid directions, except that TSWIFT neglects the mixed-derivative viscous terms containing derivatives in the predominantly streamwise grid direction. The discretized equations are solved with a multistage Runge-Kutta time-marching scheme using a spatially varying time step, implicit residual smoothing, and preconditioning (Refs. 10 to 13). All simulations discussed herein were run using a two-stage Runge-Kutta scheme with a CFL (Courant-Friedrichs-Lewy) number of 2.5, and using the H-CUSP (convective upwind split pressure) upwind scheme (Refs. 14 and 15). Another upwind scheme, the AUSM+ (advection upstream splitting method) scheme (Ref. 16), was also optionally available. Although considered generally superior with respect to solution accuracy, it proved to be unsuitable for simulations of the reference fan because of laminar, free shear-layer instabilities in the rotor solutions (Ref. 3). Therefore, for reasons related to computational consistency, it was necessary to use the H-CUSP scheme for the current fan.⁵

The TSWIFT code was derived from and has the same basic features as the SWIFT code (Ref. 17) developed by Chima at the NASA Glenn Research Center. TSWIFT also has a fairly general multiblock capability (when used with SYNCEX; see preceding footnote), includes the two-equation SST (shear stress transport) turbulence model developed by Menter (Ref. 18), and implements Giles' two-dimensional, steady-state, nonreflecting boundary conditions (Refs. 19 and 20) at flow inlet, exit, and mixing-plane boundaries.⁶ When a two-equation turbulence model is used, either the Wilcox k - ω model (Ref. 21) or the Menter SST model, the turbulence kinetic energy, k , and the ratio of turbulence kinetic energy to turbulence dissipation, k/ω , are circumferentially mass-averaged at mixing-planes (on the upstream side to determine average values of k and ω for the downstream side).

For Mach number levels below about 0.3 it becomes necessary to use preconditioning, sometimes referred to as artificial compressibility, to obtain good solution convergence. The preconditioning can also be used at higher Mach numbers, however, and typically is because it has been found to generally improve convergence behavior. Mach number levels in the current fan system are nominally around 0.1 or less, except in the rotor where blade tip relative Mach numbers exceed 0.2.

⁴All program-to-program communications, for mixing-planes and direct block-to-block interfaces, were handled using a facility called SYNCEX (pronounced sink-ex). SYNCEX is a message-passing interface that enables two or more executing programs to efficiently exchange data on a single computer and/or over a network.

⁵A simulation of the current fan was also performed using the AUSM+ scheme. The resulting solution was similar to that obtained using the H-CUSP scheme, although the AUSM+ solution indicated slightly better aerodynamic performance.

⁶The SMPI code also implements Giles' two-dimensional, steady-state, and nonreflecting boundary conditions.

Initial solution results revealed that it was also necessary to use double precision for CFD solver execution. Single precision was sufficient for grid generation, solution preprocessing, and solution postprocessing, but proved inadequate for solver execution because of truncation errors in density and pressure. In general, as Mach number levels approach zero, the dimensionless density and pressure each approach a constant positive value with an order of magnitude of one. The resulting flow-field solutions involve relatively small spatial variations in density and pressure, such that property differences computed in single precision are significantly affected by the truncation error.

Fan System Aerodynamic Simulations

The aerodynamic simulations were performed for air modeled as a perfect gas with a ratio of specific heats, γ , equal to 1.400, and with inlet total (stagnation) flow conditions set at standard day sea-level (SSL) values. Since a nonstandard inlet temperature was specified for the design, it was necessary to apply a correction to values of rotational speed, volumetric flow rate, and unit Reynolds number in order to maintain aerodynamic similarity. The SSL-corrected values were used as input data for the CFD solver, and are now being used for standardized data presentations and comparisons. For the inlet total temperature of 70 °F, the total-temperature correction factor, θ , is equal to 1.0218. Note that a total-pressure correction is not necessary since, for an inlet total pressure of 14.7 psia, the total-pressure correction factor, δ , is equal to 1.0000. Applying the temperature correction gives a design rotational speed, $N/\sqrt{\theta}$, of 11 871 rpm, a design flow rate, $Q/\sqrt{\theta}$, of 148.7 ft³/min, and a unit Reynolds number based on inlet total conditions, $(\rho c/\mu)_{SSL} \delta/\theta^{7/6}$, of 5.768×10^5 in.⁻¹, where ρ is density, c is the speed of sound, and μ is dynamic viscosity.

Inlet conditions are specified for the fan system at the upstream side of the inlet flow straightener. The inlet computational domain, however, begins at the downstream side, so the total pressure at the computational boundary must include the pressure loss of the straightener. The total-pressure drop across the straightener was calculated from the average upstream flow velocity using an empirical correlation provided by Hamilton Sundstrand. For the design flow rate of 150.3 ft³ at 70 °F, the calculated pressure drop is 0.0735 in. of water. The corresponding total-pressure ratio for the straightener is 0.999819, which is the value used as input to the CFD solver. Note that this value was used even though the SSL-corrected design flow rate is slightly different. It was also used for the off-design flow rates that differ from the design value by several percent.

The effects of turbulence were modeled using the Wilcox $k-\omega$ turbulence model (Ref. 21), with free-stream turbulence at the upstream computational boundary set at 1.0 percent, along with a turbulence (eddy) viscosity equal to 0.5 times the molecular viscosity. The corresponding turbulence kinetic energy is 1.68×10^{-7} (dimensionless; multiply by the reference speed of sound squared to obtain a dimensional value). Two versions of the model were applied, a high-Reynolds-number version and a low-Reynolds-number version, the latter being considered more appropriate and accurate for the cases being computed. The high-Reynolds-number model is known to simulate the onset of transition much too soon, which could potentially have a significant impact on the simulation results at such low Reynolds numbers when blade chord Reynolds numbers are on the order of 75 000 for the rotor, and 60,000 for the stator. Applying both models allows an assessment to be made of the relative importance of this effect. Note that both models were applied only for the design flow rate and tip clearance; for all other cases the low-Reynolds-number model was used.

For computational efficiency, the fan solution and the discharge flow field at the fan system exit were computed separately; that is, the exit discharge solution was not close-coupled to the fan solution. Both computational domains include most or all of the annular diffuser duct, so there is a large overlap region. The fan solution, the domain of which terminates at the exit of the annular duct, was computed first. Then, the corresponding solution for the exit discharge region was computed, with the fan solution providing upstream boundary values for the exit discharge domain. Both solutions involved setting the desired flow rate at the respective exit boundary, with the tip static pressure automatically adjusted at each iteration, and simple radial-equilibrium solved to determine the radial static-pressure distribution. The exit region

solution mainly provides computational total-pressure loss results for the discharge flow, as well as information about the extent of the separation (reverse flow) bubble downstream of the truncated diffuser centerbody.

Computational Grids

A meridional view of several fan system grid blocks is shown in Figure 8, where different colors are used to differentiate nine different blocks. Note that for clarity, only every other grid line has been drawn for each grid. The blue and light-blue colored blocks on the far left in the inlet duct, and the blue colored block on the far right in the annular diffuser duct, are two-dimensional/axisymmetric H-grids. The location of the far left boundary corresponds to the downstream side of the inlet flow straightener, and the lower boundary of the light-blue colored inlet block is on the fan centerline. The two black colored blocks represent three-dimensional blade-row C-grids, one on the left for the rotor, and the other on the right for the stator. The two green colored blocks represent three-dimensional H-grids that extend the rotor domain upstream and downstream, and the two red colored blocks represent three-dimensional H-grids that extend the stator domain upstream and downstream. Not indicated in the figure is a rotor tip clearance gap O-grid block.

The system exit domain contains three two-dimensional/axisymmetric grid blocks, shown in Figure 9. The front part of the blue colored block, the part located within the annular diffuser duct, is identical to the grid used for the fan system (see Fig. 8, blue grid block on right). The lower boundary of the light-blue colored base grid and the violet colored downstream extension tube grid is on the fan centerline.

Both of the inlet duct grid blocks were generated using a Poisson partial differential equation (PDE) solver, otherwise known as an elliptic grid generator, which produces grids with good boundary-normal node clusterings and spacings, and generally good local orthogonality. The annular diffuser duct and system exit grid blocks were generated using an algebraic method since the grid lines are naturally orthogonal, or nearly so.

The blade-row grids, except for the rotor exit and stator exit H-grid blocks, were generated using a computer program called TTGRID, which is a modified version of TCGRID (Ref. 22), a three-dimensional grid generator for turbomachinery developed by Chima at the NASA Glenn Research Center. TTGRID applies an elliptic PDE solver to the streamwise-pitchwise (blade-to-blade) mesh surfaces of blade-row C- and H-grids.

A three-dimensional view of the rotor grid is shown in Figure 10. Note that the (green colored) upstream/inlet H-grid overlaps the (black colored) C-grid and has node-to-node alignment with it. The (green colored) downstream/exit H-grid also overlaps the C-grid, but the grid nodes are not aligned. An axial-circumferential (blade-to-blade) mesh plot of the rotor grid at the blade tip is shown in Figure 11(a), which also includes magnified views of the blade leading and trailing edge regions. The tip clearance gap O-grid block, colored light gray, overlaps the C-grid with node-to-node alignment. A circumferential-radial view of the tip clearance grid at a midchord cross section is included in Figure 11(a), on the right. An axial-circumferential mesh plot of the rotor grid at the hub is shown in Figure 11(b), along with three circumferential-radial view mesh plots of the grid at the cross sections indicated.

A three-dimensional view of the stator grid is shown in Figure 12. Many of the comments in the previous paragraph also apply to the stator grid, except that the stator does not have an endwall clearance gap, and the upstream and downstream extension H-grid blocks are colored red.

An axial-circumferential mesh plot of the stator grid at midspan is shown in Figure 13, along with three circumferential-radial view mesh plots for the cross sections indicated.

Turbulent boundary layer flow solutions near solid walls always involve direct computation of the viscous sublayer; that is, wall functions are not used. It is important, therefore, that node spacings at solid walls be sufficiently small. The nominal wall-normal spacing at hub and tip endwalls is 0.00025 in., and at blade surfaces is 0.00010 in. Corresponding inner-variable wall distances, y^+ , are typically between 1.0 and 2.0 at the endwalls, and 0.2 and 0.8 at blade surfaces.

Table 1 summarizes the grid blocks and their sizes for the fan system computational domain, and Table 2 summarizes the grid blocks and their sizes for the system exit computational domain.

TABLE 1.—FAN SYSTEM COMPUTATIONAL GRID BLOCKS

Grid block	Size (I×J×K)	Number of nodes
Inlet duct inner H-grid	131×1×65	7,345
Inlet duct outer H-grid	97×1×97	9,409
Rotor inlet H-grid	13×38×85	41,990
Rotor blade C-grid	201×49×85	837,165
Rotor exit H-grid	73×89×77	500,269
Rotor tip clearance O-grid	157×15×17	40,035
Stator inlet H-grid	13×32×73	30,368
Stator blade C-grid	201×49×73	718,977
Stator exit H-grid	33×89×73	214,401
Diffuser duct H-grid	97×1×73	7,081
Total all grid blocks		2,407,040

TABLE 2.—SYSTEM EXIT COMPUTATIONAL GRID BLOCKS

Grid block	Size (I×J×K)	Number of nodes
Diffuser duct + exit outer H-grid	129×1×73	9,417
Exit inner/base H-grid	61×1×49	2,989
Exit extension tube H-grid	57×1×89	5,037
Total all grid blocks	-----	17,479

Aerodynamic Simulation Results

Fan system CFD results are presented below using averaged and non-averaged data. Circumferential (pitchwise) averaging of the three-dimensional flow fields was performed on a structured meridional grid for some selected solutions, allowing contour plots to be generated for the averaged flow fields. Detailed comparisons, however, are made at selected axial stations, the locations of which are shown in Figure 14 where they are indicated by red vertical dashed lines. The stations are labeled as indicated, and the corresponding axial coordinates are summarized below in Table 3. Note that the (near-) vertical blue lines in Figure 14 show mixing-plane locations, and the (near-) vertical gray lines show grid block interface locations. Stations 1a and 4b, respectively, are at the upstream and downstream boundaries of the computational domain(s), and are included only for completeness, as well as possible future reference.

TABLE 3.—AXIAL STATION LOCATIONS

Station label	X-coordinate (in.)
1a	-2.00
1b	-1.10
2a	0.05
2b	0.55
3a	2.60
3b	3.40
3c	4.20
3d	5.95
4a	10.50
4b	12.00

Overall averages, obtained by spanwise (radial) averaging of the circumferentially averaged flow field, were calculated at stations 2b, 3c, and 4a, to provide representative performance numbers for the rotor and fan stage. These results are summarized below in Tables 4 and 5, and are presented first because they provide a convenient overview of the operating points and performance values computed for the fan. Note that all simulated cases are included, off-design as well as design, and that the left column indicates the turbulence model used: (Low-Re) for the low-Reynolds-number model and (High-Re) for the high-Reynolds-number model. It should be recalled that, for the cases computed here, the low-Reynolds-number model is the one preferred. A fan performance map generated from these results, excluding the two off-design tip clearance cases, is shown in Figure 15, where total-pressure rise and hydraulic efficiency are graphed against volumetric flow rate.

TABLE 4.—COMPUTED ROTOR PERFORMANCE

Turbulence model	Rotor tip clearance, in.	Flow rate $Q/\sqrt{\theta}$, ft ³ /min	Pressure rise $\Delta p_{t,2b}$, in. water	Work input $\Delta h_{t,2b}$, in. water)	Hydraulic efficiency, $\eta_{H,2b}$	Rotor torque T/δ, in.-oz
Low-Re	0.009	141.34	4.391	4.947	0.8876	9.363
Low-Re	0.009	148.69	4.221	4.743	0.8900	9.445
Low-Re	0.009	156.12	4.020	4.521	0.8891	9.452
High-Re	0.009	148.67	4.232	4.750	0.8910	9.455
Low-Re	0.006	148.69	4.269	4.773	0.8944	9.504
Low-Re	0.012	148.69	4.191	4.730	0.8860	9.418

TABLE 5.—COMPUTED FAN STAGE PERFORMANCE

Turbulence model	Rotor tip clearance, in.	Flow rate $Q/\sqrt{\theta}$, ft ³ /min	Pressure rise $\Delta p_{t,3c}$, (in. water)	Hydraulic efficiency, $\eta_{H,3c}$	Pressure rise $\Delta p_{t,4a}$, in. water	Hydraulic efficiency, $\eta_{H,4a}$
Low-Re	0.009	141.34	3.957	0.7998	3.800	0.7843
Low-Re	0.009	148.69	3.800	0.8012	3.716	0.7834
Low-Re	0.009	156.12	3.613	0.7991	3.517	0.7780
High-Re	0.009	148.67	3.822	0.8048	3.739	0.7871
Low-Re	0.006	148.69	3.849	0.8064	3.764	0.7885
Low-Re	0.012	148.69	3.769	0.7969	3.685	0.7790

In Figure 15, as well as in Tables 4 and 5, the turbulence model version has only a small impact on the computed overall performance for the fan, at least for operation near the aerodynamic design point. At the design flow rate and tip clearance, the computed total-pressure rise is 3.716 in. of water for the fan system (station 4a, low-Reynolds-number model). This value meets, with some positive margin, the design objective of 3.640 in. of water, while the corresponding hydraulic efficiency of 0.7834 far exceeds expectations based on the Hamilton Sundstrand reference design. As reported in Reference 3, the computed design-flow total-pressure rise for the reference design fan system is 3.435 in. of water, with a hydraulic efficiency of 0.6663.

Referring again to Figure 15, notice the relative amount of total-pressure loss between stations 3c and 4a. That loss is comparatively small, with almost 70 percent of it due to the exit flow discharge. At station 3d, the design-flow total-pressure rise is 3.774 in. of water (low-Reynolds-number model; result not included in table or figure), giving a discharge total-pressure loss between stations 3d and 4a of 0.058 in. of water. If the annular diffuser is defined as beginning at station 3b, where the design-flow total-pressure rise is 3.825 in. of water (result not included in table or figure), then its total-pressure loss is 0.051 in. of water. The total combined loss for the annular diffuser and discharge is 0.109 in. of water. When normalized by the total-pressure rise for the entire fan system, the annular diffuser loss is 1.4 percent, the discharge loss is 1.6 percent, and the combined loss is 3.0 percent.

Several contour plots showing the fan system flow field and the exit discharge region flow field, for the design flow rate and rotor tip clearance, are contained in Figures 16 and 17, respectively, where for Figure 16 the three-dimensional blade-row flow solutions were mixed-out averaged in the circumferential direction.⁷ Note that the grid blocks in Figure 8 correspond to the contour plots of Figure 16, the grid blocks in Figure 9 correspond to the contour plots of Figure 17, and all of the contour plots were generated from the solution set obtained with the low-Reynolds-number $k-\omega$ turbulence model. The entropy rise and turbulence kinetic energy plots involve dimensionless values, with entropy rise nondimensionalized by the gas constant, R , for air, and turbulence kinetic energy normalized by the inlet kinetic energy. The inlet kinetic energy is based on the magnitude of the mean flow velocity at the flow straightener, $Q/A\sqrt{\theta}$, which has a value of 37.09 ft/sec at the design flow rate. Also note that Figure 17 uses the contour legends in Figure 16, as appropriate, with static-pressure rise using the same legend as total-pressure rise, and axial velocity using the same legend as velocity magnitude.

Most noteworthy in Figure 16 is the relatively thick, higher-entropy region generated at the rotor tip, convecting downstream and encompassing about 30 percent of the span next to the outer casing. Such an extensive endwall viscous-loss region is unusual, generally speaking, considering the amount of tip clearance (1.4 percent of span), and is a direct result of the relatively low Reynolds numbers involved. Simple considerations from flat-plate boundary layer theory suggest that this effect should be expected, although the highly viscous, three-dimensional nature of the tip clearance flow seems to amplify it considerably. When the Reynolds number for a flat-plate boundary layer flow is decreased by a factor of 10, for example, the thickness of the layer increases by a factor of $\sqrt{10}$ (equal to 3.2) if it is laminar, or by a factor of about $\sqrt[5]{10}$ (equal to 1.6) if it is turbulent. Lower Reynolds numbers are also generally associated with delayed, or even nonexistent, laminar-to-turbulent transition, as well as with decreased turbulence viscosity levels. In view of all this, and recognizing that laminar boundary layers have proportionately greater displacement thicknesses than turbulent ones, it becomes apparent why such a large annulus-area blockage (18.5 percent, as discussed earlier) was needed at the rotor exit trailing edge station for the NCDP design code input.

Also of interest in Figure 16 are the inlet- and exit-diffuser flow fields. The inlet integrates well with the rotor, aerodynamically as well as geometrically, so that there is no overexpansion of the local flow around the hub/spinner nose. This avoids any significant adverse pressure gradients for the hub boundary layer before it enters the rotor blade row. The flow in the exit diffuser is also clean, with fully attached boundary layers throughout. Although the diffuser hub boundary layer is approaching a condition of separation, there is no reverse flow until after the flow discharges into the downstream tube, as the axial velocity contour plot in Figure 17 reveals. The thick black contour in the plot corresponds to a value of zero and outlines a region of reverse flow (negative axial velocity) just downstream of the diffuser centerbody. This reverse-flow region extends downstream to an axial location of about 10.0 in., and so has an axial length of 4.0 in.

Axial distributions of static-pressure rise at the hub and tip endwalls for the fan system and the exit discharge region are shown in Figures 18 and 19, respectively. These results correspond to the design flow rate and rotor tip clearance, and involve circumferentially mixed-out averaged flow field solutions. Both the low- and high-Reynolds-number turbulence model results are included for comparison, but the differences between them are small. Blade row locations are indicated by thin vertical lines with labels, so various sections of the flow path can be identified along with corresponding static-pressure rise changes and gradients. As expected, static pressure generally increases in the axial/streamwise direction, except in the inlet and near the outer casing between the rotor and stator, and the static-pressure rise and related pressure gradient are largest at the tip of the rotor. Static-pressure recovery for the diffuser is good, with static pressure increasing by 0.869 in. of water from station 3b to station 4a. The corresponding total-pressure loss, as discussed above, is only 0.109 in. of water.

Line graphs of circumferentially mixed-out averaged results at all axial stations from 1b through 3d, for the design flow rate and rotor tip clearance, are presented in Figures 20 through 26, respectively. A fairly

⁷Turbulence kinetic energy was mass-averaged in the circumferential direction.

extensive set of graphs is included for documentation purposes, so many of the graphs are not discussed. Again, results for the low- and high-Reynolds-number turbulence models are included for comparison, and the differences between them are generally small. The largest differences are seen near the tip endwall, where three-dimensional viscous effects are important. Note that the contour plots of Figure 16 may be helpful for interpreting these line graphs, by providing a broader perspective for the station data.

Referring to Figures 21(a) and 22(a), corresponding to stations 2a and 2b, the total-pressure rise and work input distributions downstream of the rotor are nearly flat for most of the passage, that is, from about 5 to 70 percent of passage height, in which region the hydraulic efficiency is very high at around 0.977. The flat total-pressure profile is intended for the design, and would ideally extend all the way from hub to tip if three-dimensional viscous effects did not make it impractical. Near the endwalls, especially the tip, the efficiency decreases as a result of higher total-pressure losses there, appearing as higher entropy in the contours of Figure 16. These losses will be discussed more below. Note that it is common practice with pumps and low-speed fans to calculate hydraulic efficiency using work input based on changes in tangential velocity multiplied by blade speed (a kinematic quantity). At low Reynolds numbers, however, this approach leads to excessive errors because viscous effects are too prevalent. To avoid such errors here, the work input has been calculated using total-enthalpy rise (a thermodynamic quantity). Similarly, it would be more accurate to use thermodynamic adiabatic efficiency rather than hydraulic efficiency, but convention favors the latter. In general, calculated hydraulic efficiencies are greater than corresponding adiabatic efficiencies, with the differences depending on the particular conditions involved, and decreasing to zero as flow compressibility approaches zero. For all cases presented herein, representative hydraulic efficiency values are greater than adiabatic efficiency values by an amount somewhere between 0.0024 and 0.0036.

As the rotor exit flow convects downstream, first through the stator blade row, and then through the annular diffuser, the flow property profiles become progressively more rounded; that is, less flat (compare results at stations 2a through 3d in Figures 21(a) through 26(b)). Viscous dissipation and blade-row generated secondary flows are the fluid dynamic mechanisms producing this effect, both working to expand the influence of the endwalls by mixing the endwall fluid with the high-efficiency core flow. Almost all the rotor exit flow swirl (negative tangential velocity) is removed by the stator, which leaves less than 5° of residual swirl at its exit. Near the hub endwall, secondary flow effects in the stator blade row lead to a significant amount of overturning, that is, to positive tangential velocities at the stator exit (see stations 3a through 3d in Figures 23(a) through 26(b)), but the level of over-turning is not excessive.

Line graphs showing several blade row parameters relevant to the aerodynamic design and performance of the fan are presented in Figures 27 and 28. Parameters for the rotor blade row are shown in Figure 27, and parameters for the stator blade row are shown in Figure 28. The results graphed are based on circumferentially mixed-out average quantities at blade leading and trailing edge meridional stations, and results for the low- and high-Reynolds-number turbulence models are both included for comparison. For the rotor (see Fig. 27(a)), the graph of total-pressure loss coefficient shows very low losses over most of the span, corresponding to the high hydraulic efficiencies discussed earlier for the same approximate region of the passage. Near the hub and tip endwalls, however, the loss coefficients are more than an order of magnitude higher due to the additional losses generated by the endwall flows. The high-loss region at the tip involves a substantial fraction of the passage flow, and therefore has a significant effect on overall performance. The graph of diffusion factor shows an increasing trend from hub to tip, but values remain under 0.4 everywhere outside the endwall flow regions, indicating low to moderate levels of aerodynamic blade loading, at least by conventional standards. Diffusion factors are especially low near the hub because of the 30° hub ramp angle and corresponding radius increase. Near the tip, diffusion factor follows roughly the same trend as loss coefficient. Given that the near-tip diffusion factors are less than 0.4 when the high-loss region is neglected, the amount of tip-generated loss (entropy) seems inordinately large, and demonstrates the increased influence of viscosity at low Reynolds numbers.

For the stator (see Fig. 28(a)), the graphs of loss coefficient and diffusion factor reveal moderate levels for each. It should be noted that the stator losses exhibited little sensitivity to variations in blade geometry during the aerodynamic design process, so as a result the design effort focused more on aerodynamic predictability and robustness. Notice in the figure that the loss coefficients near the endwalls are negative

(truncated by the graph), but that the maximum values are close by, at approximately 10 percent of span away from each wall. This is a result of secondary flow migration in the blade row, where low-momentum fluid is transported away from the endwalls. Regarding the diffusion factors, an important design objective involved maintaining a nominal value of 0.4, which was accomplished by increasing the blade chord length in order to increase the aerodynamic solidity. Although the resulting diffusion factors are considered moderate by conventional standards, it is noteworthy that the flow deviation angles are so large (see Fig. 28(a)), around 15° over most of the span. Efforts were made during the design process to reduce them, but improvements proved elusive. Apparently, the large deviation angles are also a low-Reynolds-number effect.

Further consideration of the fluid dynamics associated with rotor-tip loss generation leads to the conclusion that the primary loss source is the shear flow on the endwall surface. This shear flow involves the fairly steep axial/streamwise static-pressure gradient that accompanies the relatively large static-pressure rise at the rotor tip (see Fig. 18). The flow through the tip clearance gap also contributes to the loss, but its main effect is to produce a fairly strong vortex that eventually redistributes the high-entropy endwall fluid in the spanwise direction. In this respect the clearance flow can be beneficial, in that it disperses the high-loss, low-momentum endwall fluid so that it does not accumulate and lead to large-scale flow separation. However, rotor tip clearances are generally viewed in a negative light because larger clearance gaps are virtually always associated with higher losses. Smaller clearance gaps, on the other hand, although better aerodynamically, are more costly to achieve and maintain. It is therefore of some interest to quantify the influence of the tip clearance gap height on fan efficiency, particularly at these low Reynolds numbers where the tradeoff between performance and cost may be different than expected.

Comparing the bottom two rows in Tables 4 and 5 with the second row of numbers reveals the effect of decreased and increased rotor tip clearance on overall performance. Decreasing the clearance by 0.003 in., or 33 percent, increases the design-flow pressure-rise slightly, and improves the fan system hydraulic efficiency by 0.0051. Conversely, increasing the clearance by 0.003 in. decreases the design-flow pressure-rise slightly, and degrades the system hydraulic efficiency by 0.0044. These changes in performance are quantitatively significant, but are smaller than anticipated given the large role that tip-generated losses have on the overall fan efficiency.

The rotor blade-to-blade flow field in the rotating frame-of-reference is shown in Figure 29 for three stream surfaces of revolution: one at 85 percent of passage flow (near the tip), one at 50 percent of passage flow (near midspan), and one at 15 percent of passage flow (near the hub). Contours of relative velocity magnitude are plotted using the same contour range for all three stream surfaces, and flow solutions for both the low- and high-Reynolds-number turbulence models are presented for comparison. In Figure 30, contours of turbulence kinetic energy (normalized by system inlet kinetic energy) are shown for the 50 percent of passage flow stream surface, with small red arrows indicating locations where laminar-to-turbulent boundary layer transition occurs. Transition behavior and turbulence development on the blade surface for the near-hub and near-tip stream surfaces are similar to that at midspan, so turbulence kinetic energy contours are not shown for those locations. Line graphs showing chordwise distributions of rotor blade surface pressure coefficient, C_p , for the 15, 50, and 85 percent of passage flow stream surfaces are provided in Figure 31. The pressure coefficient accounts for the effects of rotation and radius change, and the reference values for static and relative total pressure are based on the mixed-out average conditions at the blade leading edge. In these line graphs, the top curve corresponds to the blade pressure surface, the bottom curve corresponds to the blade suction surface, and the vertical spacing between the curves is related to the local aerodynamic loading (static pressure difference) at a particular chordwise location. In the contour plots, the upper blade surface corresponds to the suction surface.

In general, the blade-to-blade flow field for all three stream surfaces is aerodynamically clean and robust. The pressure coefficient distributions are all similar, and show that the rotor blade loading is maximum at the front of the blade, especially near the leading edge, and decreases almost linearly from about 25 percent of chord to the trailing edge. On the blade suction surface the static-pressure gradient, or rate of flow deceleration/diffusion, is fairly uniform, and the boundary layer remains attached. With the low-Reynolds-number turbulence model the blade boundary layers are virtually all laminar, and transition

to turbulence takes place at the trailing edge. Notice that on the suction side the transition actually occurs slightly upstream of the trailing edge (see small red arrow in Fig. 30). This is accompanied by a small region of reverse flow, but the region is too small to be significant and can be considered as part of the wake. With the high-Reynolds-number model, transition to turbulence occurs at the front of the blade, on both sides, and the resulting turbulent boundary layers are noticeably thicker, as is also the wake. Aside from that, however, the flow fields are very similar. It might be added that it is unusual to have an all-laminar blade flow, such as that simulated using the low-Reynolds-number model, but the solution is probably correct, or is at least more accurate than the solution obtained using the high-Reynolds-number model.

Relative velocity magnitude and turbulence kinetic energy contour plots in Figure 32 show the computed flow field in and around the rotor tip clearance gap. The blade-to-blade contours in Figures 32(a) and 32(b) were calculated on a surface-of-revolution located spanwise near the middle of the clearance gap, and the contours in Figure 32(c) were calculated on a plane perpendicular to the axis of rotation at a midchord axial location (axial coordinate -0.700 in.; see Figs. 1 and 2). A comparison of the flow field solutions obtained with the low- and high-Reynolds-number turbulence models reveals significant differences, but the impact on overall performance is small, and both solution sets indicate acceptable aerodynamic characteristics. Notable is the lack of turbulence for most of the tip flow region as computed using the low-Reynolds-number model. Of particular interest is the laminar-free shear-layer between the tip jet and the flow just below the jet, on the suction side of the blade (see Fig. 32(c), left side of figure, right side of blade). The region below the shear layer is also laminar and involves a radial-tangential secondary flow which is considerably larger than that computed using the high-Reynolds-number turbulence model (compare to right side of Fig. 32(c)). Although no flow/numerical stability problems were encountered in connection with the laminar-free shear-layer computed for this design, CFD simulations for the reference fan design did exhibit unusual flow features indicative of an instability (Ref. 3).

The rotor exit flow field at station 2b, located over one chord-length downstream of the rotor blade row, is shown in Figure 33, where contour plots of relative velocity magnitude, total-pressure rise, entropy rise, and turbulence kinetic energy are presented. Solution results for both the low- and high-Reynolds-number turbulence models are included, and are generally similar to each other. Close inspection reveals some differences in local flow features, but their significance is thought to be minimal. Note that the contour levels of relative velocity magnitude are the same as those in Figures 29 and 32, that total-pressure rise is in the stationary system, entropy rise is nondimensionalized by the gas constant, and turbulence kinetic energy is normalized by inlet kinetic energy (see discussion of Fig. 16). Rotation is in the direction indicated, so the wake-convecting flow field is moving counterclockwise, and the circumferential property variations are, in the stationary frame of reference, transient fluctuations. Tone noise is generated as this periodic unsteady flow interacts with the stator blades at the blade-passing frequency of the rotor. Although the stator blade row is actually located further downstream, it is close enough that the fluctuation patterns and amplitudes there should be similar to those existing at station 2b. No effort has been made as yet to predict the tone noise, and the acoustic complexities involved require specialized methods to do so. At the risk of over-simplification, however, it might be suggested that the total-pressure contours give at least some impression of the noise-generating wake intensity. It might be added that turbulence kinetic energy is also related to noise, but to noise of a different type; namely, broadband noise.

The stator blade-to-blade flow field in the stationary frame of reference is shown in Figure 34 for the same three stream surfaces of revolution used for the rotor: 85, 50, and 15 percent of passage flow. Velocity magnitude and turbulence kinetic energy contours are plotted, each using the same contour range for all three stream surfaces, and flow solutions for both the low- and high-Reynolds-number turbulence models are presented for comparison. Small red arrows in the turbulence kinetic energy plots indicate locations of laminar to turbulent transition on the blade surface, except at 85 percent of passage flow where the blade boundary layer is turbulent all the way from the leading edge. Line graphs showing chordwise distributions of stator blade surface pressure coefficient, C_p , for all three stream surfaces are provided in Figure 35. The reference values of static- and total-pressure for the pressure coefficient are based on the mixed-out average conditions at the blade leading edge. The top curve in each line graph corresponds to the blade pressure surface, the bottom curve corresponds to the blade suction surface, and the vertical spacing between the

curves is related to the local aerodynamic loading (static pressure difference) at a particular chordwise location. In the contour plots, the lower blade surface corresponds to the suction surface.

From the contour plots it can be seen that the stator blade-to-blade flow field is basically the same for all three stream surfaces, and that the turbulence model has a noticeable, but small, effect on it. This similarity is also seen in the pressure coefficient distributions, which show that the stator blade loading is maximum at the front of the blade, especially near the leading edge, and decreases almost linearly from about 5 percent chord to around midchord, after which it remains fairly constant. The flow diffusion (deceleration and static-pressure rise) on the blade suction surface is strongly biased toward the front half of the blade, while the back half involves a separated boundary layer that largely reduces its capacity for any significant and sustained diffusion.

Low diffusion over the back half of the suction surface is an intended feature of the blade profile design, which was developed to limit the overall increase in static pressure on the suction surface. During the design process it became apparent that, for the targeted diffusion factor level of 0.4, the suction surface boundary layer has a stubborn tendency to separate upstream of the trailing edge. Instead of trying to completely avoid the separation, therefore, the design was developed to accommodate and minimize it, while achieving the desired amount of flow turning; that is, while achieving zero swirl at stator exit. A related issue involved the existence of a laminar separation bubble, a small laminar boundary layer separation followed by turbulent reattachment, on the suction surface upstream of midchord. Although the separation bubble only exists in solutions computed using the low-Reynolds-number turbulence model, that model was and is preferred over the high-Reynolds-number model. For the final design, the presence of the bubble can be seen in Figure 35 by a local depression in the lower pressure-coefficient curve for the distributions at 50 and 15 percent of passage flow. The pressure dip extends from about 20 to 35 percent of chord, and does not exist at the 85 percent of passage flow location because the boundary layer there is everywhere turbulent, even with the low-Reynolds-number turbulence model.

An effort was made to eliminate the separation bubble, either by delaying transition until the aft separation, or by achieving transition without a separation bubble, but neither approach was successful. All such designs only increased the severity of the aft separation and led to under-turning of the flow. It was decided, therefore, to deliberately include the separation bubble in the blade profile development, a design approach that favors stability and predictability over separation avoidance. The final design locates the separation bubble at around 25 percent of chord, and produces a stable, attached turbulent boundary layer segment between the bubble and the aft separation. Higher levels of turbulence, as indicated by results for the high-Reynolds-number turbulence model, only improve the aerodynamic stability by eliminating the separation bubble and reducing the size of the aft separation. Notice in Figure 34 that the size of the aft separation zone varies along the span, and as just mentioned, depends on the turbulence model. The stator at 50 percent of passage flow is representative, however, and there the boundary layer separates near 75 percent of chord with the low-Reynolds-number turbulence model, and near 85 percent of chord with the high-Reynolds-number model.

Finally, contour plots showing the stator exit flow field at station 3b, located over one chord-length downstream of the stator blade row, are provided in Figure 36. Plots of velocity magnitude, total-pressure rise, entropy rise, and turbulence kinetic energy are presented for both the low- and high-Reynolds-number turbulence models. Note that the contour levels of velocity magnitude are the same as those in Figure 34, that entropy rise is nondimensionalized by the gas constant, and turbulence kinetic energy is normalized by inlet kinetic energy (see discussion of Fig. 16). All in all, these plots are included primarily for completeness and documentation purposes, as they show nothing unexpected or unconventional when the first-order, low-Reynolds-number effects are taken into account. The stator exit flow field is aerodynamically sound, and the differences between the two turbulence model solutions are relatively minor.

Summary and Concluding Remarks

A spacecraft cabin ventilation fan has been aerodynamically designed using tools and methodologies similar to those employed by the aircraft engine industry. Computational fluid dynamics methods were used to develop and assess the design, which is expected to exceed the design goals for aerodynamic performance. Necessary specifications and constraints for the design were obtained from a preexisting reference design, compared to which the new fan has a lower rotational speed, reduced by 25 percent, and a greatly improved hydraulic efficiency. The new design is intended to serve as a baseline for future research and development, including possible use as a test bed for investigating noise-reduction concepts.

Decreased fan noise relative to the reference design is an important objective for the new design. Acoustic analysis and prediction methods have not yet been applied, but the lower rotational speed and cleaner aerodynamics are expected to translate into less noise.

As a next step, it is recommended that the new fan, along with the reference fan, be built and tested. This is necessary to effectively advance the program, first by verifying the predicted aerodynamic performance of each fan, and second, by quantifying and comparing the noise generated by each. System integration may also be an important topic for future study, since distortion of the inlet and exit flow fields can significantly affect aerodynamic and acoustic performance.

References

1. Munch, C.L.: Noise Reduction Study of Orbiting Workshop Ventilation Fans. NASA CR-102287 (Wyle Laboratories TM 69-4), 1969.
2. Misoda, J.; and Magliozzi, B.: Fan and Pump Noise Control. NASA CR-128986 (Hamilton Standard SVHSER-6183), 1973.
3. Tweedt, Daniel L.: Computational Aerodynamic Simulations of an Orion Spacecraft Cabin Ventilation Fan Design. NASA/ASRC-2009-AS6461-HSF (unpublished contractor report), 2009.
4. Crouse, James E.; and Gorrell, William T.: Computer Program for Aerodynamic and Blading Design of Multistage Axial-Flow Compressors. NASA TP-1946 (AVRADCOM Technical Report 80-C-21), 1981.
5. Lovell, John S.; and Magliozzi, Bernard: Design Guidelines for Quiet Fans and Pumps for Space Vehicles. NASA/CR-2008-215427 (also Hamilton Standard SVHSER 6225), 2008.
6. Munson, Bruce Roy; Young, Donald F.; and Okiishi, T.H.: Fundamentals of Fluid Mechanics. Second ed., John Wiley & Sons, New York, NY, 1994, pp. 811-815.
7. Koch, L. Danielle: An Experimental Study of Fan Inflow Distortion Tone Noise. NASA/TM-2010-215844 (AIAA-2009-3290), 2009.
8. Sofrin, T.G.; and Mathews, D.C.: Asymmetric Stator Interaction Noise. *J. Aircraft*, vol. 17, no. 8, 1979, pp. 554-560.
9. Tyler, J.M.; and Sofrin, T.G.: Axial Flow Compressor Noise Studies. SAE International Technical Papers, paper no. 620532, 1962.
10. Chima, Rodrick V.: Viscous Three-Dimensional Calculations of Transonic Fan Performance. NASA TM-103800, 1992.
11. Chima, Rodrick V.; and Yokota, Jeffrey W.: Numerical Analysis of Three-Dimensional Viscous Internal Flows. *AIAA J.*, vol. 28, no. 5, 1990, pp. 798-806.
12. Tweedt, Daniel L.; and Chima, Rodrick V.: Rapid Numerical Simulation of Viscous Axisymmetric Flow Fields. NASA TM-107103 (AIAA-96-0449), 1995.
13. Tweedt, Daniel L.; Chima, Rodrick V.; and Turkel, Eli: Preconditioning for Numerical Simulation of Low Mach Number Three-Dimensional Viscous Turbomachinery Flows. NASA TM-113120 (ICOMP-97-11), 1997.
14. Tatsumi, S.; Martinelli, L.; and Jameson, A.: Flux-Limited Schemes for the Compressible Navier-Stokes Equations. *AIAA J.* (AIAA-94-0647), vol. 33, no. 2, 1995.

15. Tatsumi, S.; Martinelli, L.; and Jameson, A.: A New High Resolution Scheme for Compressible Viscous Flows with Shocks. AIAA 95-0466, 1995.
16. Chima, Rodrick; and Liou, Meng-Sing: Comparison of the AUSM+ and H-CUSP Schemes for Turbomachinery Applications. AIAA 2003-4120 (NASA/TM-2003-212457), 2003.
17. Chima, Rodrick V.: Swift—Multiblock Analysis Code for Turbomachinery. User's Manual and Documentation, Version 300, 2003.
18. Menter, F.R.: Two-Equation Eddy-Viscosity Turbulence Models for Engineering Applications. AIAA J. (NASA TM-111958 and AIAA 93-2906), vol. 32, no. 8, 1994, pp. 1598-1605.
19. Giles, Michael B.: Nonreflecting Boundary Conditions for Euler Equation Calculations. AIAA J., vol. 28, no. 12, 1990, pp. 2050-2058.
20. Giles, M.: UNSFLO: A Numerical Method for the Calculation of Unsteady Flow in Turbomachinery. GTL report 205, 1991.
21. Wilcox, David C.: Turbulence Modeling for CFD. Third ed., DCW Industries, La Cañada, CA, 2006.
22. Chima, Rodrick V.: TCGRID 3-D Grid Generator for Turbomachinery. User's Manual and Documentation, Version 300, 2003.

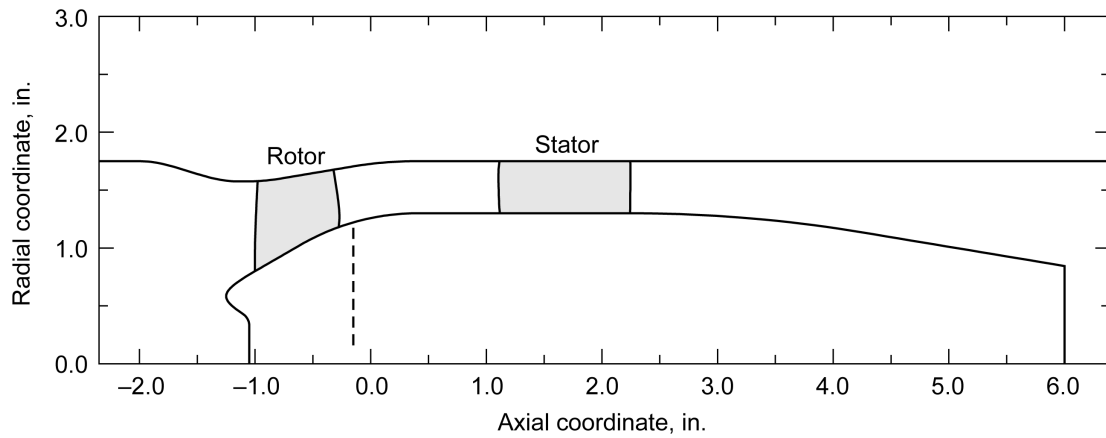


Figure 1.—Fan system meridional flow path.

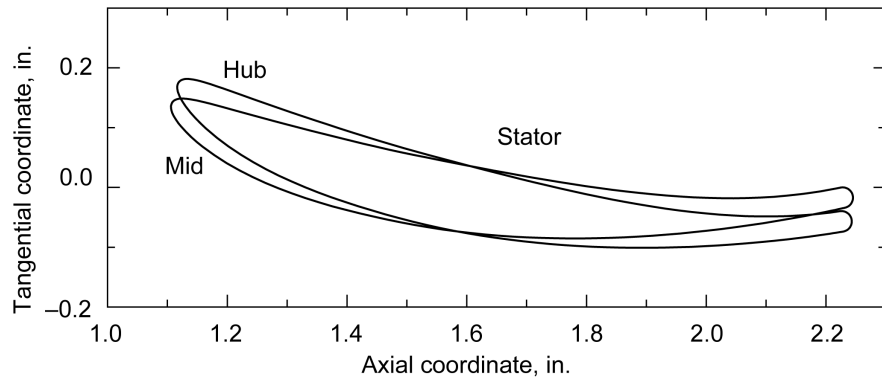
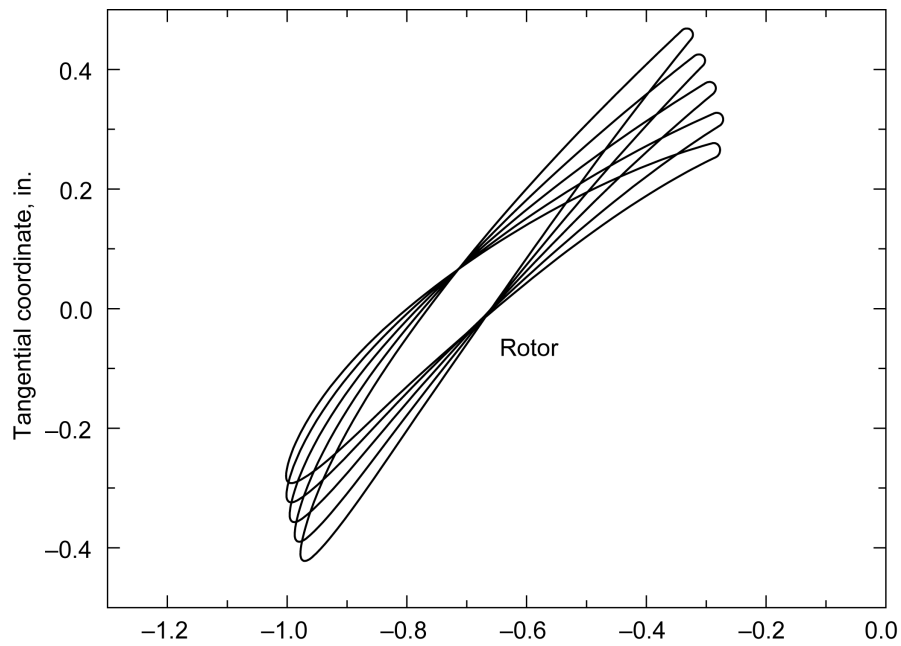


Figure 2.—Rotor and stator blade sections.

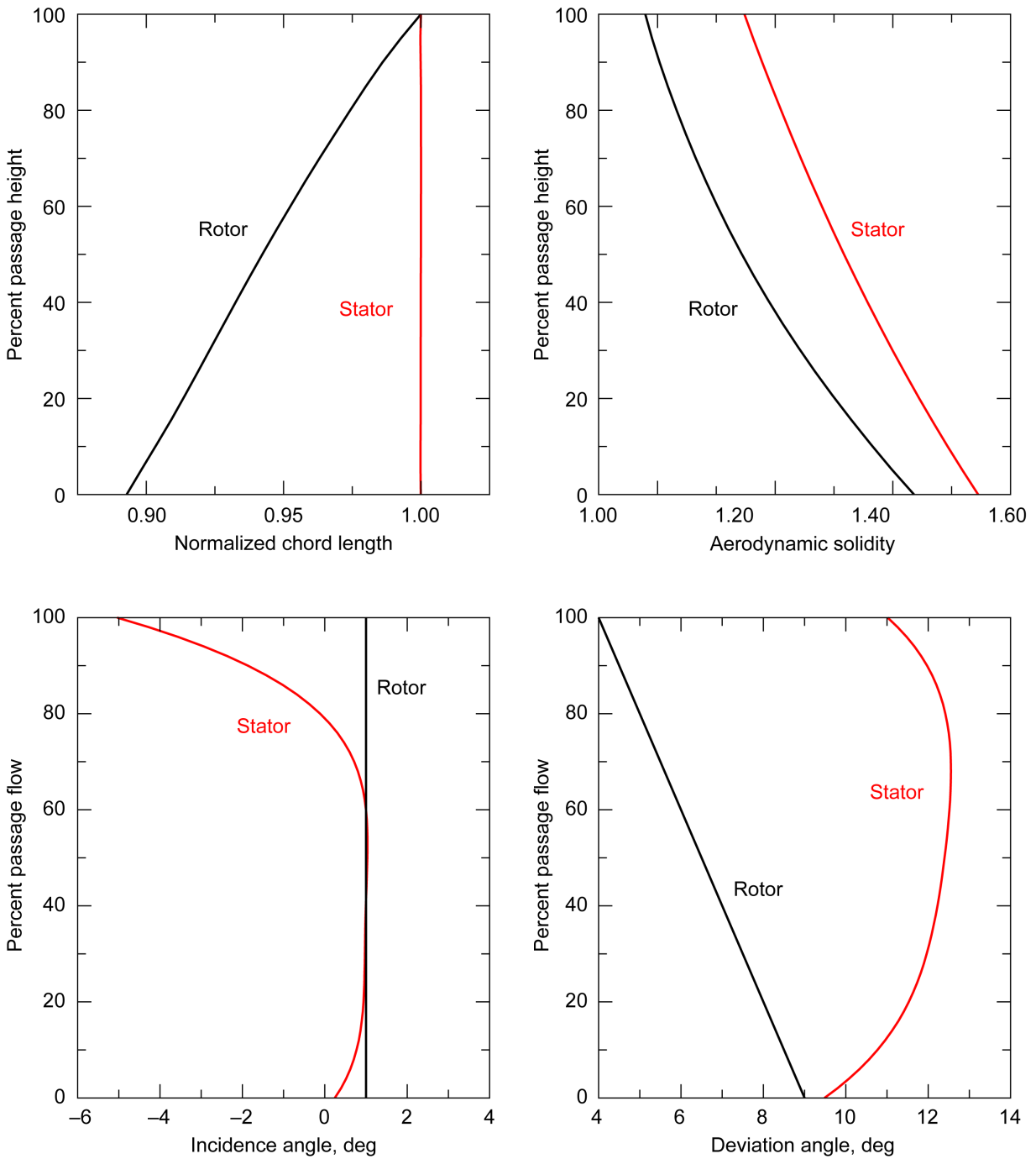


Figure 3.—Rotor and stator blade design parameters.

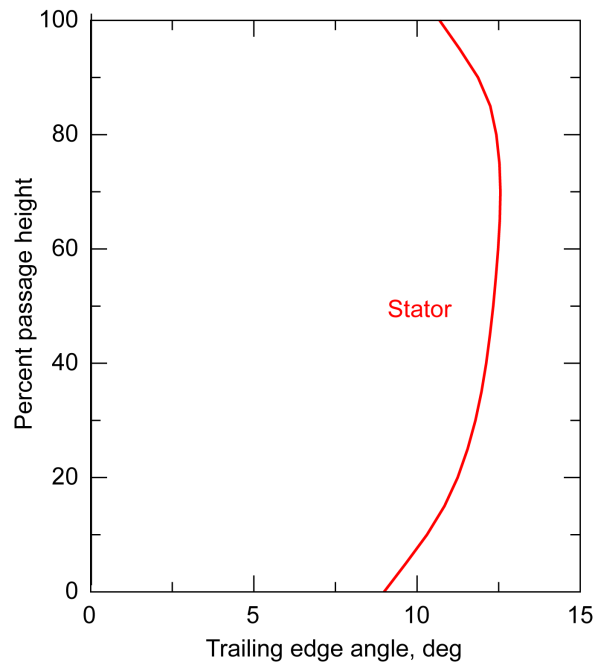
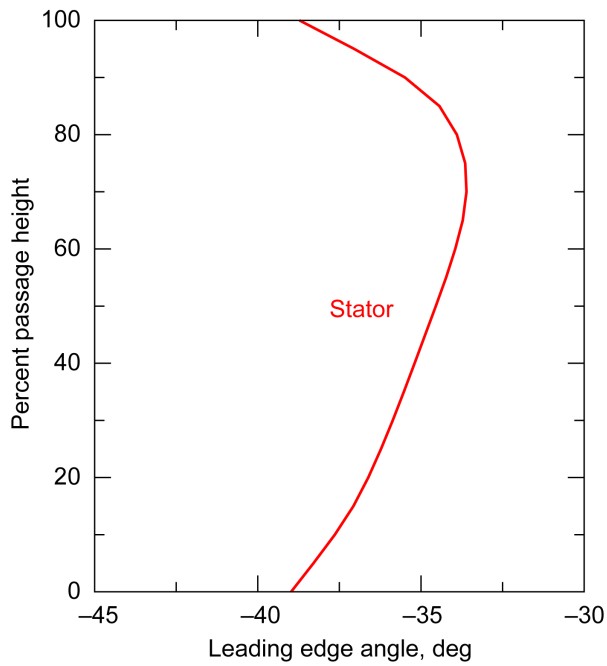
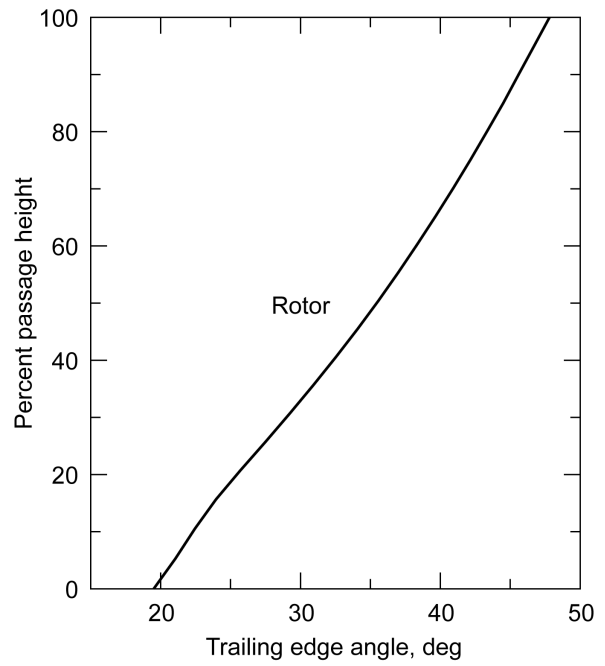
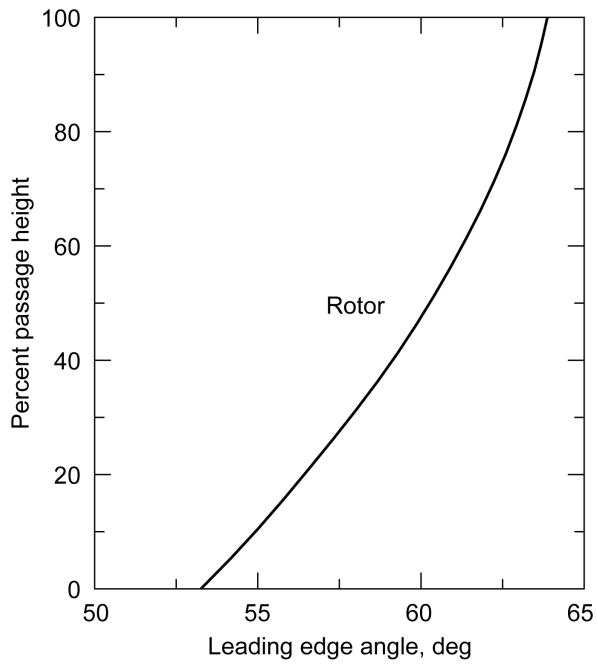


Figure 4.—Rotor and stator blade leading and trailing edge angles.

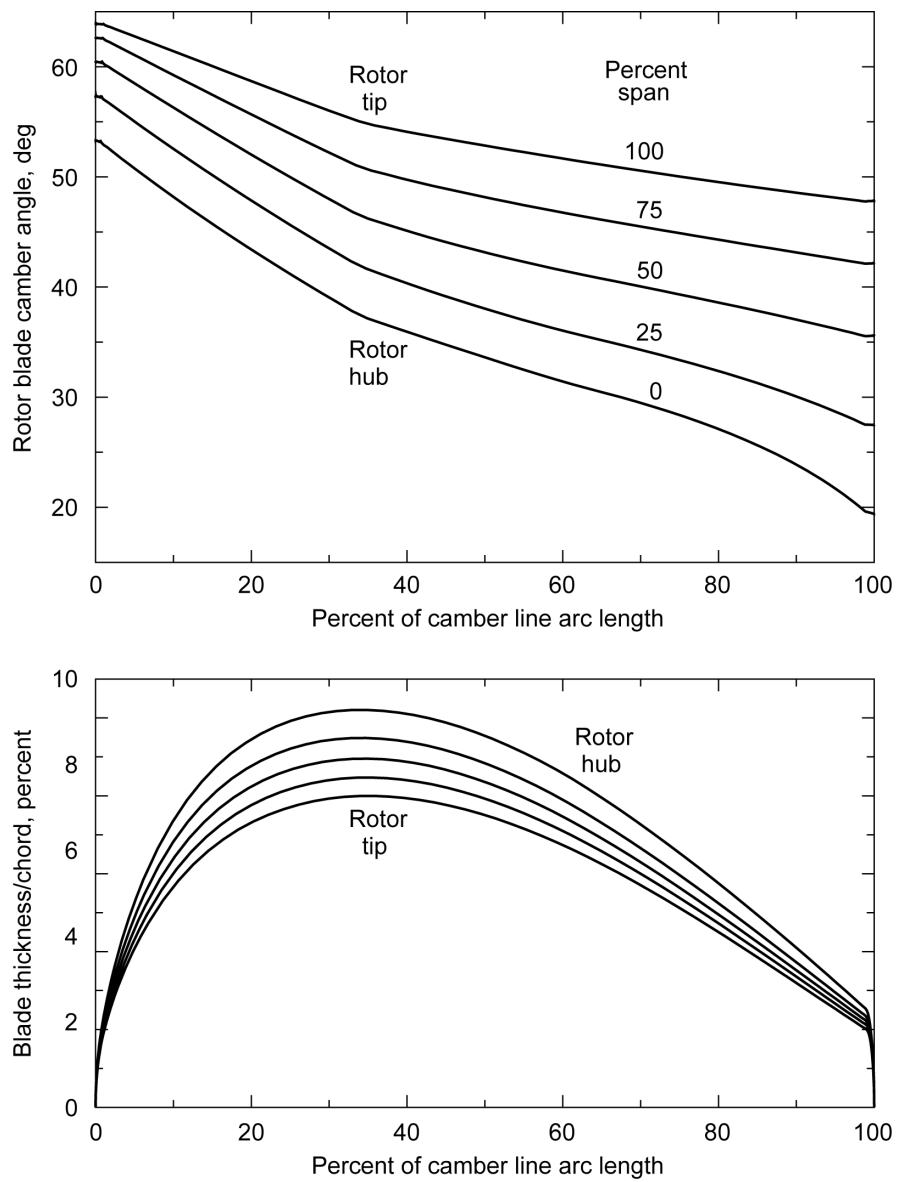


Figure 5.—Rotor blade camber-angle and thickness distributions.

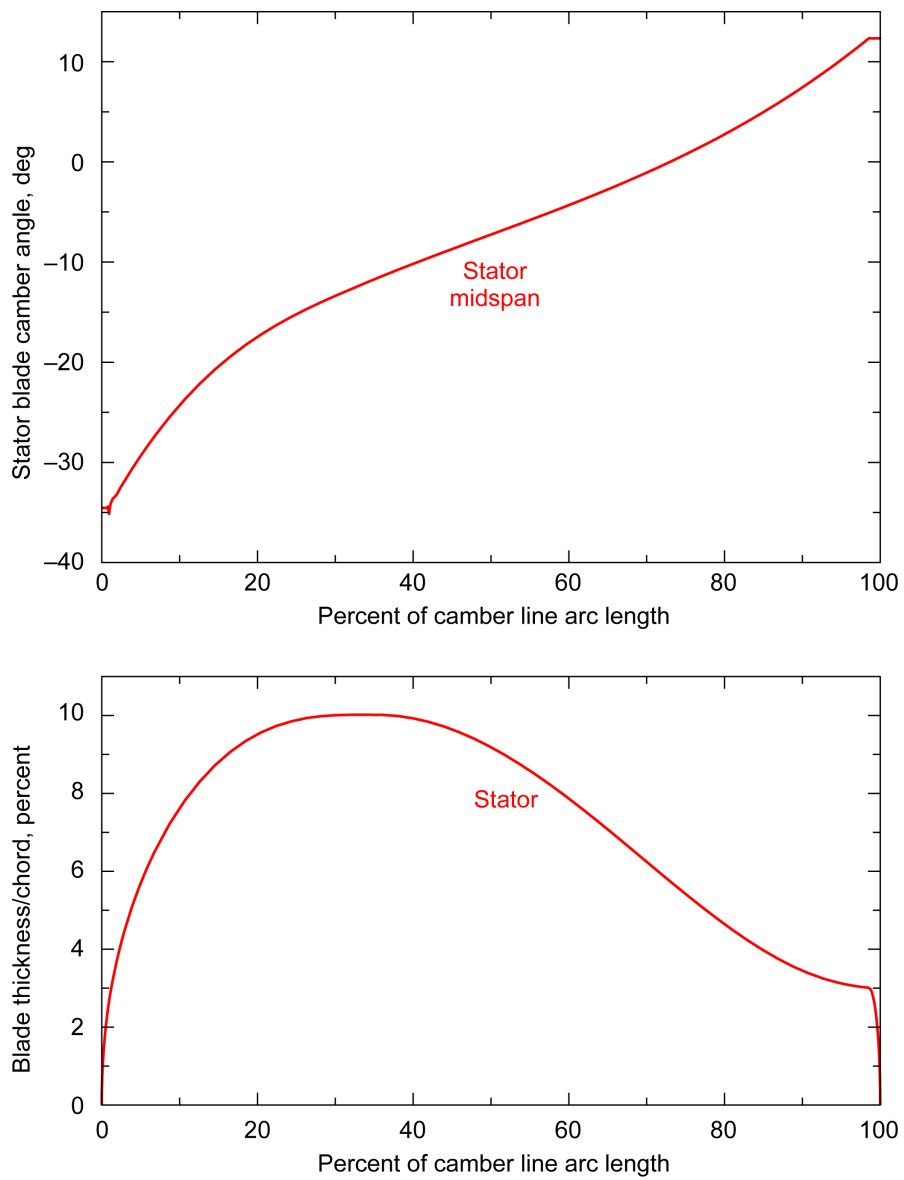


Figure 6.—Stator blade camber-angle and thickness distributions.

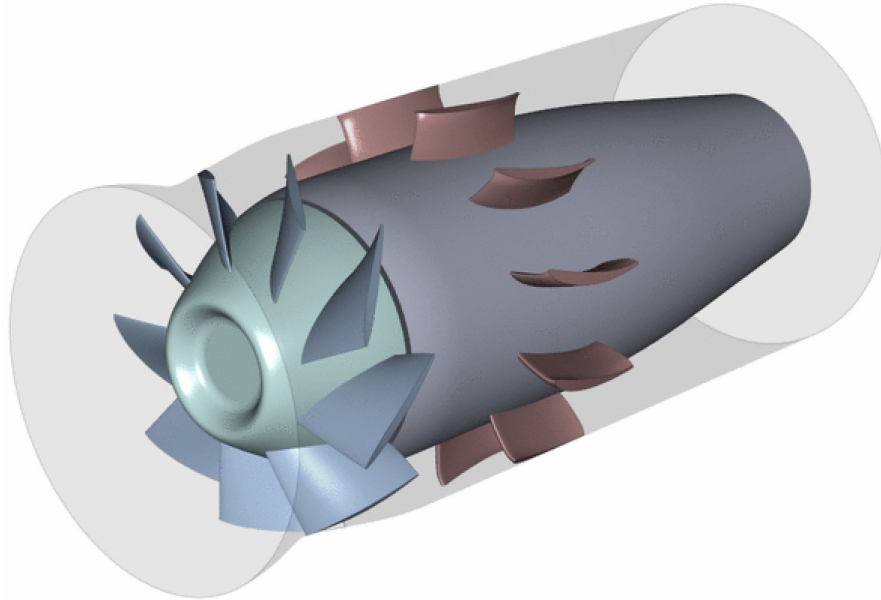


Figure 7.—Three-dimensional view of fan system.

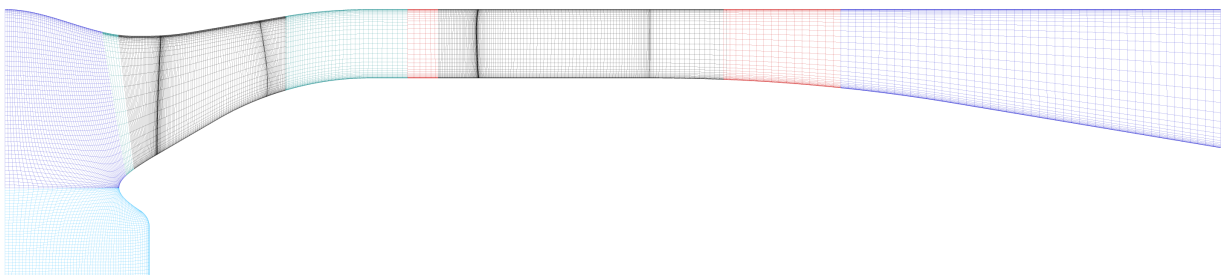


Figure 8.—Meridional view of fan system grid blocks.

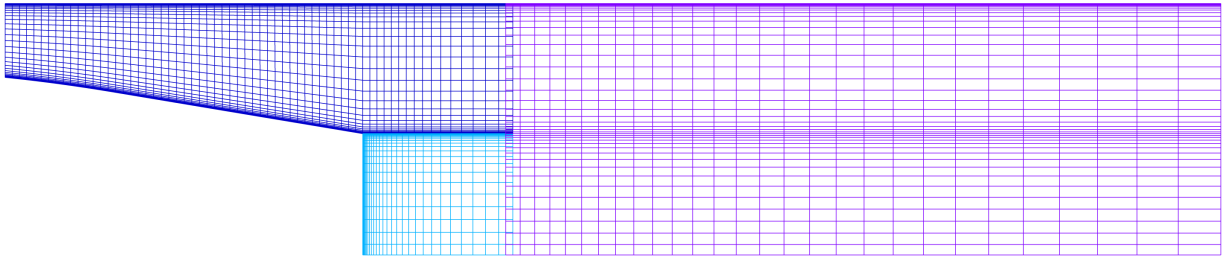


Figure 9.—System exit grid blocks.

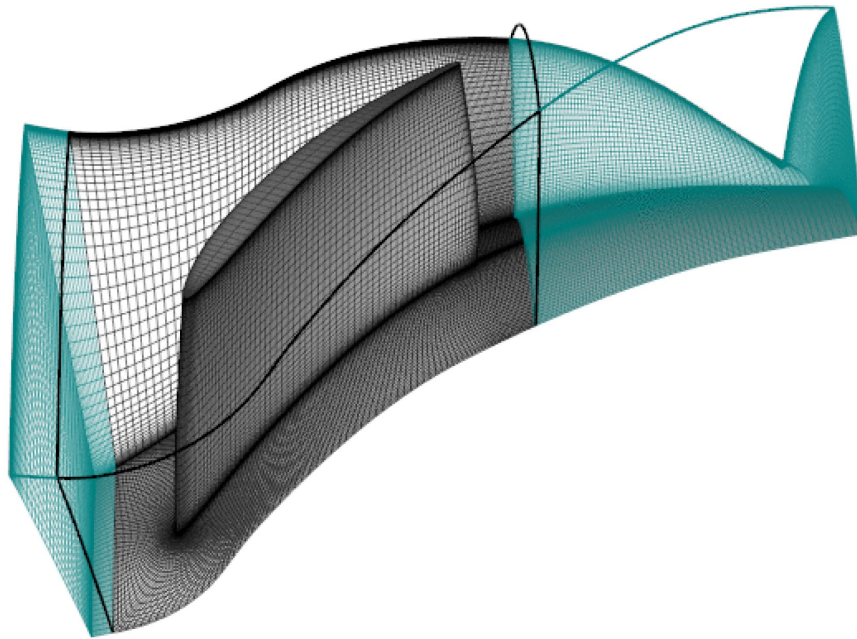


Figure 10.—Three-dimensional view of rotor grid blocks.

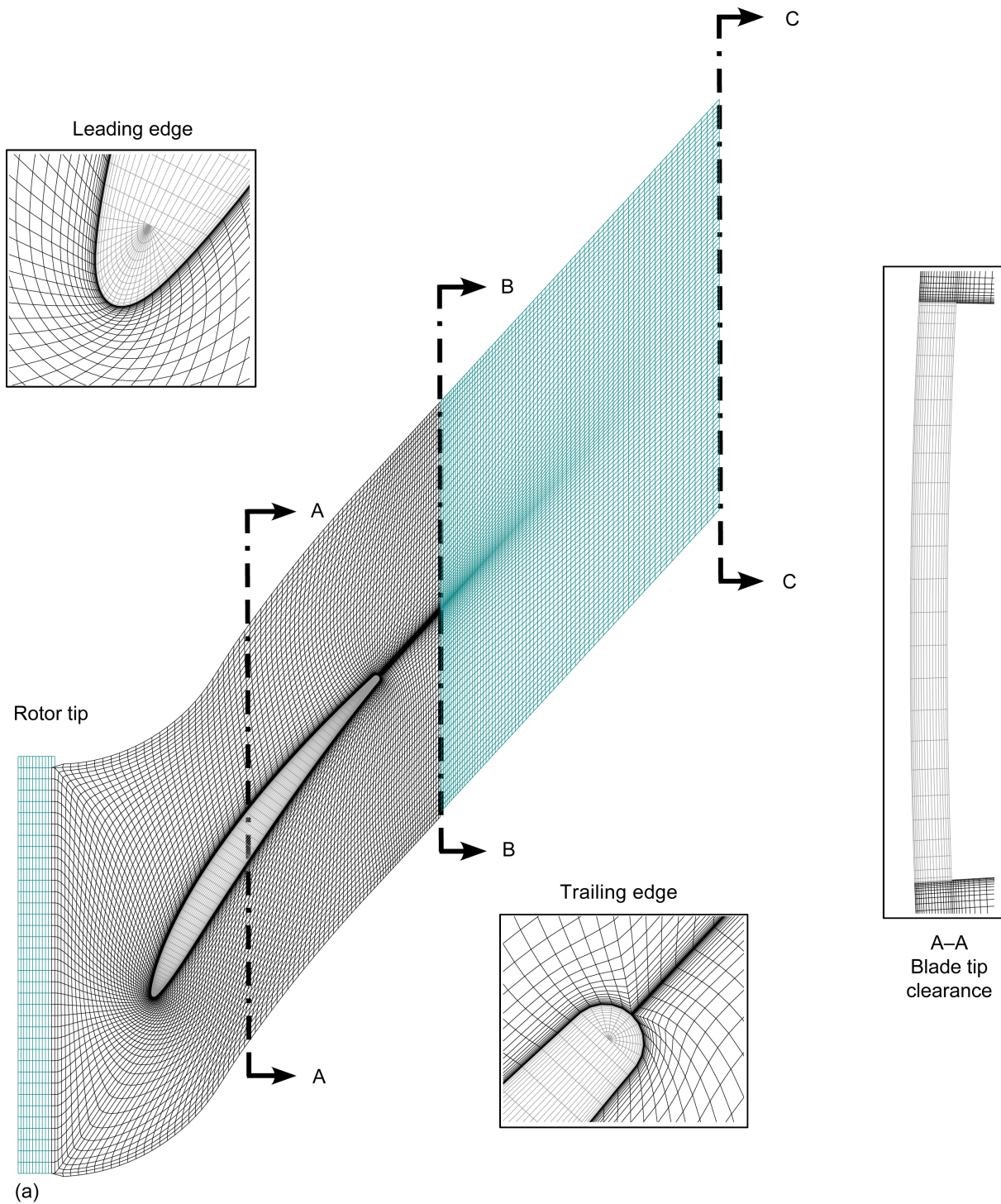


Figure 11.—Rotor grid mesh plots. (a) An axial-circumferential (blade-to-blade) mesh plot of the rotor grid at the blade tip. (b) An axial-circumferential mesh plot of the rotor grid at the hub.

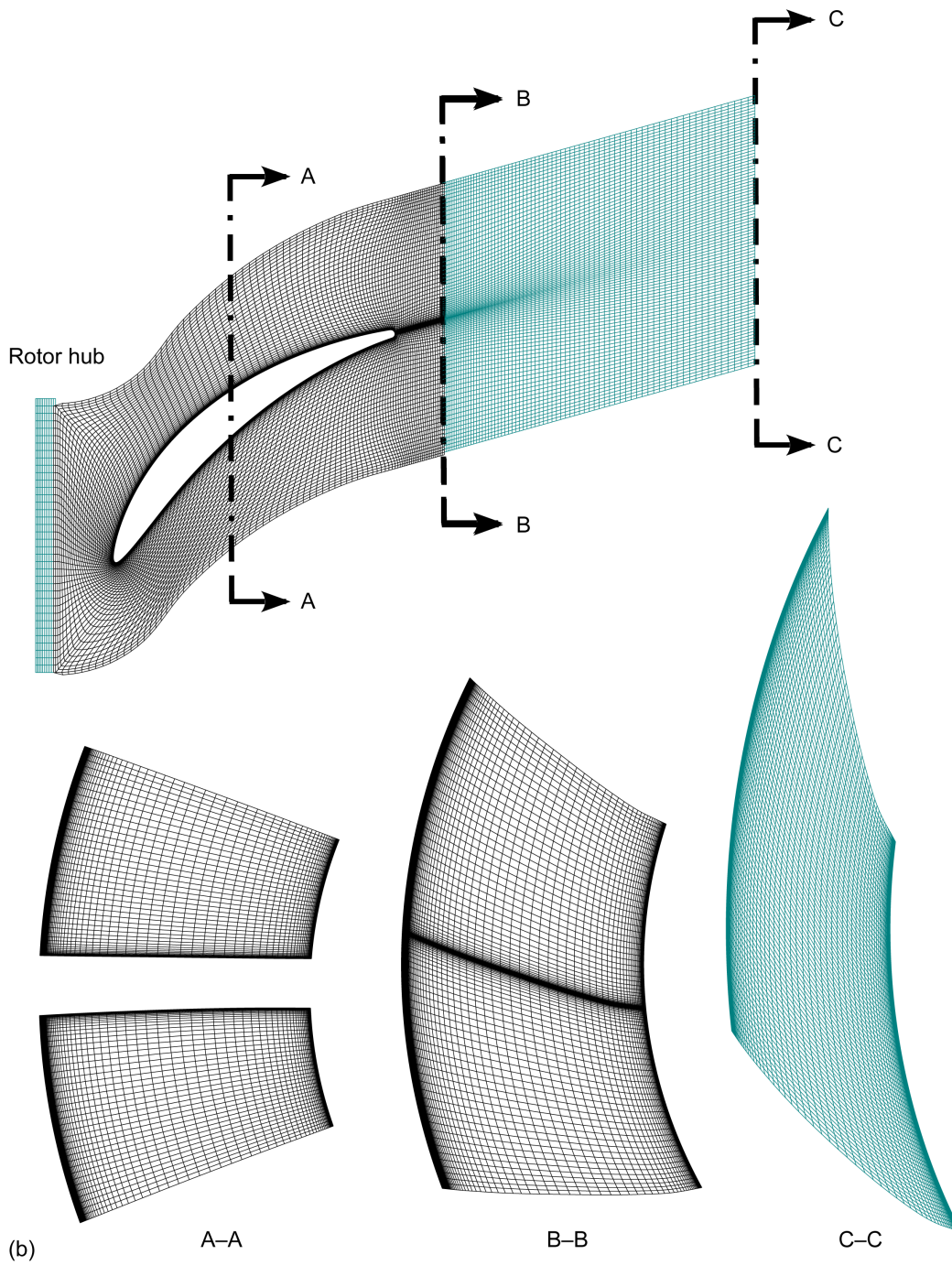


Figure 11.—Concluded. (b) An axial-circumferential mesh plot of the rotor grid at the hub.

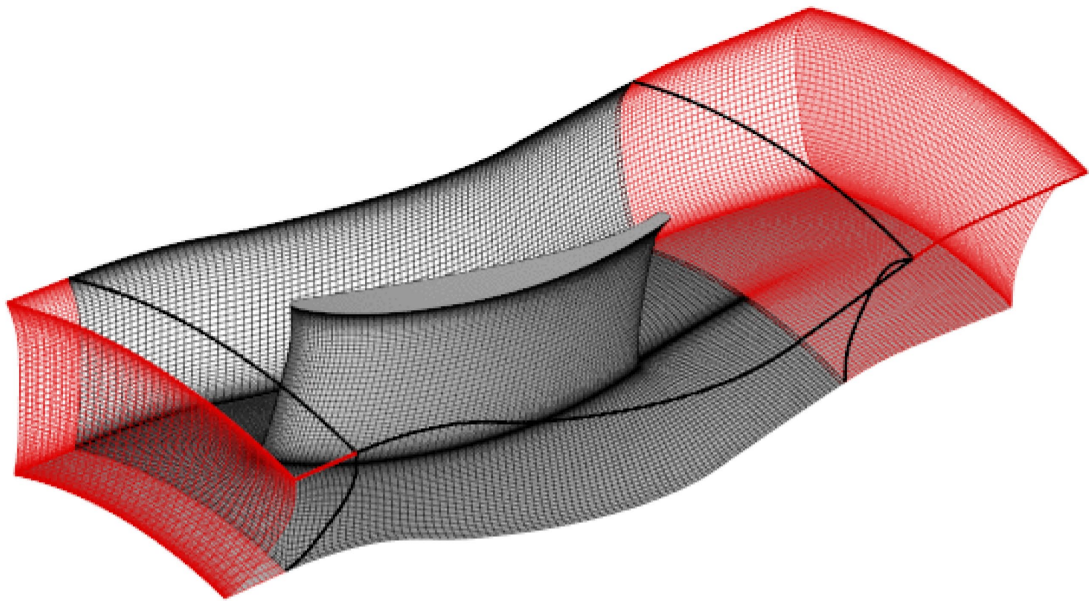


Figure 12.—Three-dimensional view of stator grid blocks.

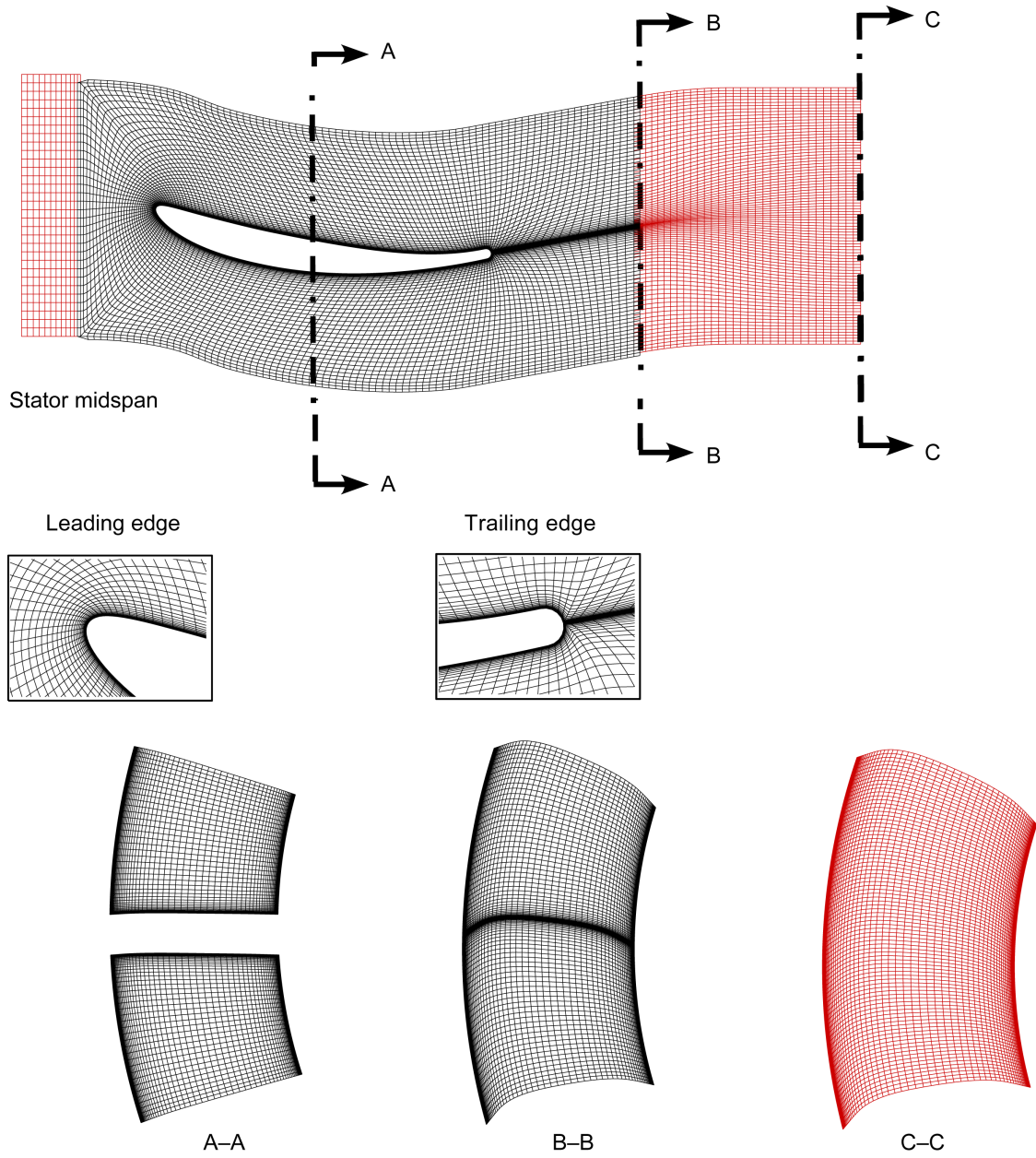


Figure 13.—Stator grid mesh plots.

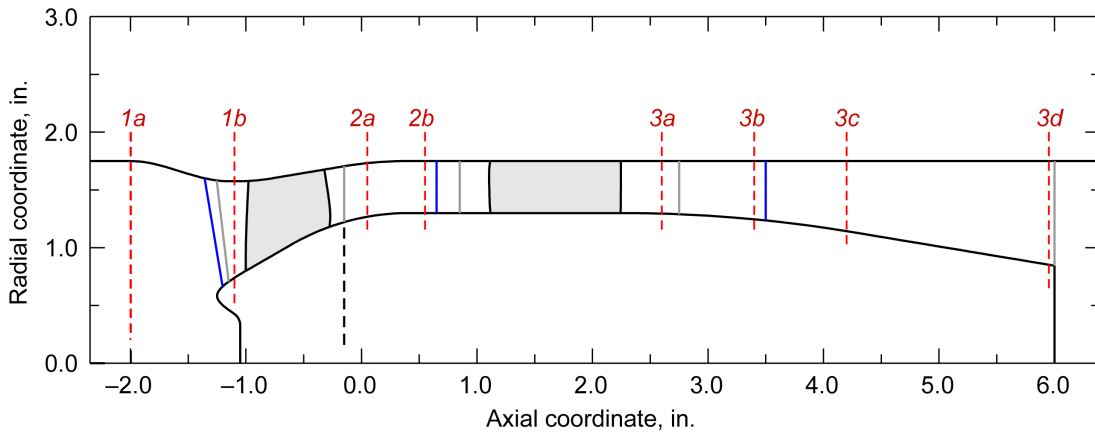


Figure 14.—Axial station locations.

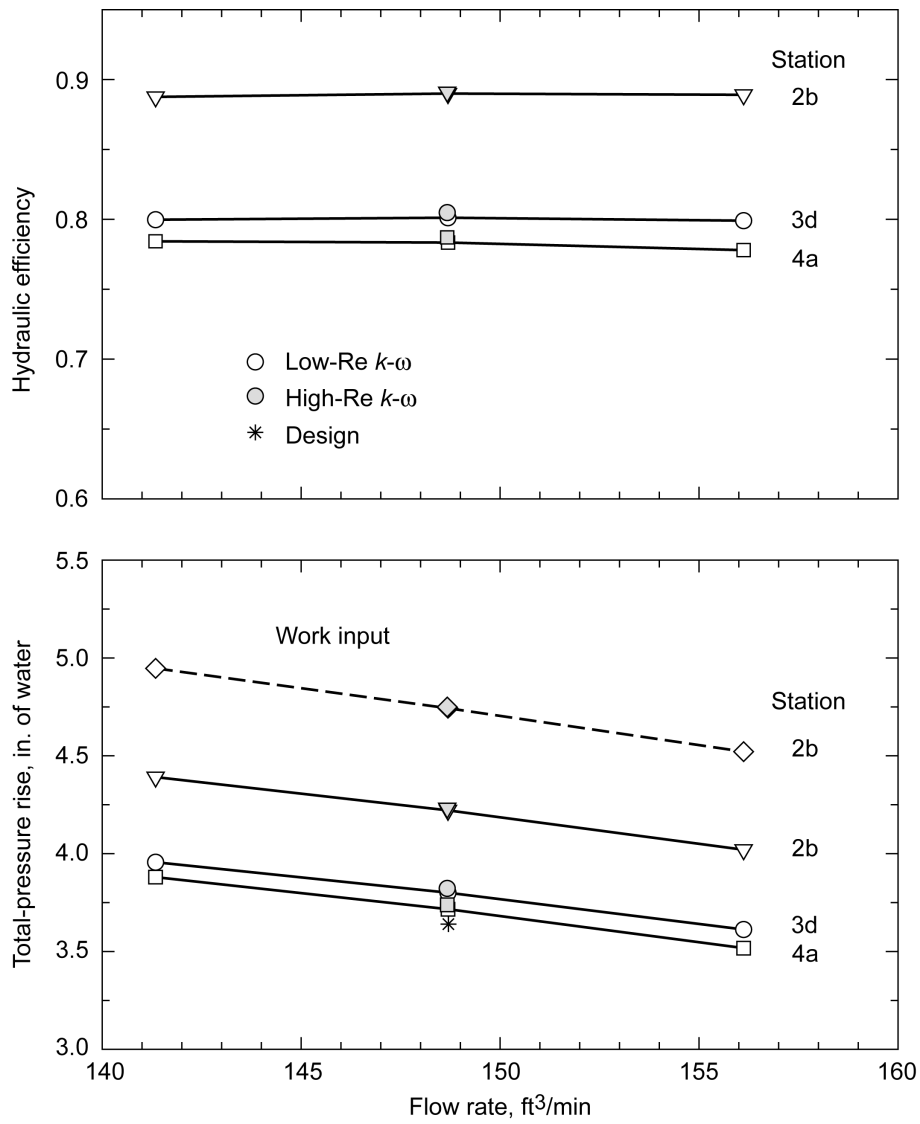


Figure 15.—Fan performance map.

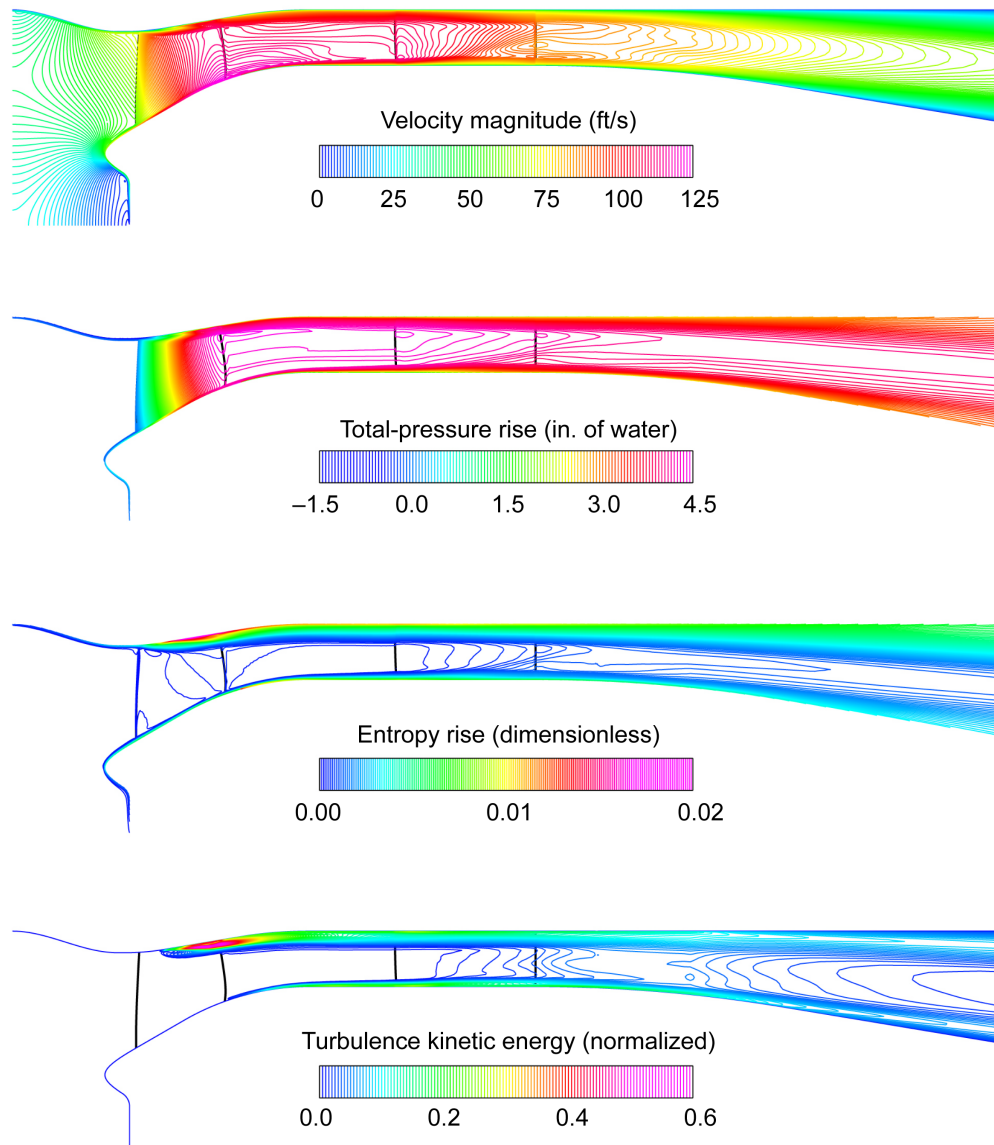


Figure 16.—Computed fan system flow field for design operating conditions; circumferentially averaged flow; low-Re turbulence model.

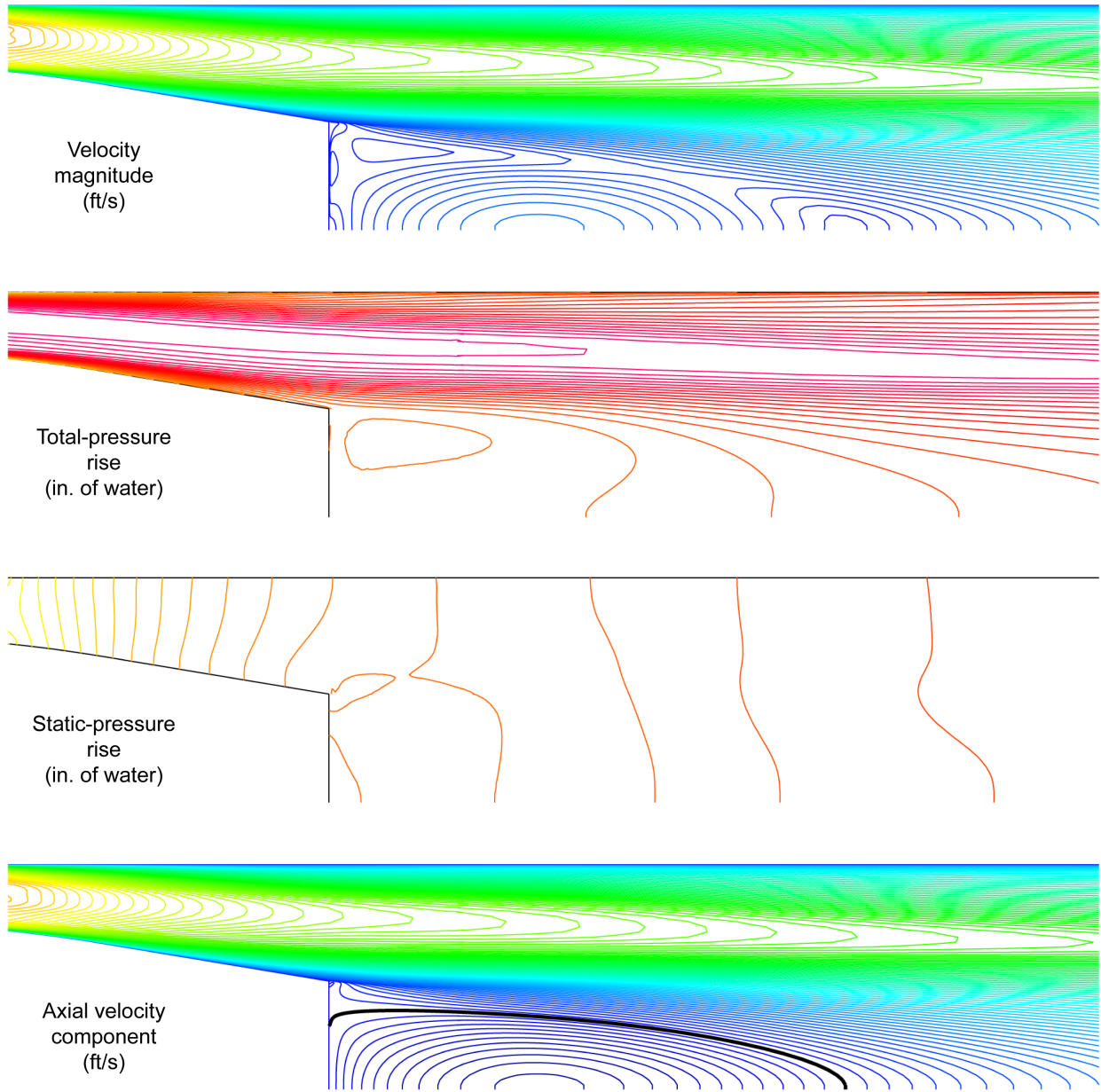


Figure 17.—Computed system exit flow field for design operating conditions; low-Re turbulence model.

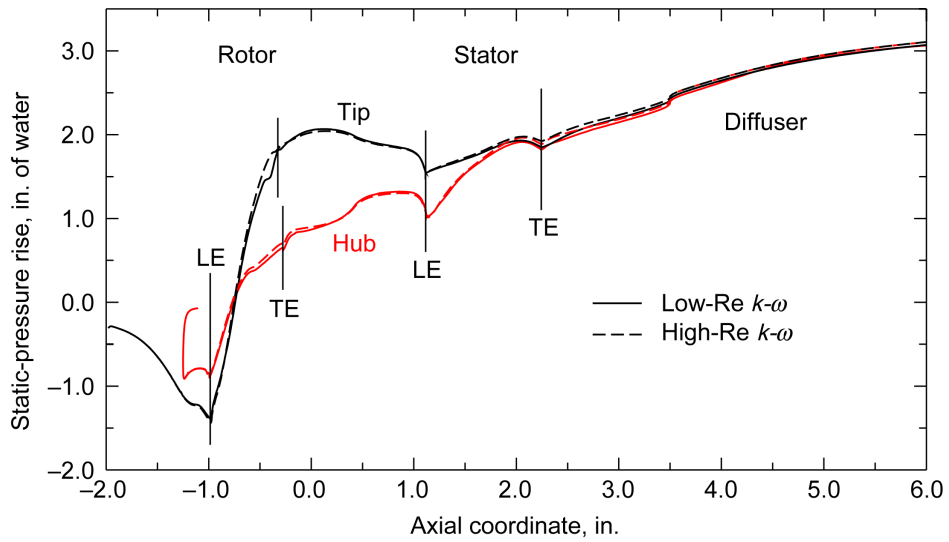


Figure 18.—Fan system endwall static-pressure rise for design operating conditions (circumferentially averaged flow).

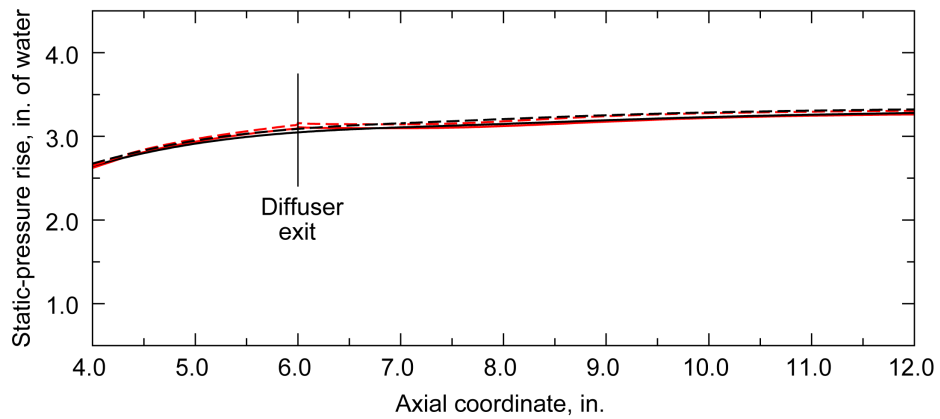


Figure 19.—System exit endwall static-pressure rise for design operating conditions.

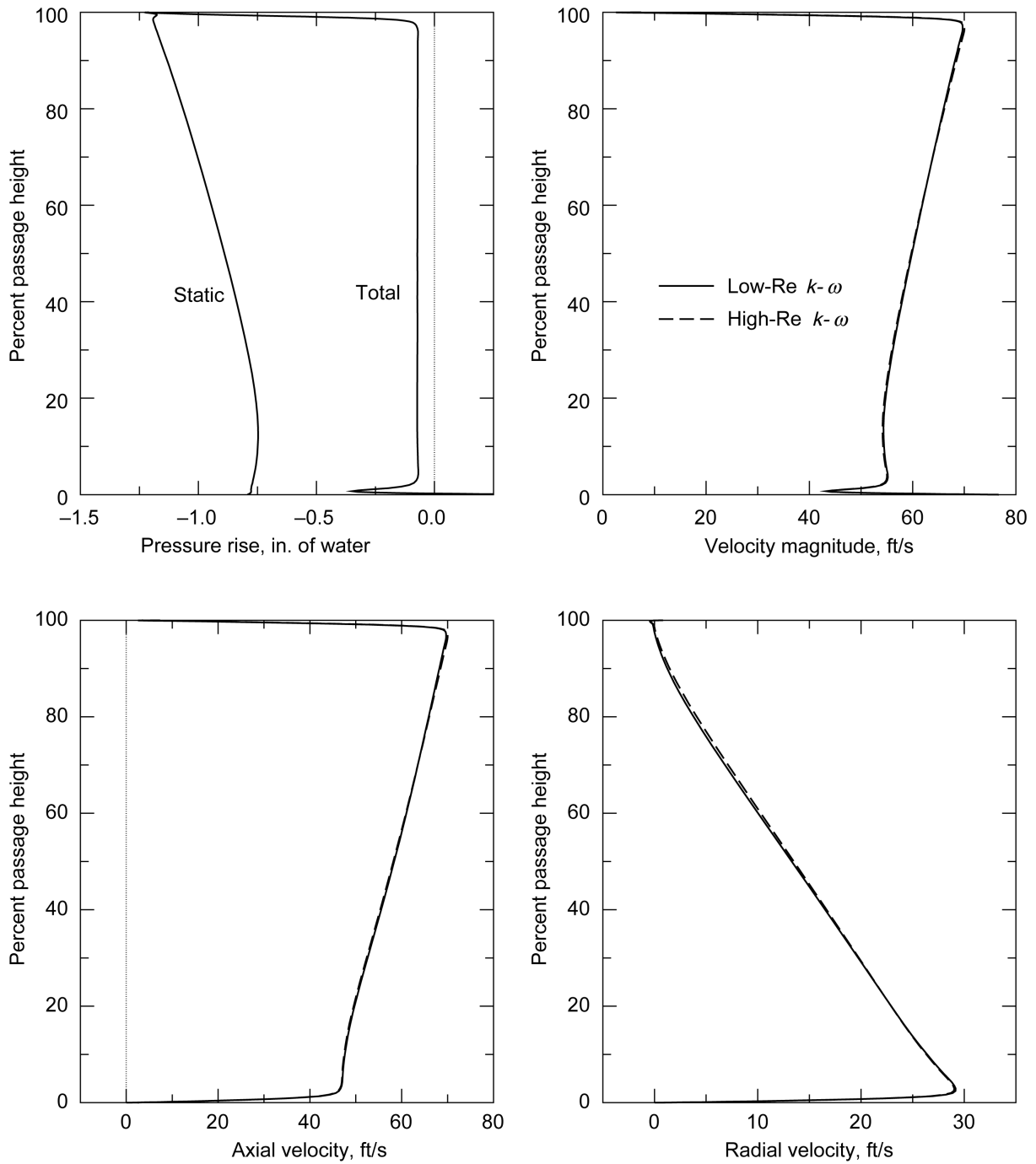


Figure 20.—Station 1b flow property profiles (circumferentially averaged flow).

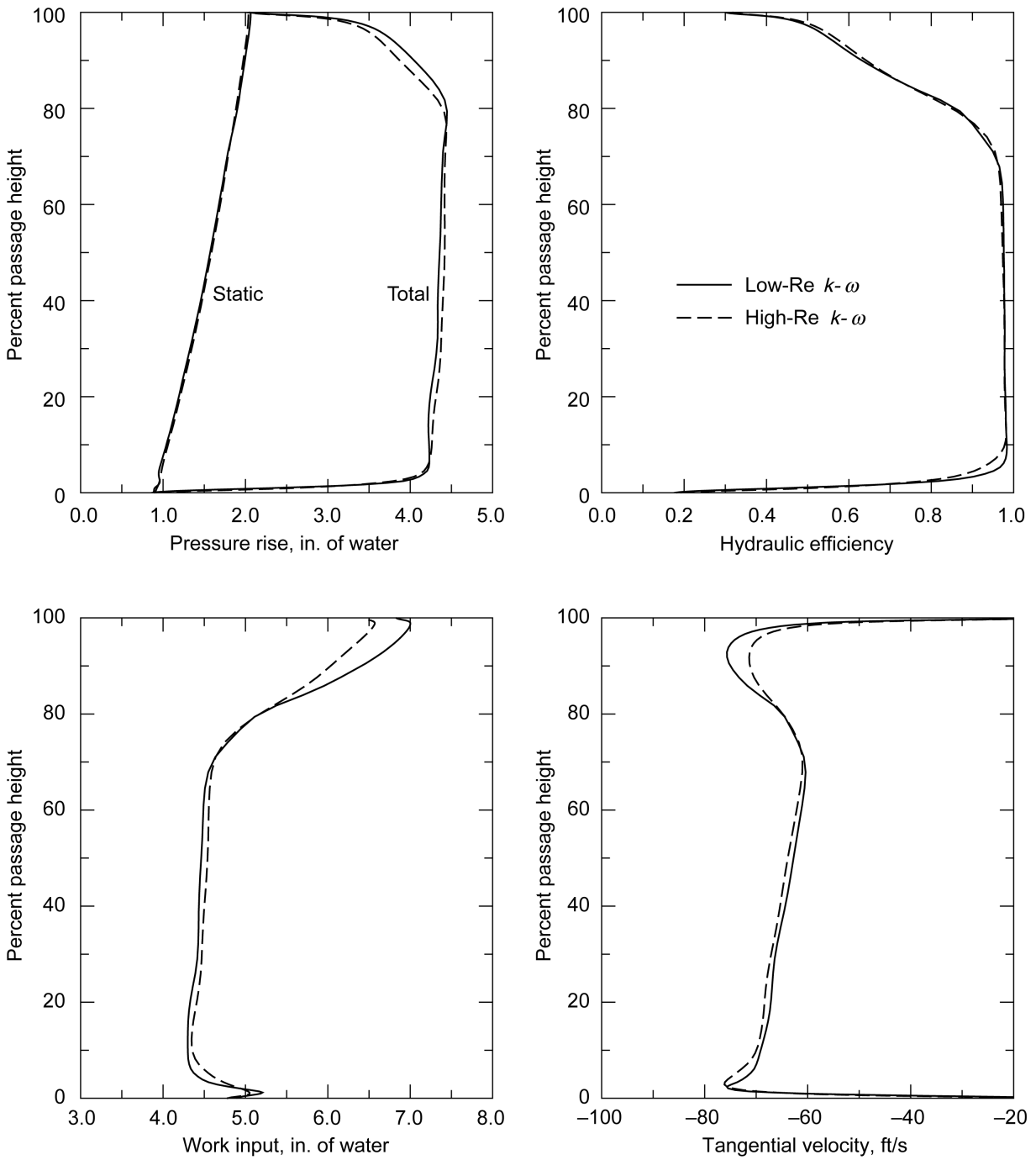


Figure 21(a).—Station 2a flow property profiles (circumferentially averaged flow).

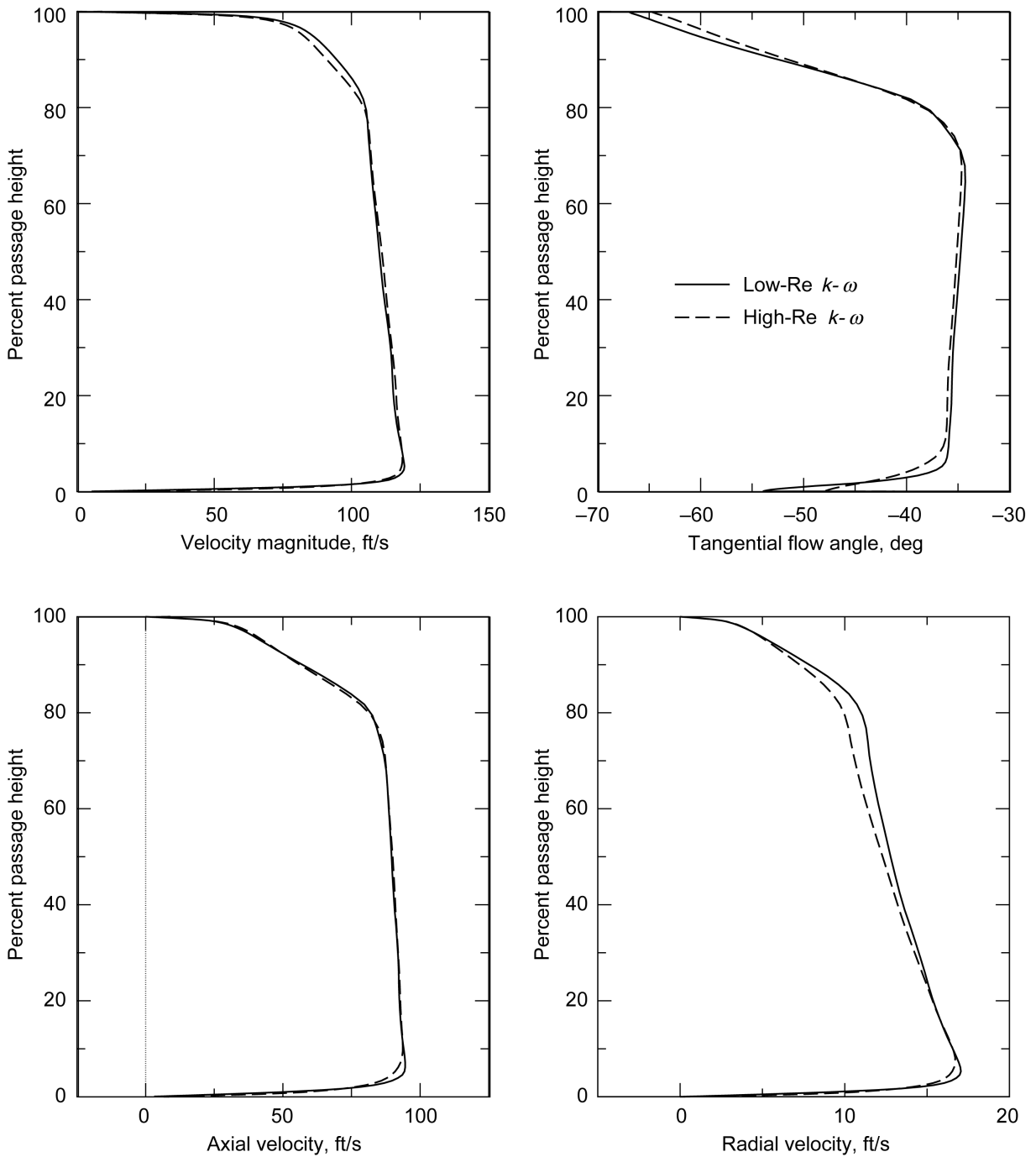


Figure 21(b).—Station 2a flow property profiles (circumferentially averaged flow).

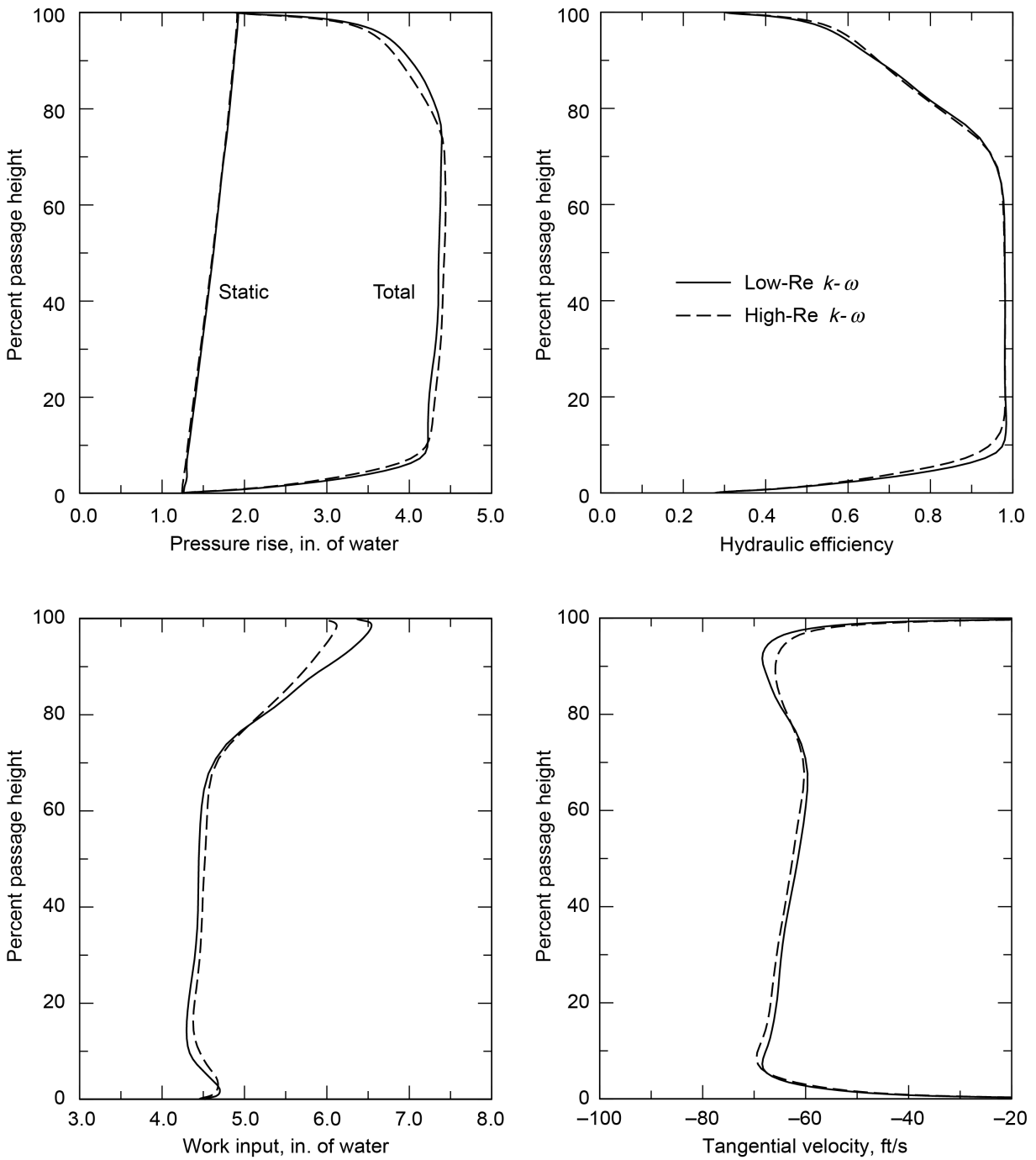


Figure 22(a).—Station 2b flow property profiles (circumferentially averaged flow).

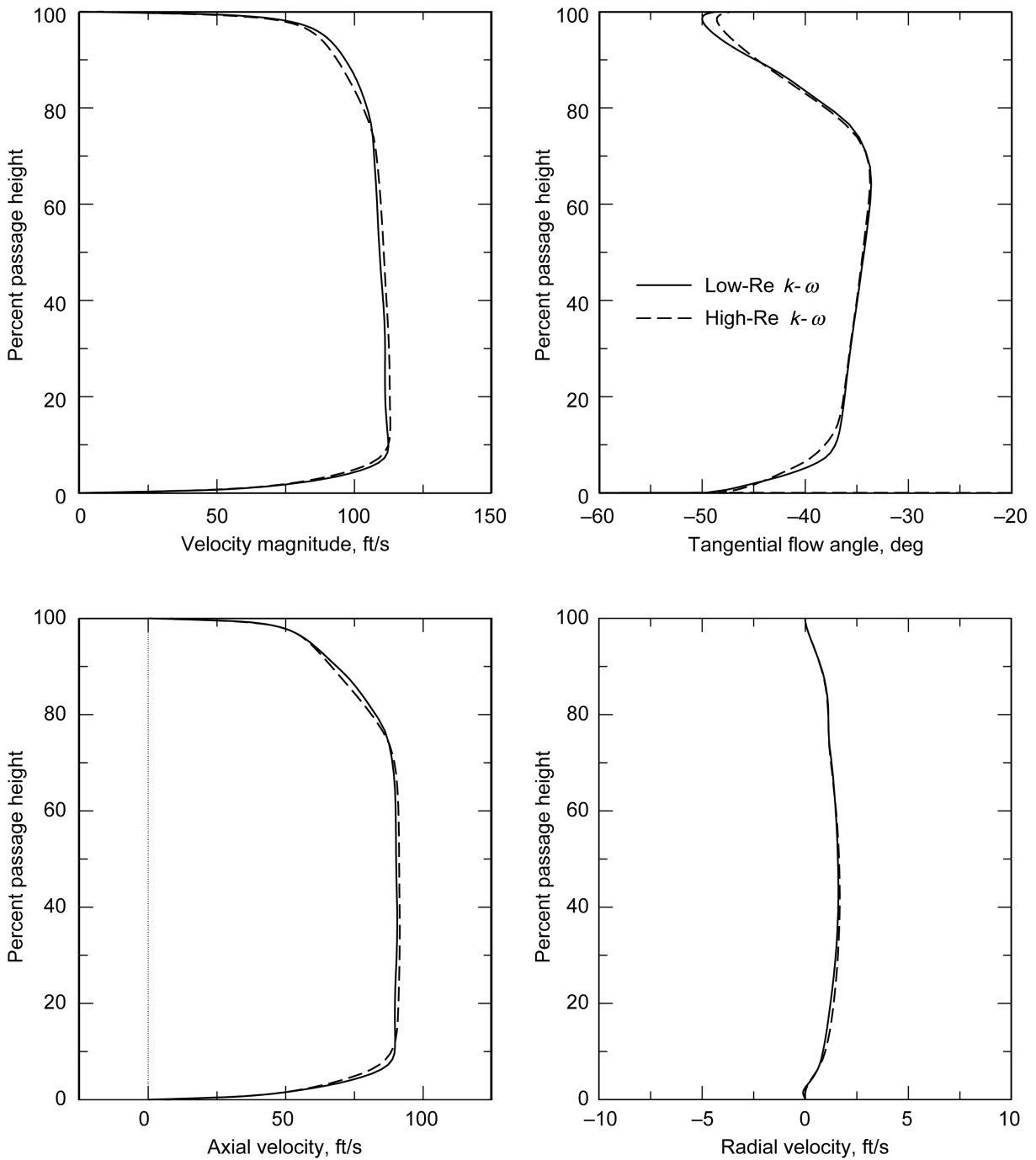


Figure 22(b).—Station 2a flow property profiles (circumferentially averaged flow).

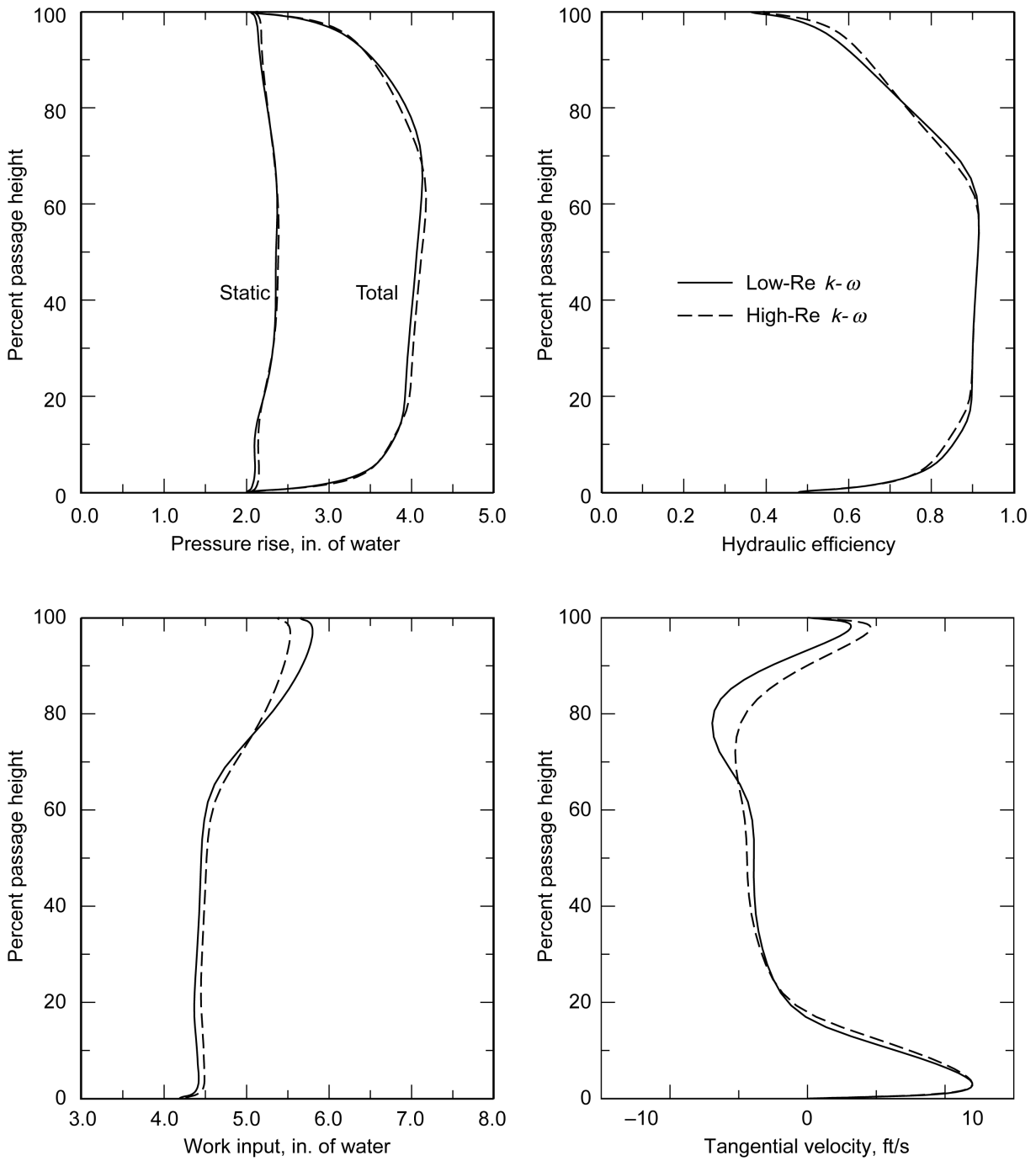


Figure 23(a).—Station 3a flow property profiles (circumferentially averaged flow).

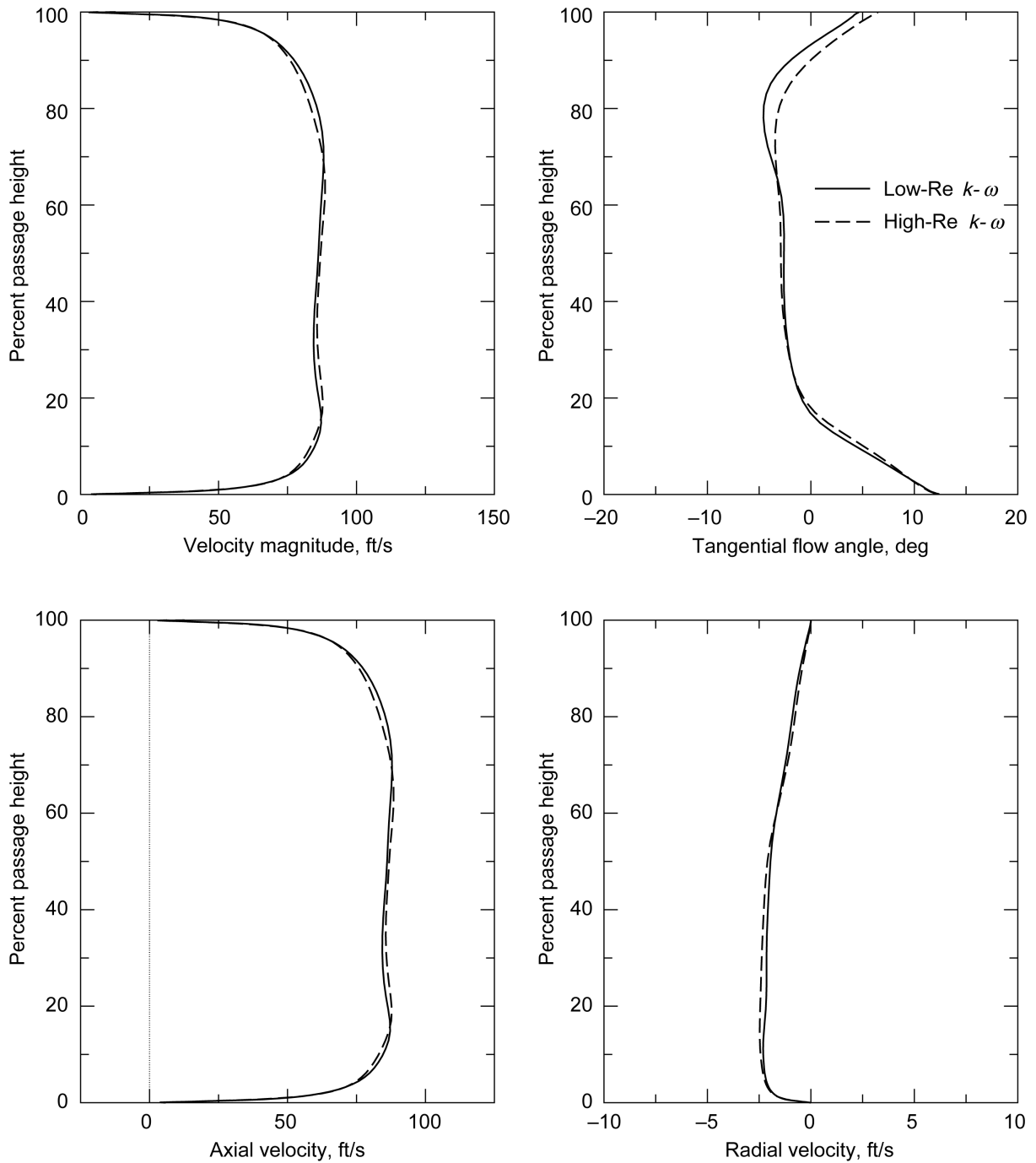


Figure 23(b).—Station 3a flow property profiles (circumferentially averaged flow).

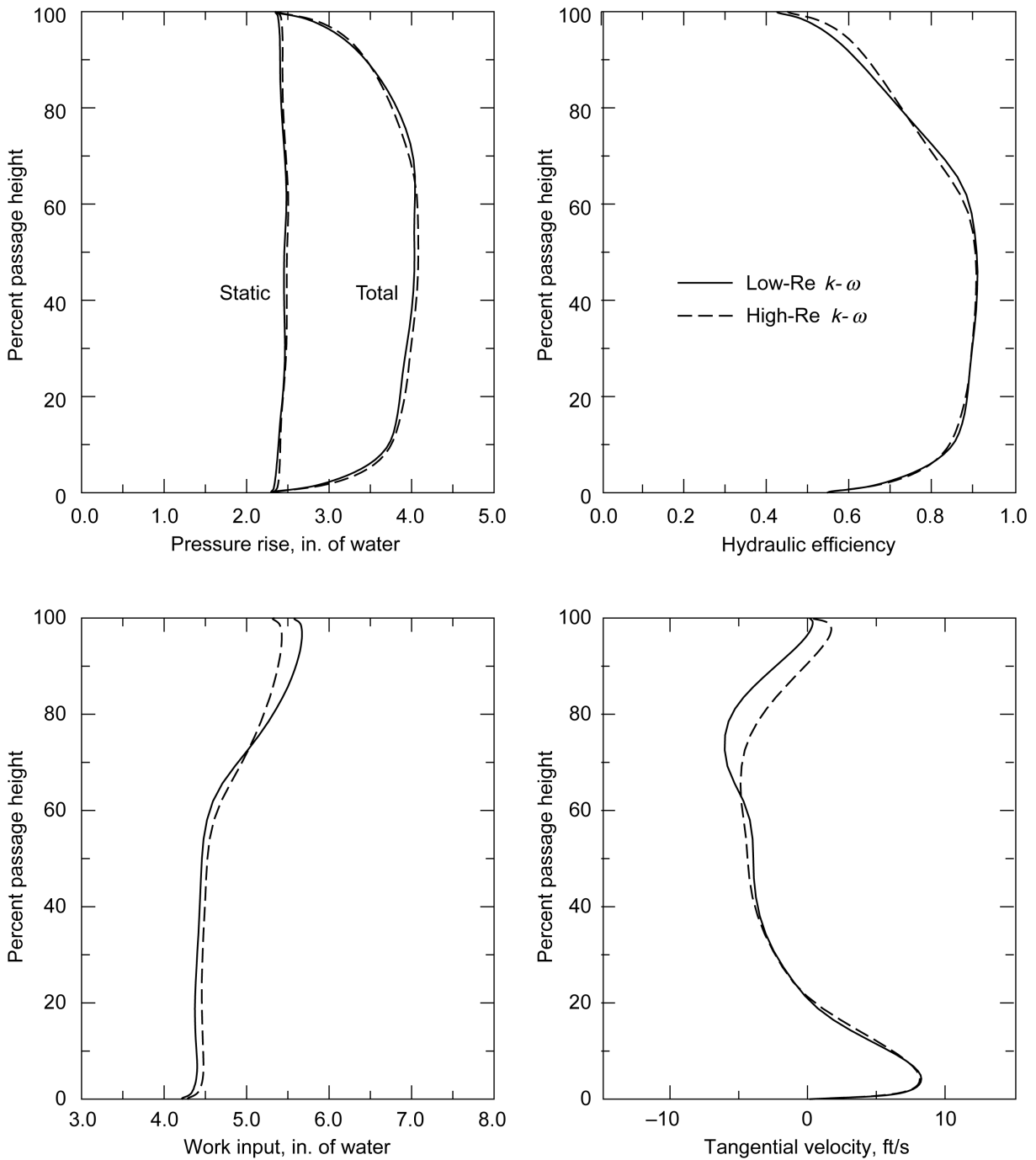


Figure 24(a).—Station 3b flow property profiles (circumferentially averaged flow).

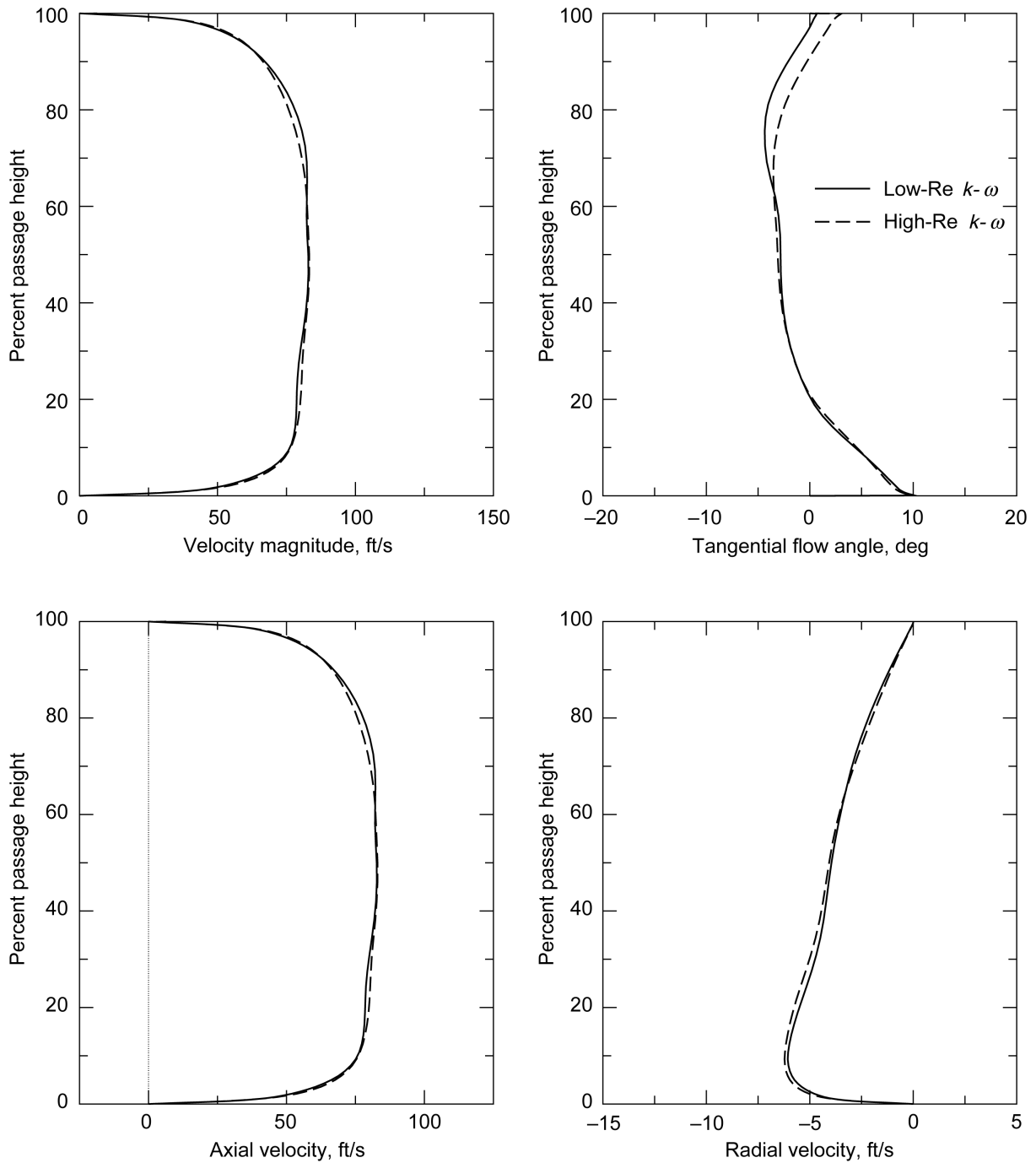


Figure 24(b).—Station 3b flow property profiles (circumferentially averaged flow).

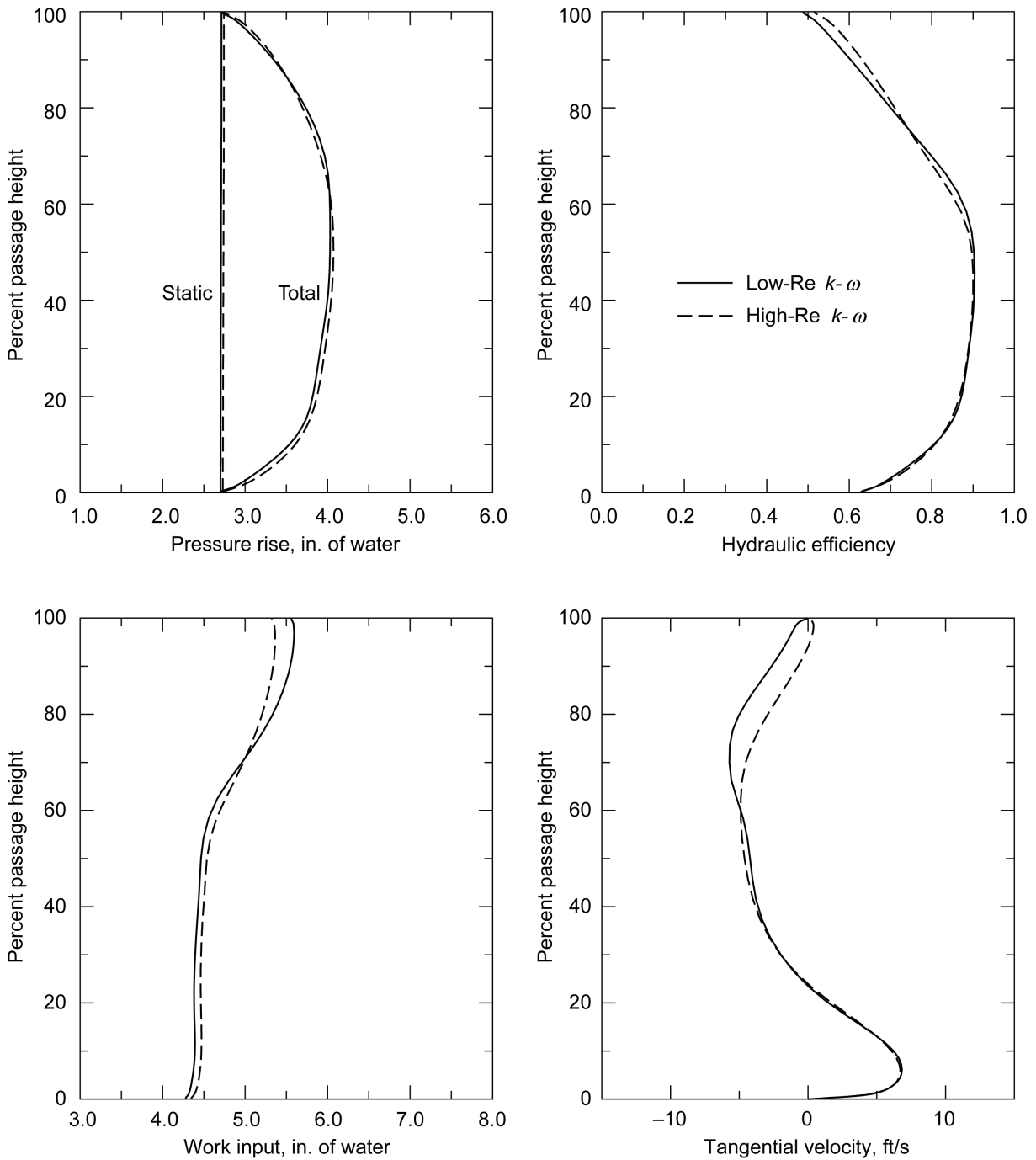


Figure 25(a).—Station 3c flow property profiles (circumferentially averaged flow).

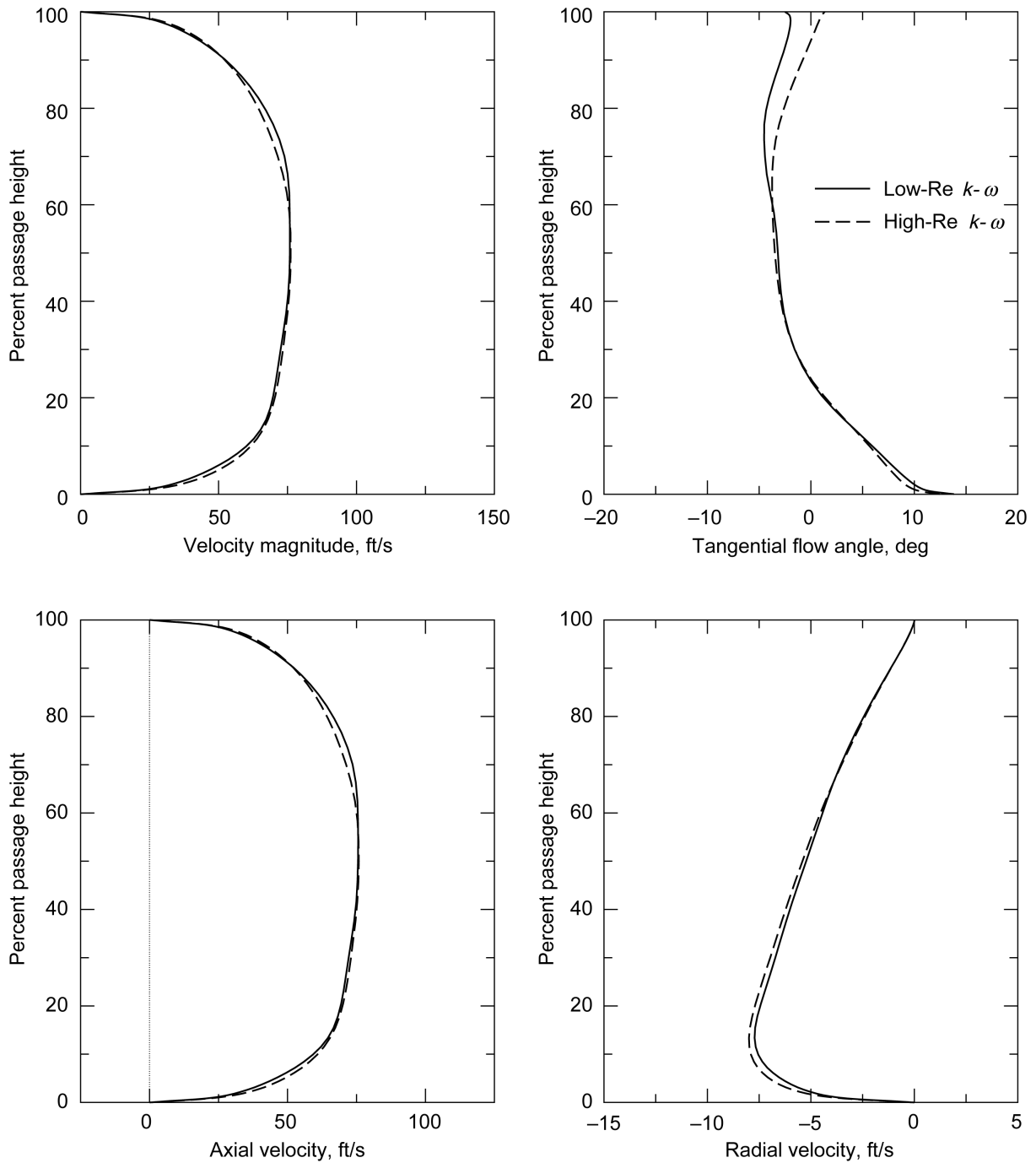


Figure 25(b).—Station 3c flow property profiles (circumferentially averaged flow).

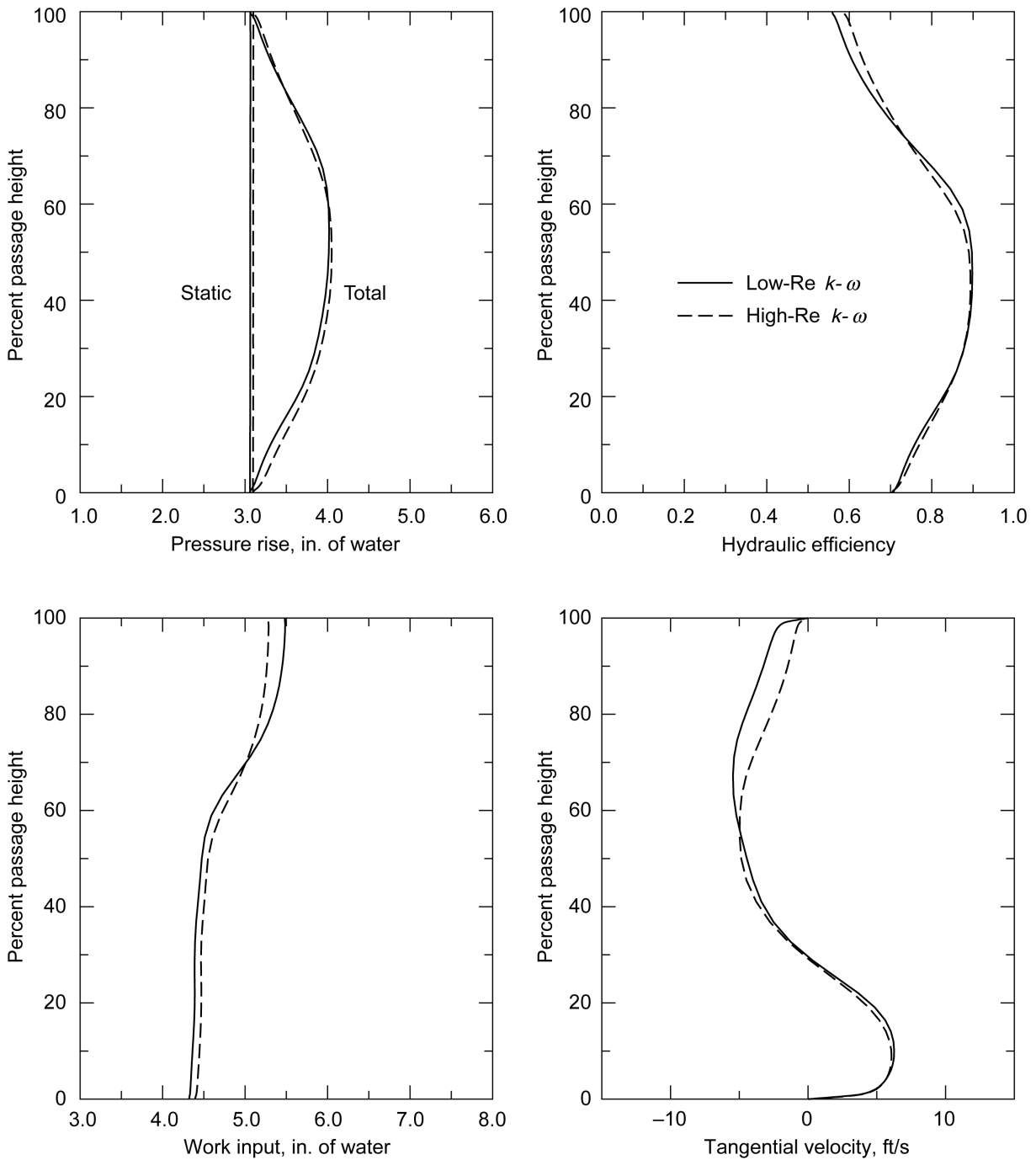


Figure 26(a).—Station 3d flow property profiles (circumferentially averaged flow).

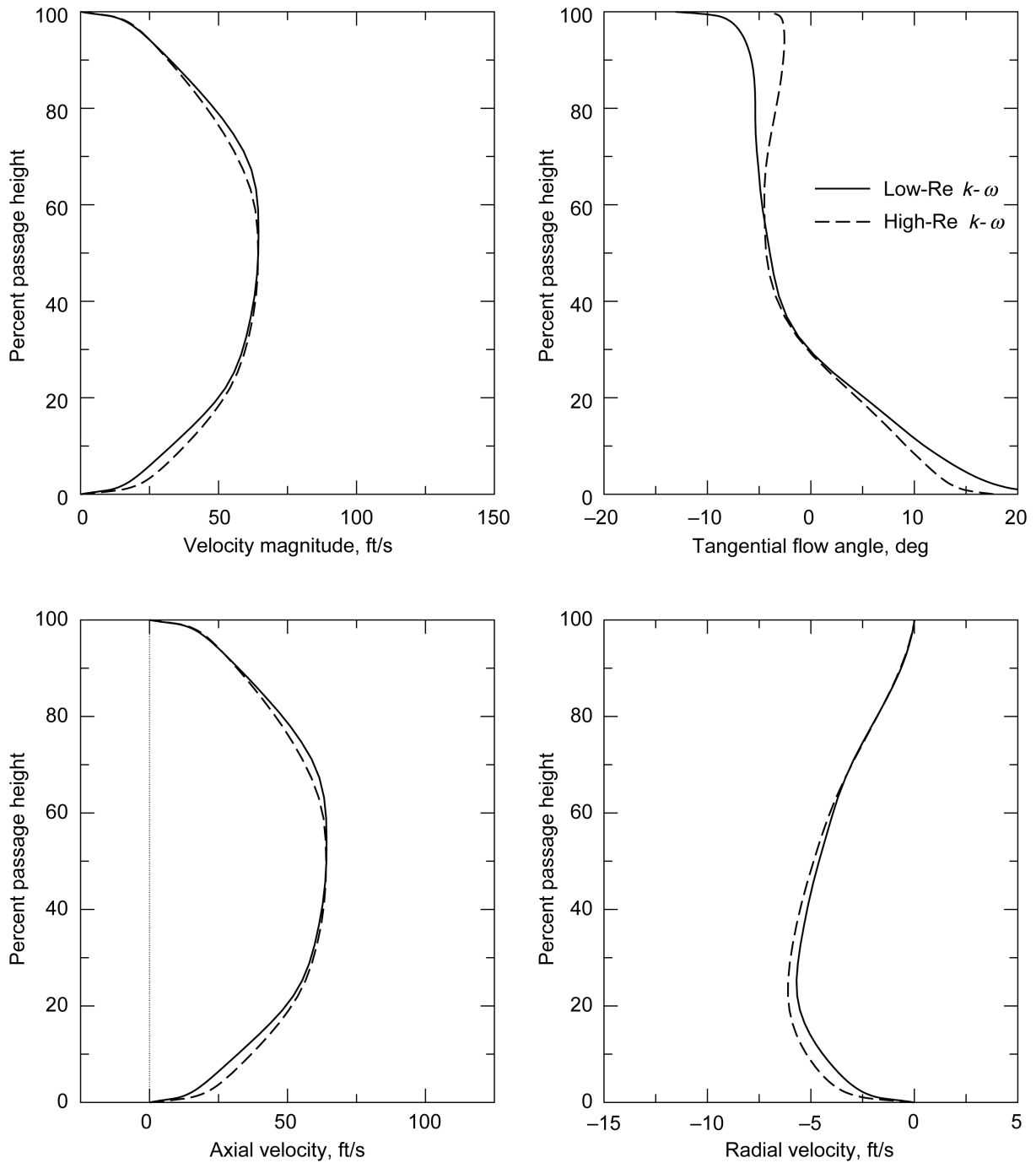


Figure 26(b).—Station 3d flow property profiles (circumferentially averaged flow).

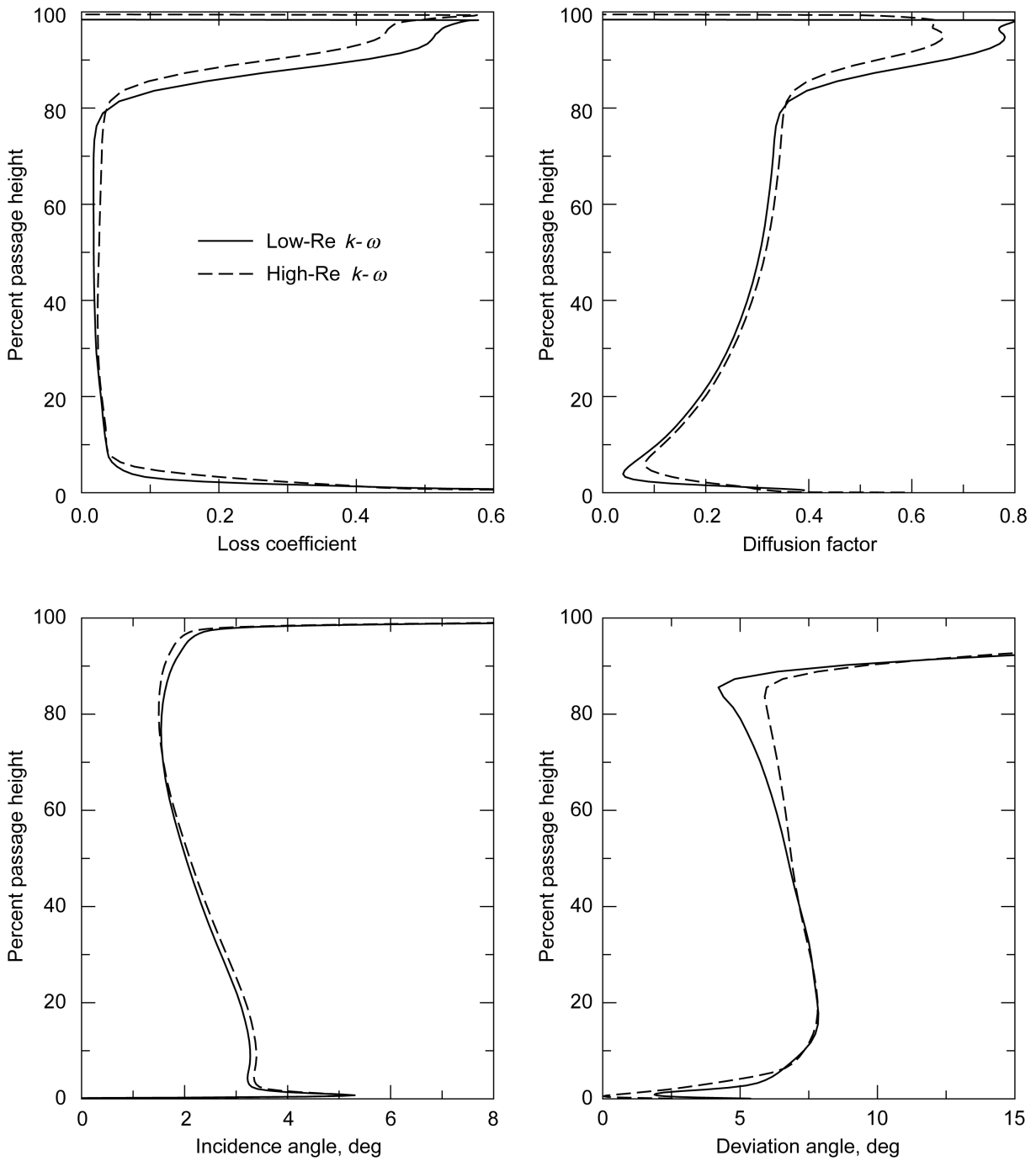


Figure 27(a).—Spanwise distributions of rotor blade row aerodynamic parameters.

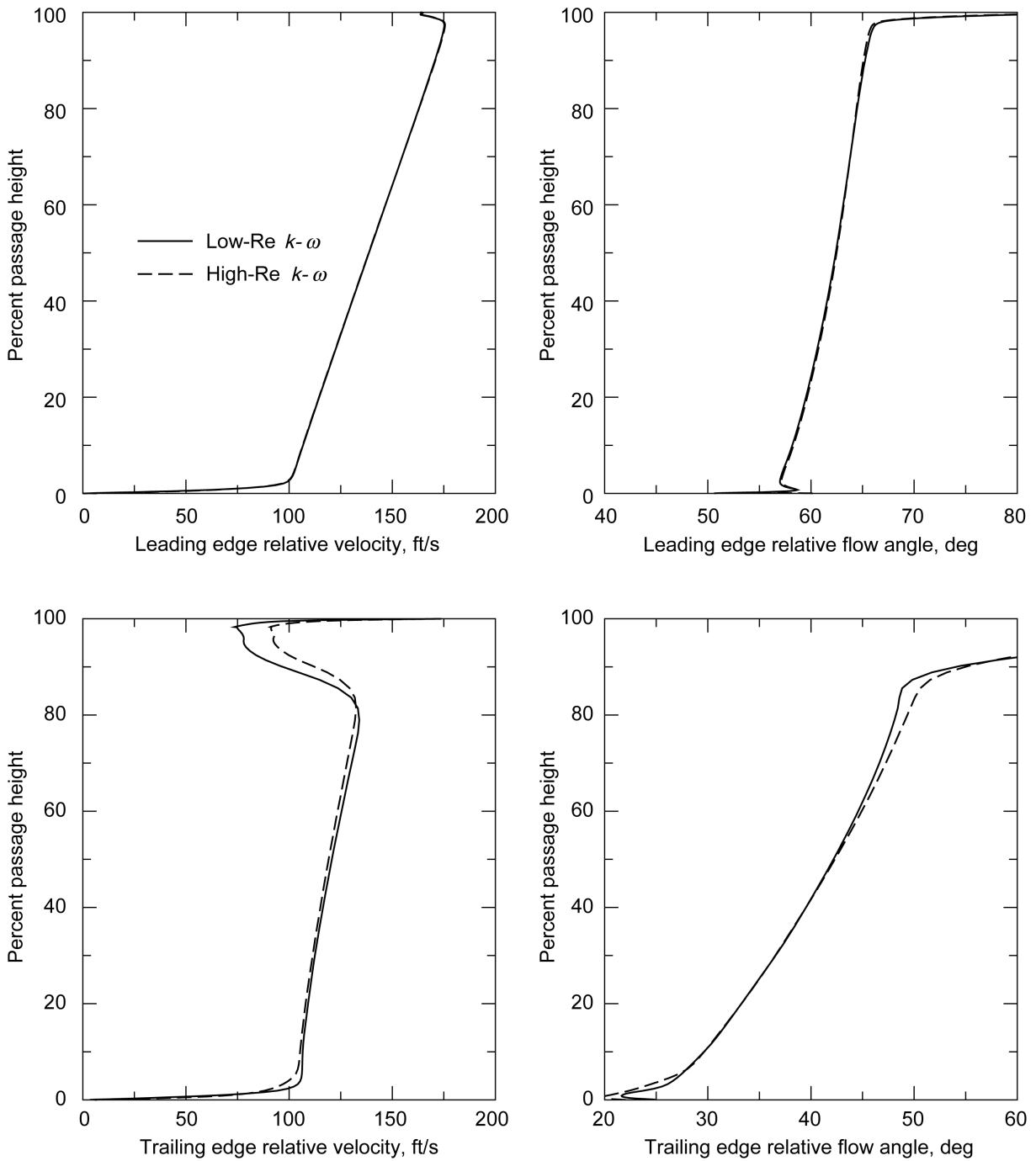


Figure 27(b).—Spanwise distributions of rotor blade row aerodynamic parameters.

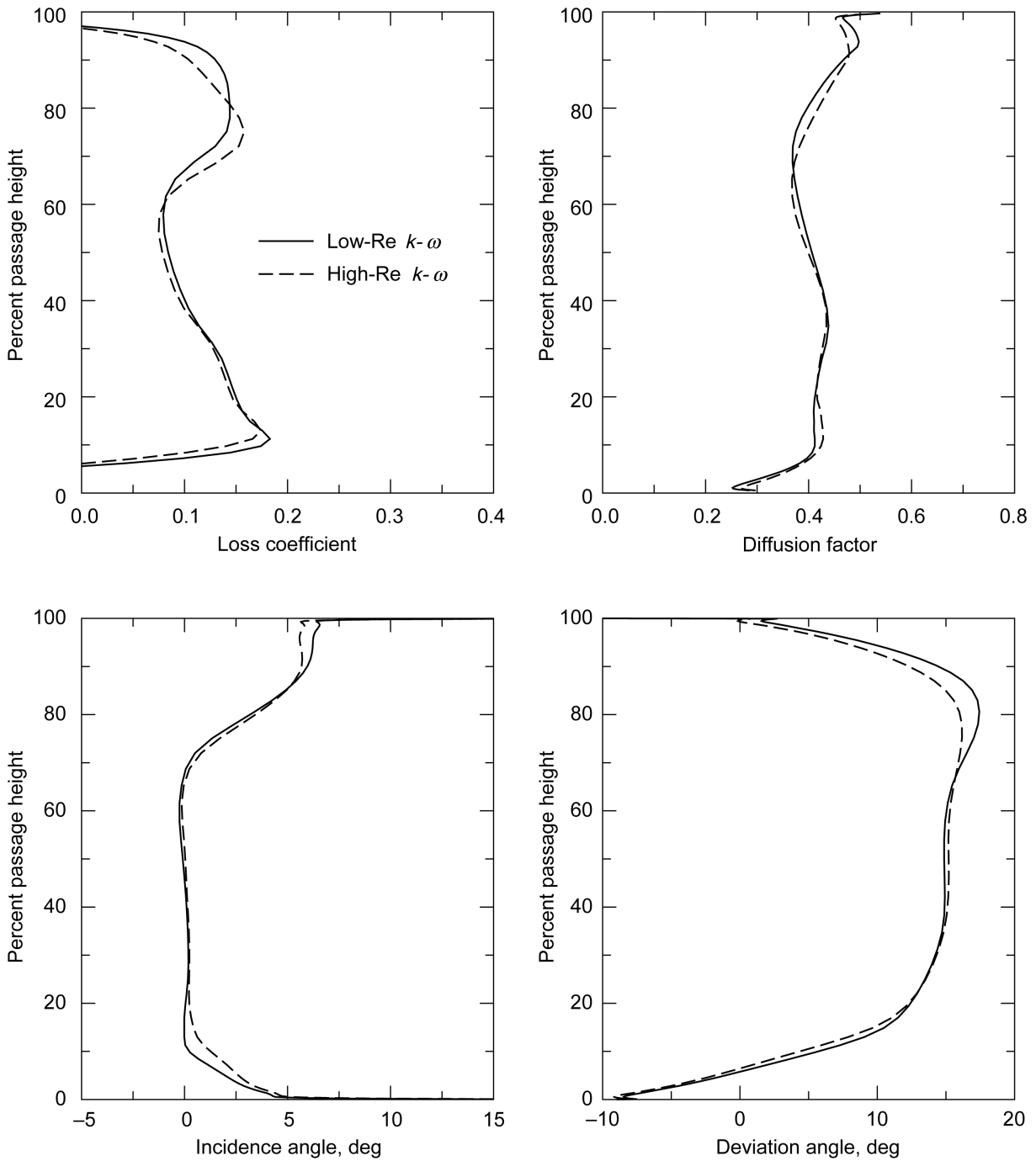


Figure 28(a).—Spanwise distributions of stator blade row aerodynamic parameters.

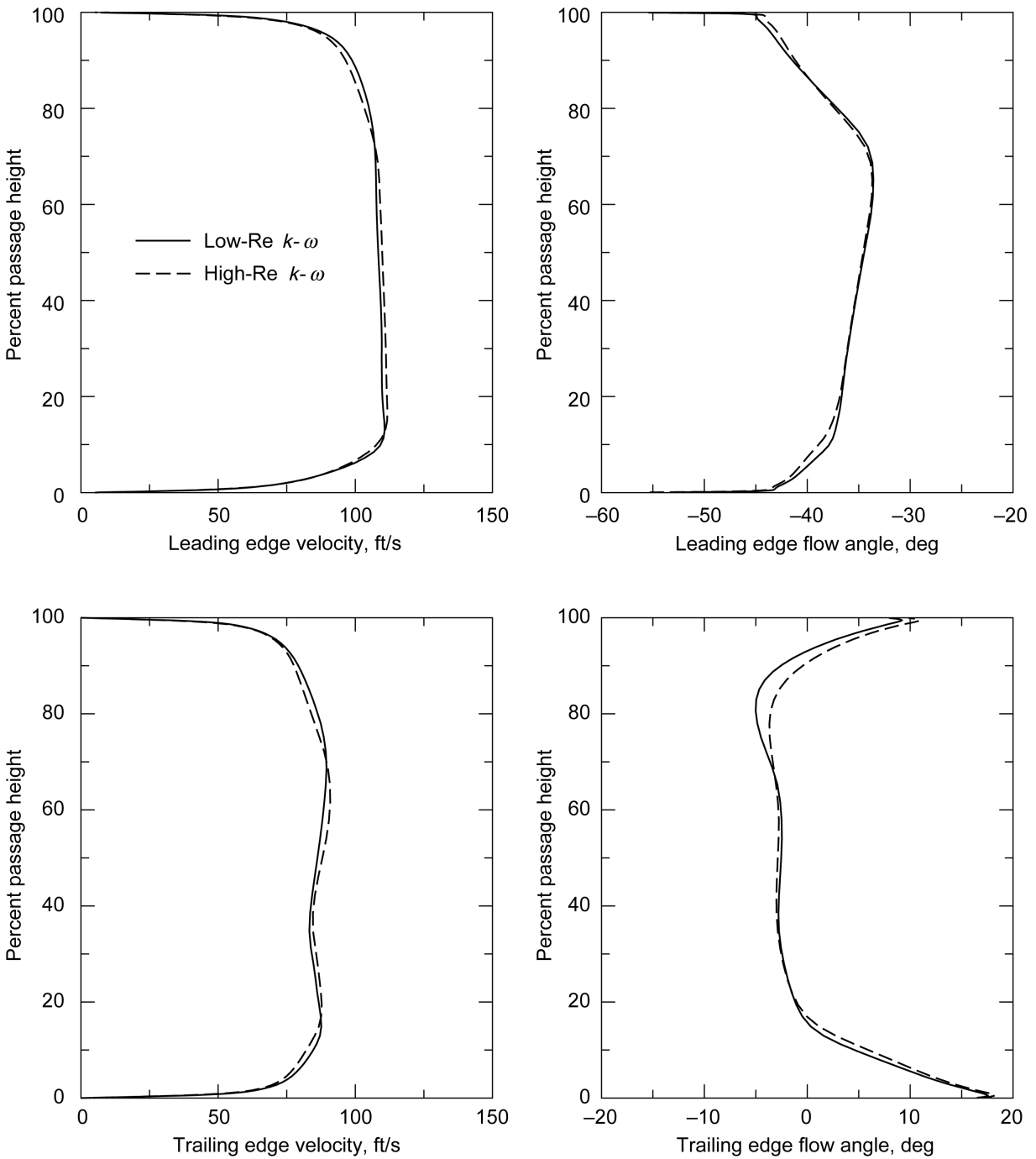


Figure 28(b).—Spanwise distributions of stator blade row aerodynamic parameters.

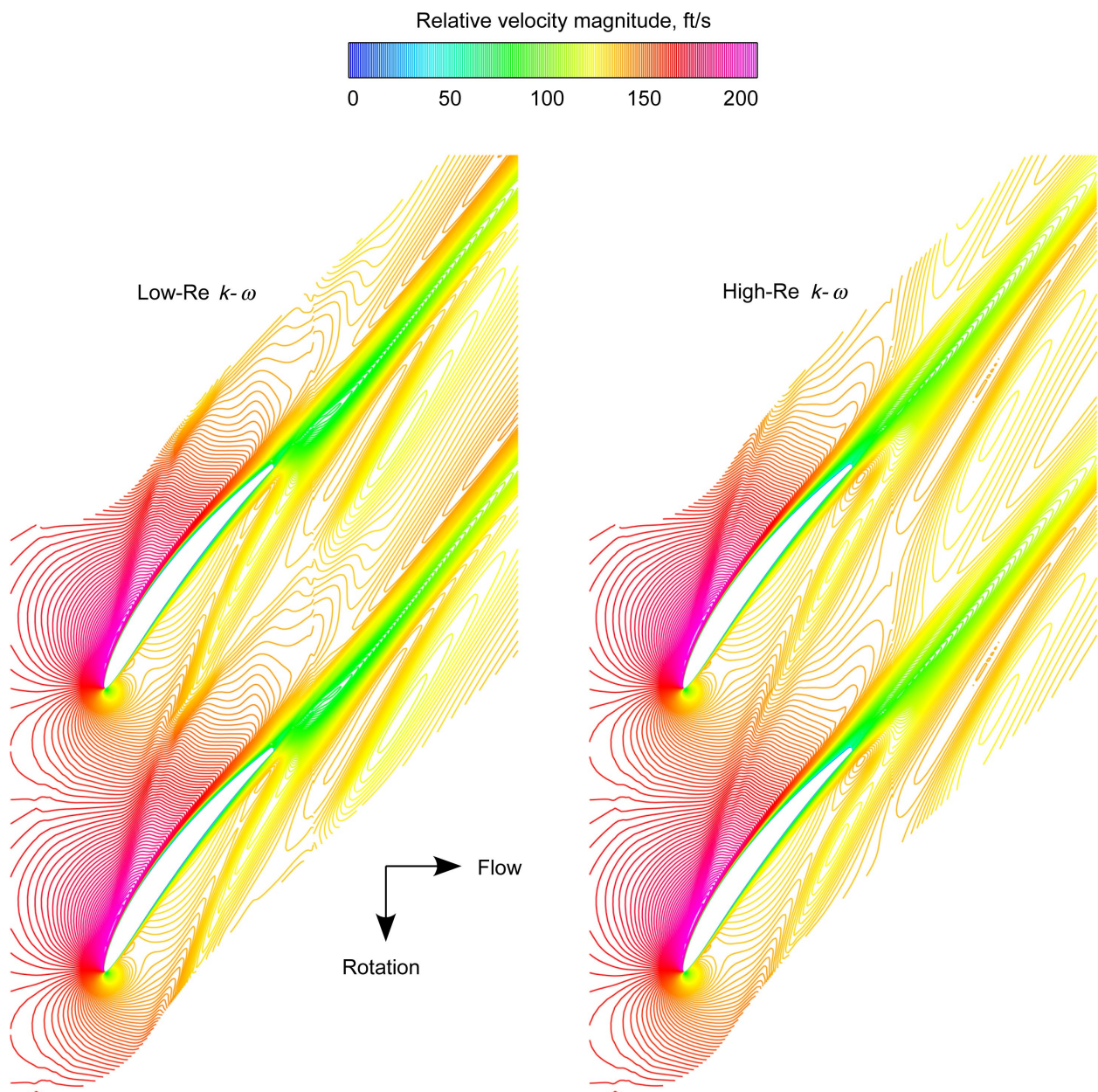


Figure 29(a).—Computed rotor flow field for design operating conditions; relative velocity magnitude; 85 percent of passage flow.

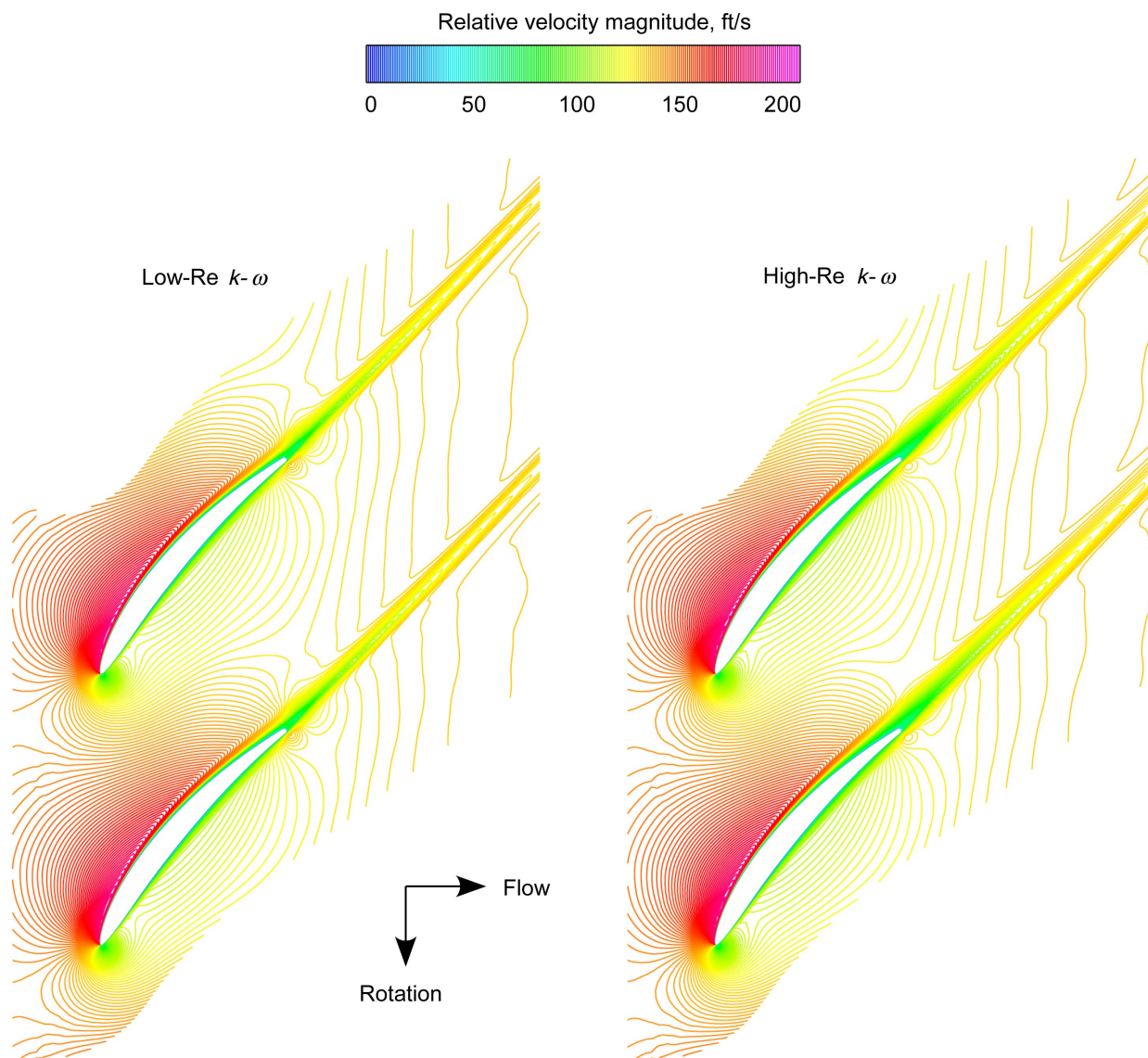


Figure 29(b).—Computed rotor flow field for design operating conditions; relative velocity magnitude; 50 percent of passage flow.

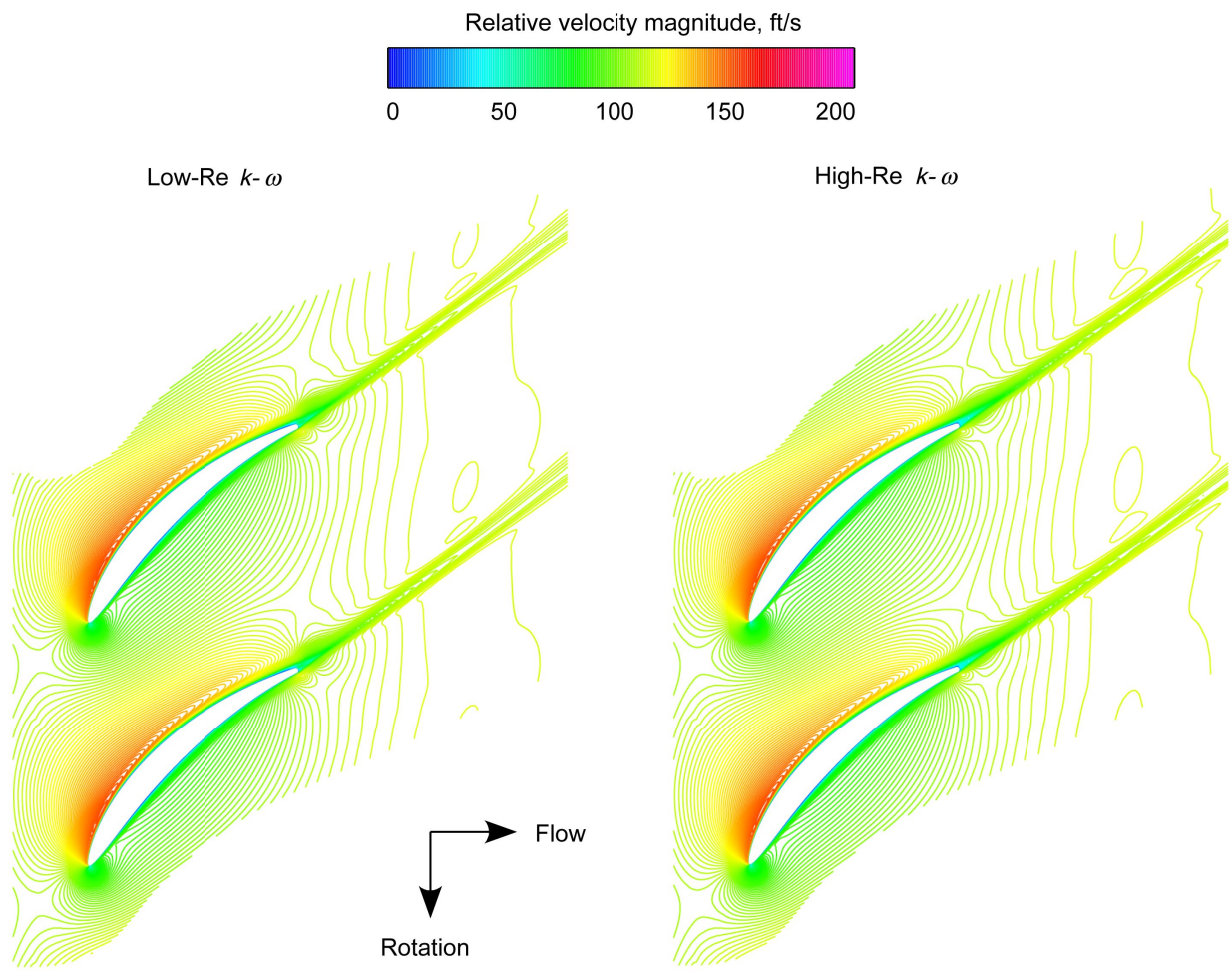


Figure 29(c).—Computed rotor flow field for design operating conditions; relative velocity magnitude; 15 percent of passage flow.

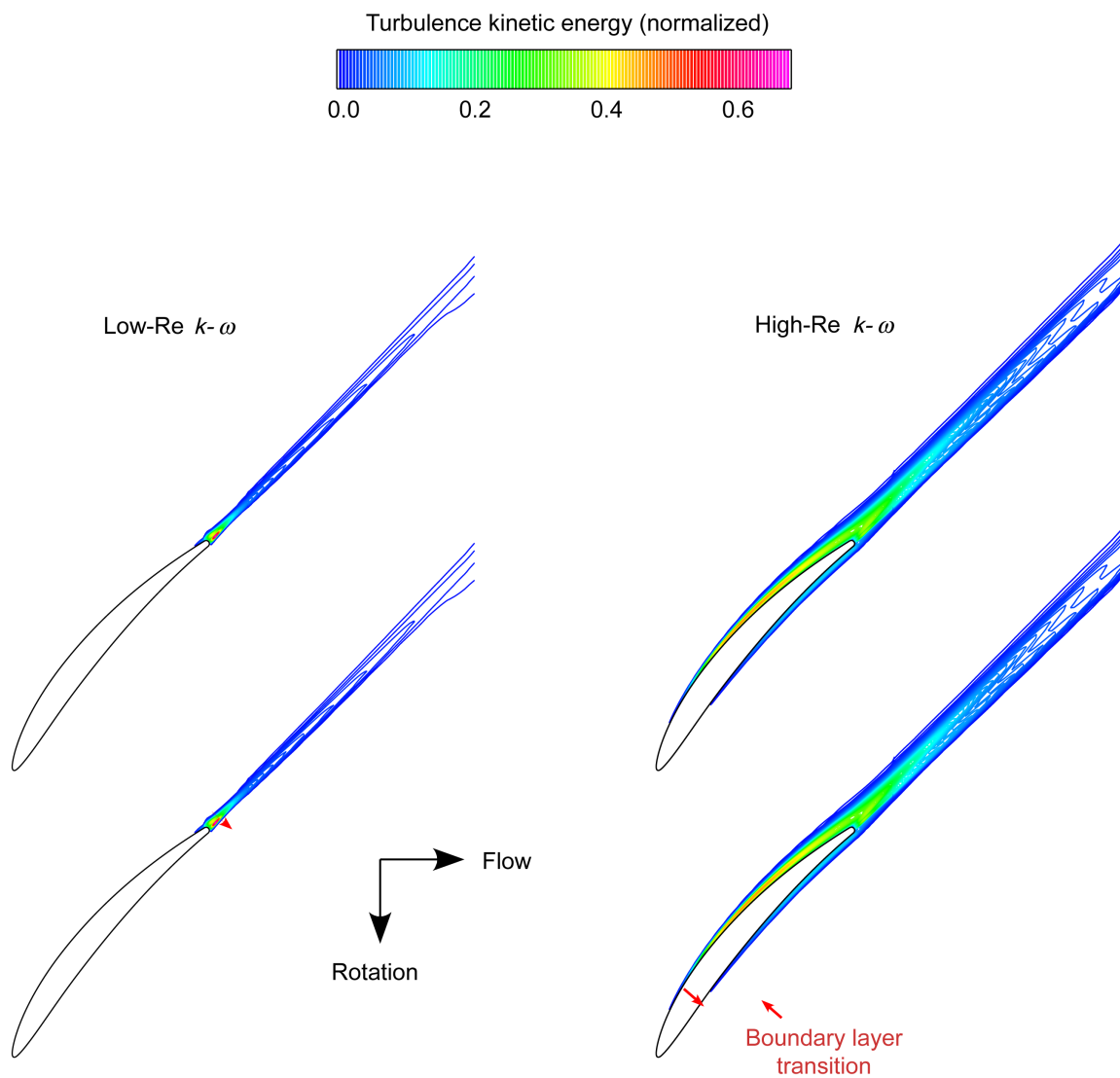


Figure 30.—Computed rotor flow field for design operating conditions; turbulence kinetic energy; 50 percent of passage flow.

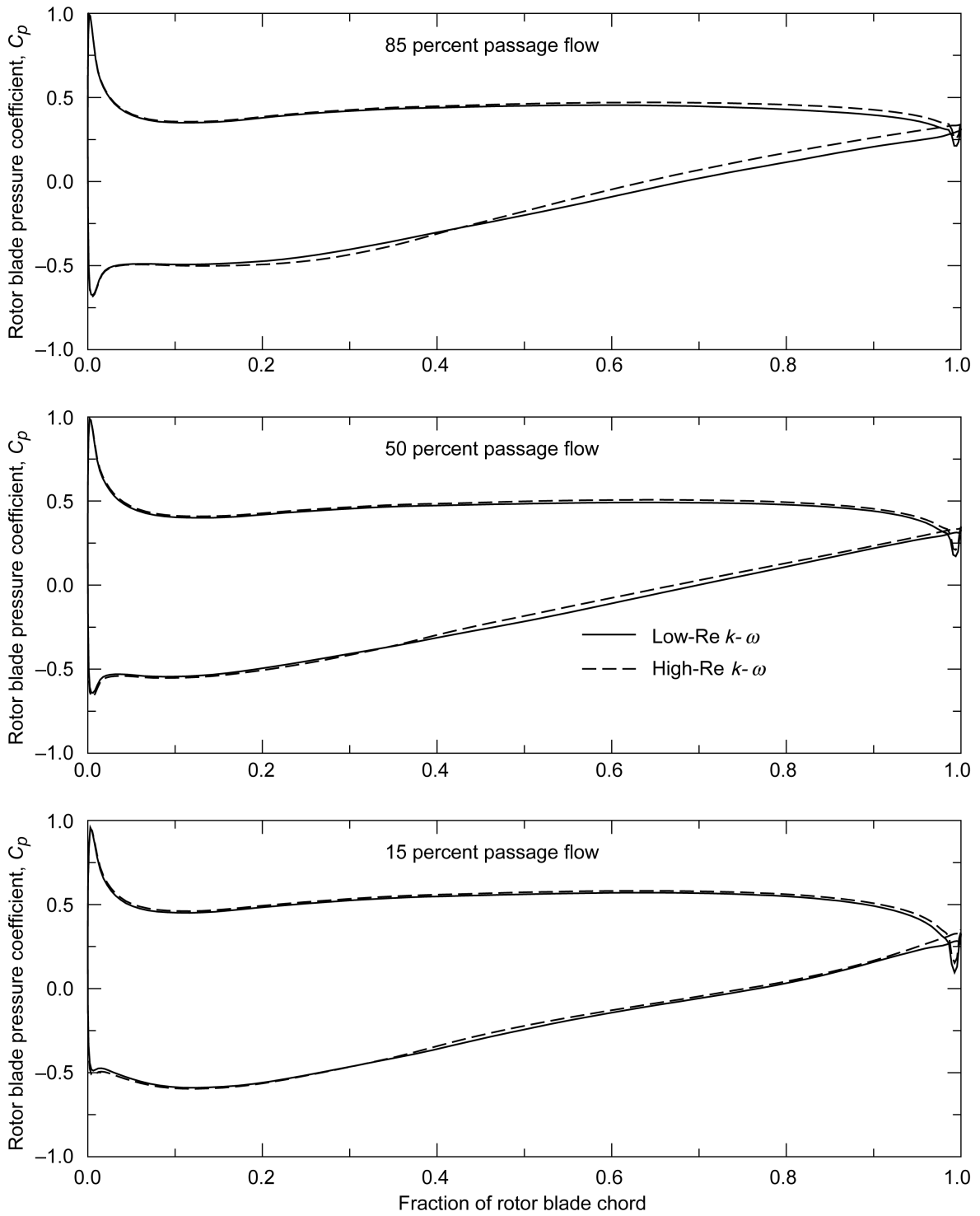


Figure 31.—Chordwise distributions of rotor blade surface pressure coefficient.

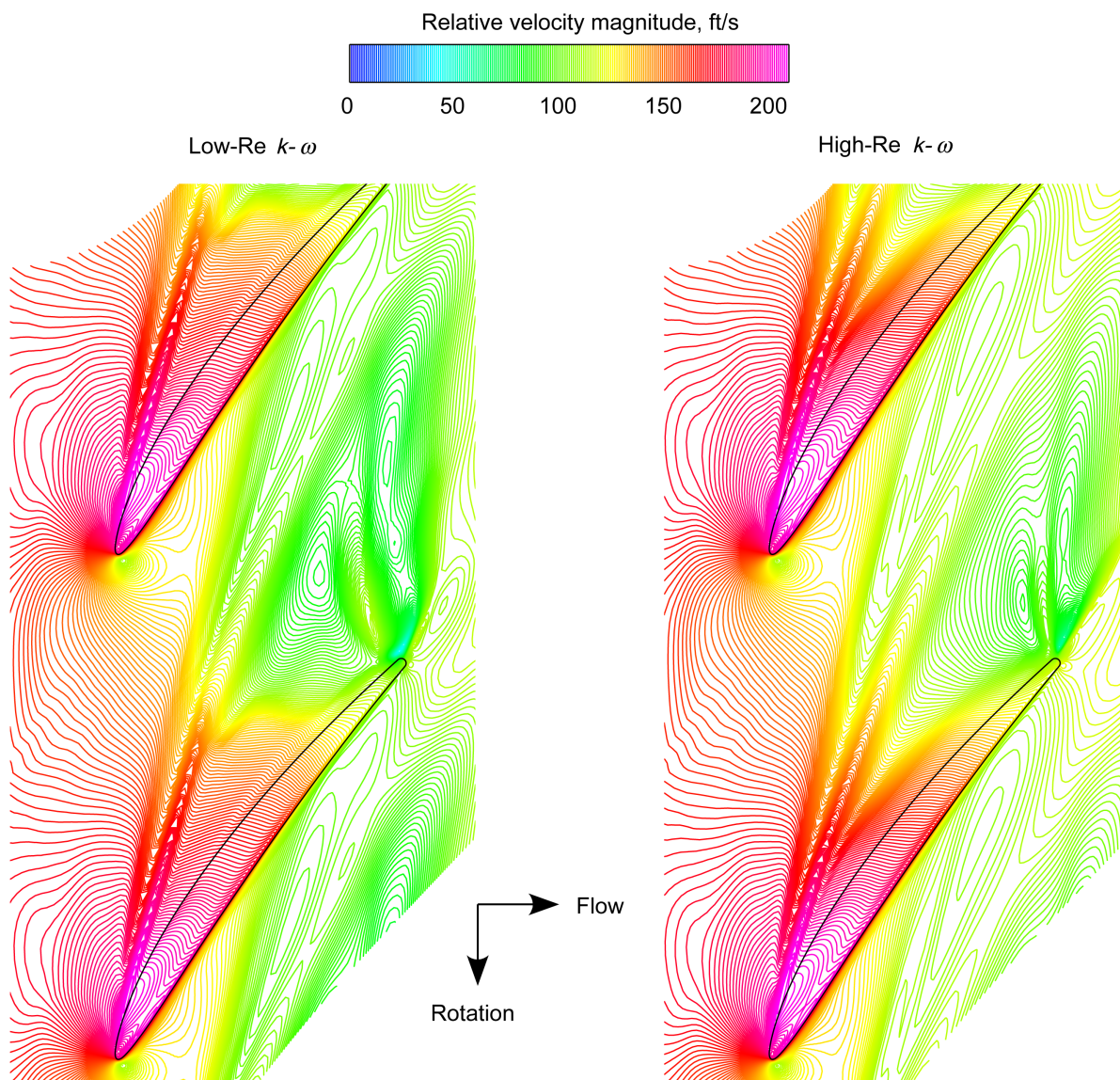


Figure 32(a).—Computed rotor-tip flow field for design operating conditions; relative velocity magnitude; mid-clearance-gap spanwise location.

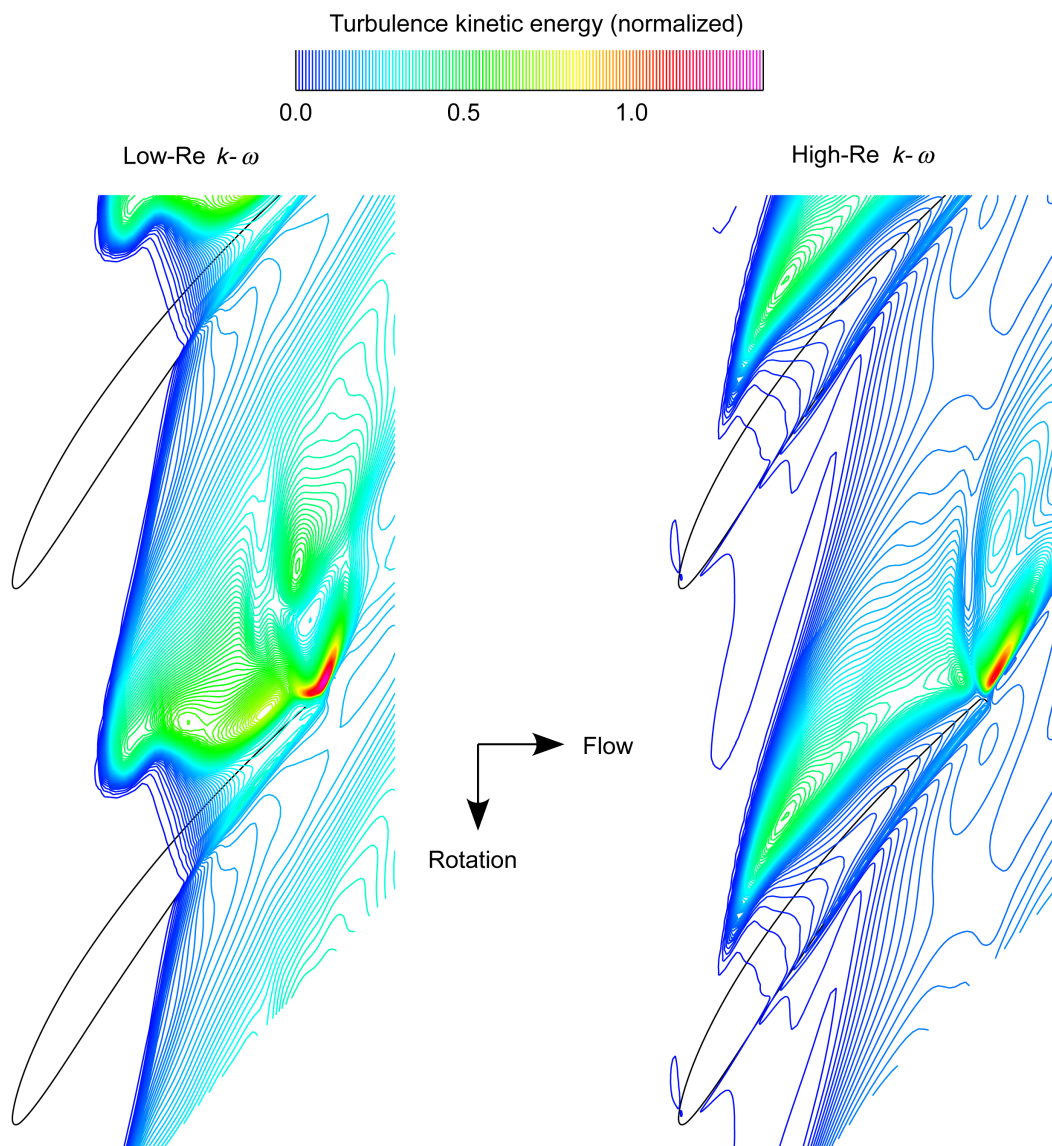


Figure 32(b).—Computed rotor-tip flow field for design operating conditions; turbulence kinetic energy; mid-clearance-gap spanwise location.

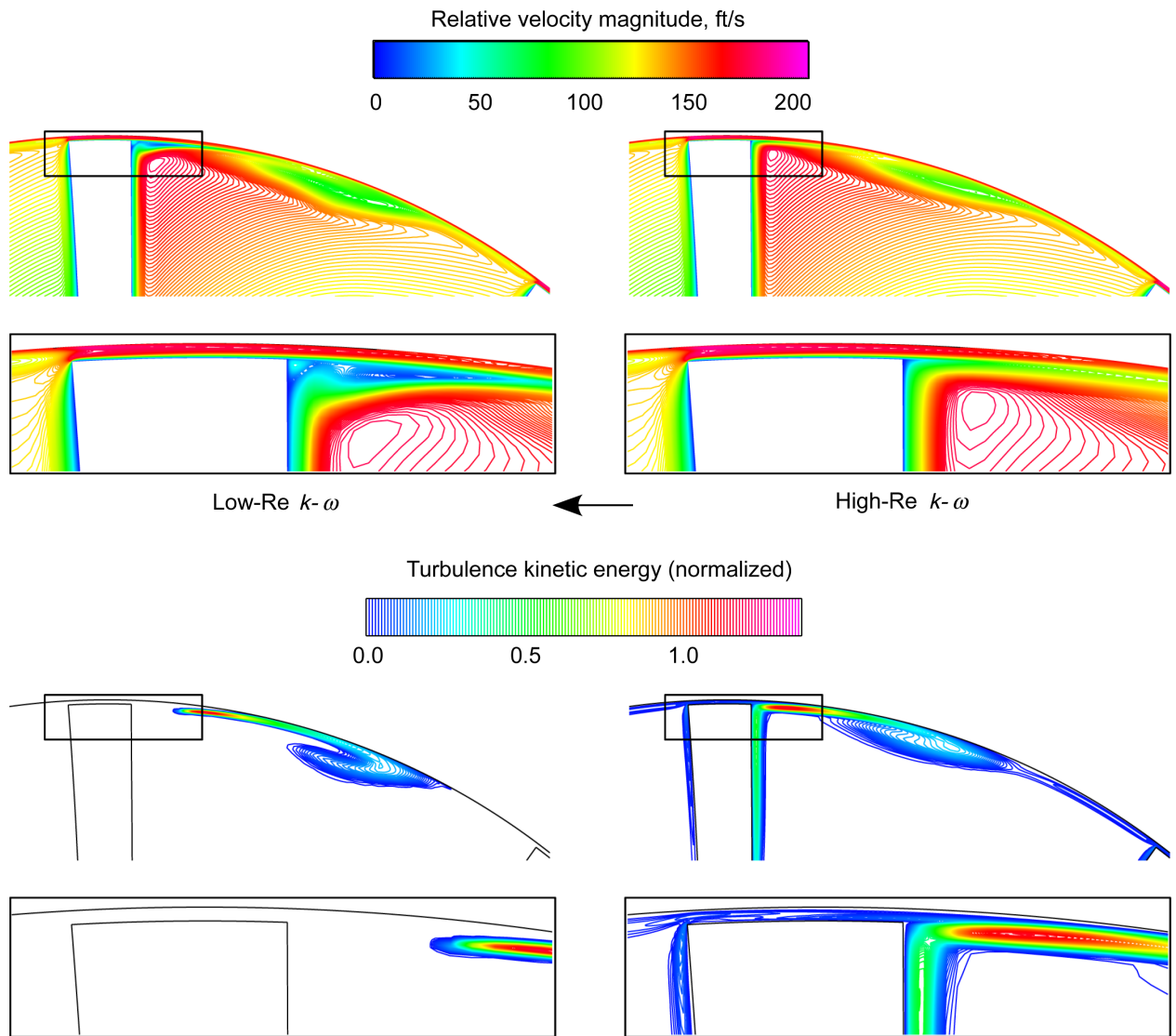


Figure 32(c).—Computed rotor-tip flow field for design operating conditions; mid-chord axial location (axial coordinate -0.700 in.).

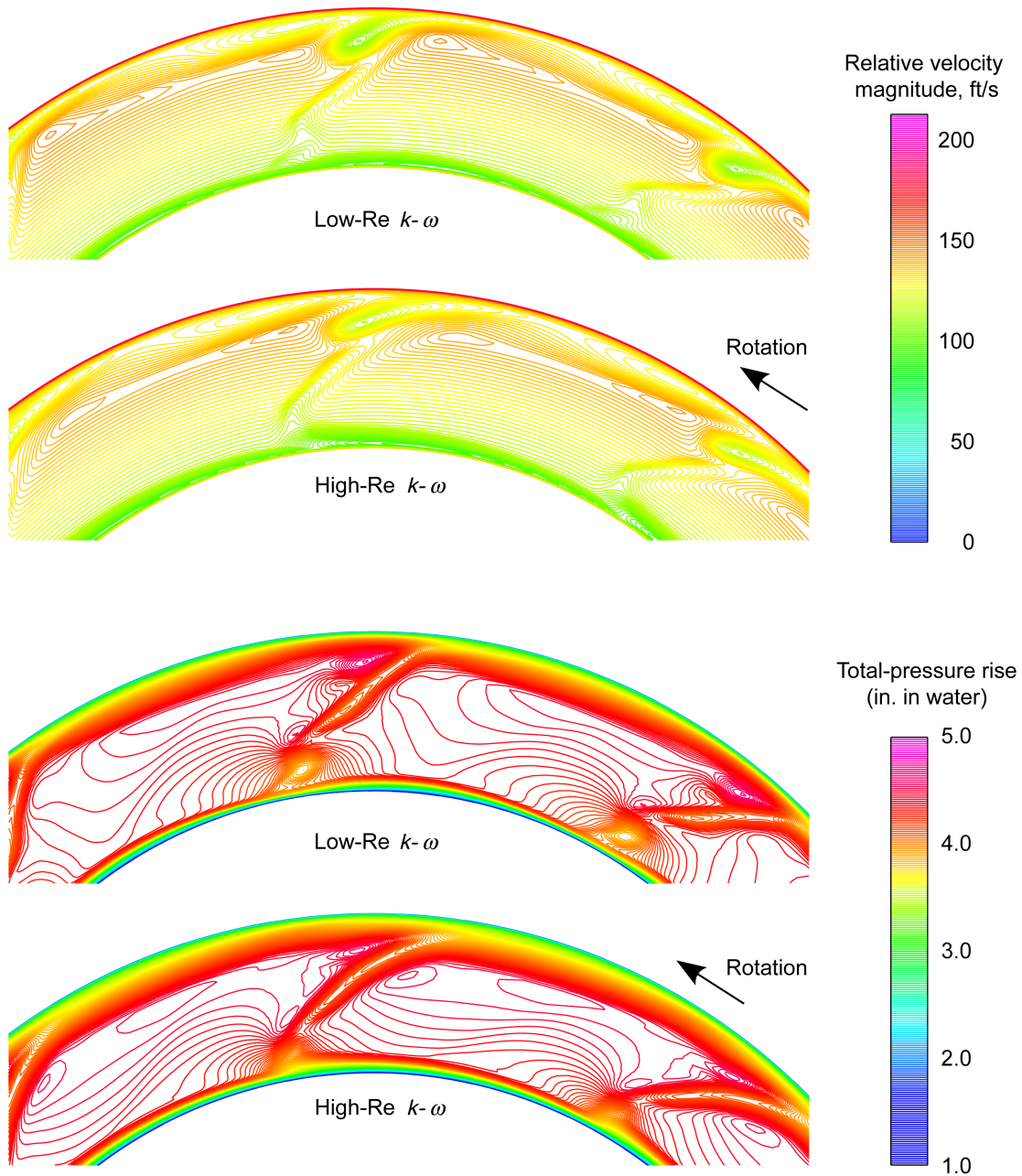


Figure 33(a).—Computed rotor exit flow field for design operating conditions; station 2b.

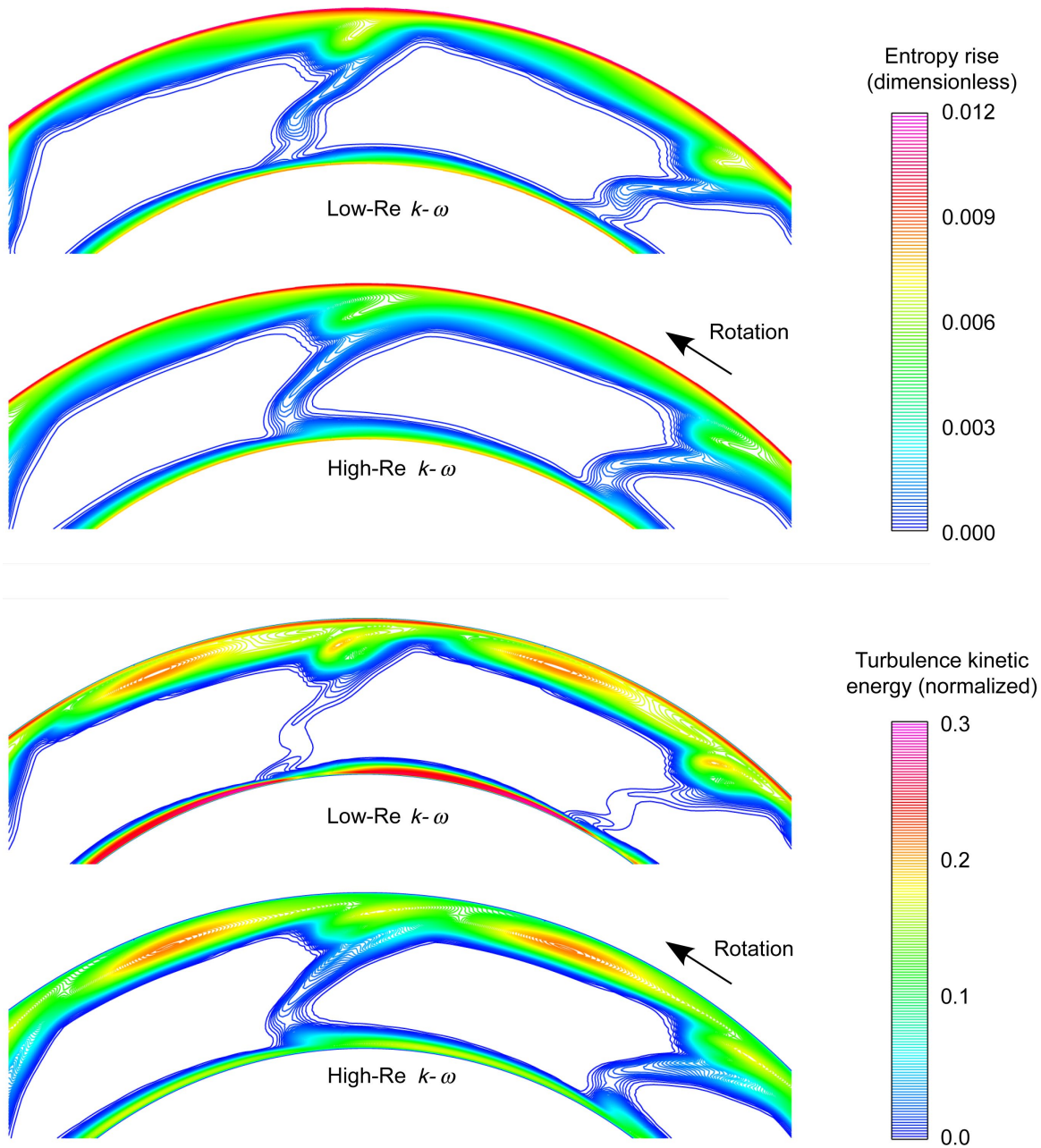


Figure 33(b).—Computed rotor exit flow field for design operating conditions; station 2b.

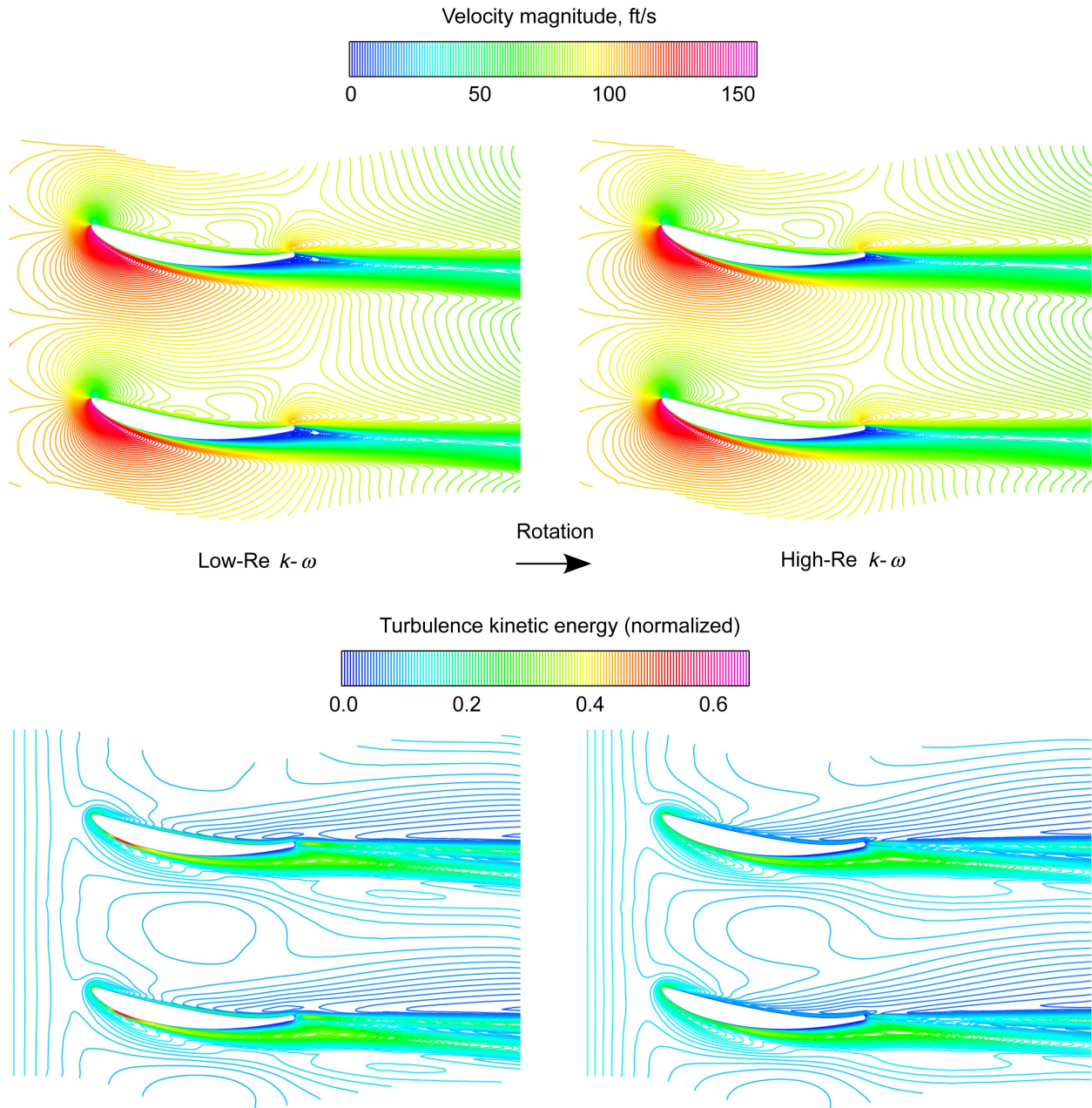


Figure 34(a).—Computed stator flow field for design operating conditions; 85 percent of passage flow.

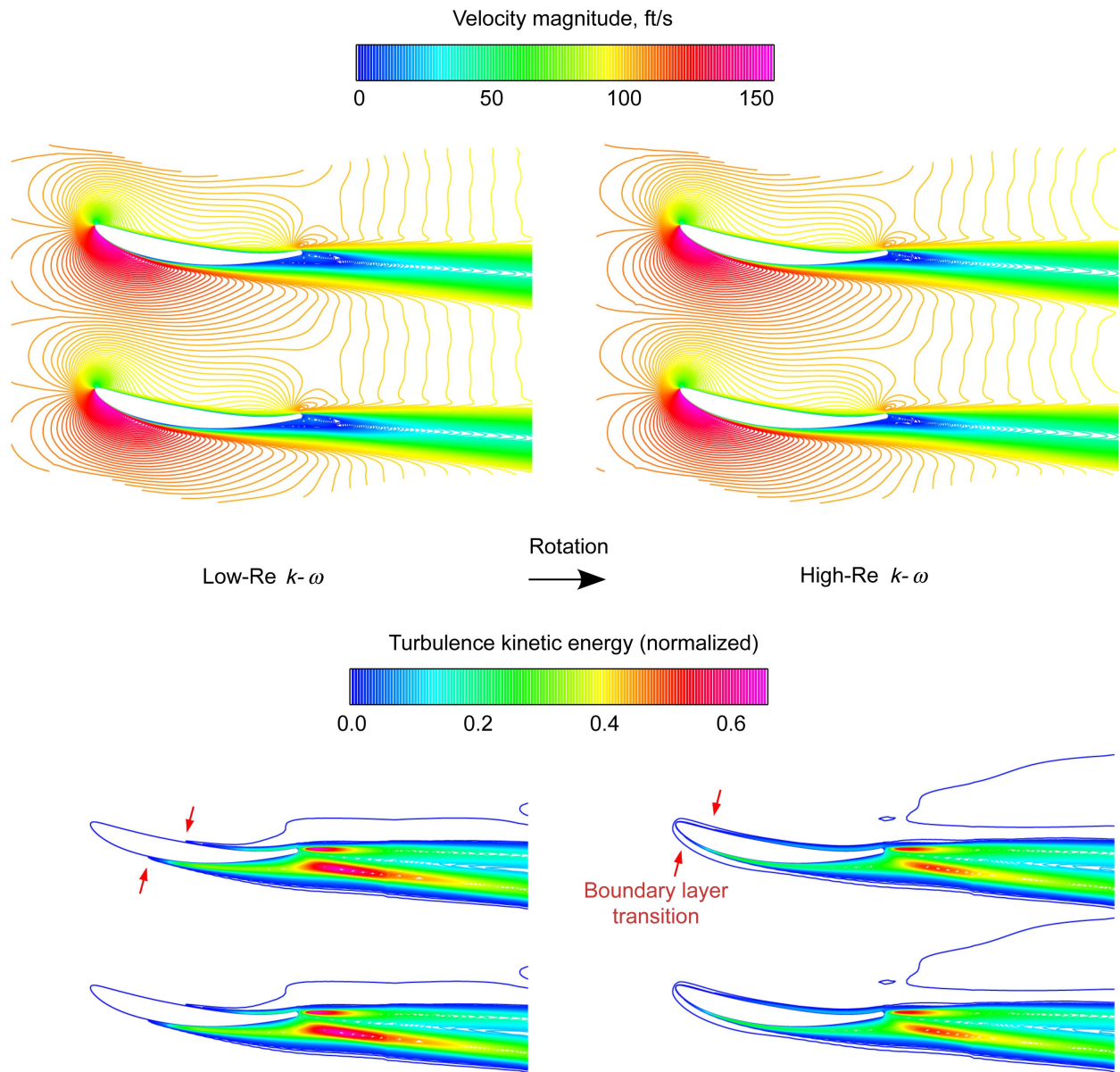


Figure 34(b).—Computed stator flow field for design operating conditions; 50 percent of passage flow.

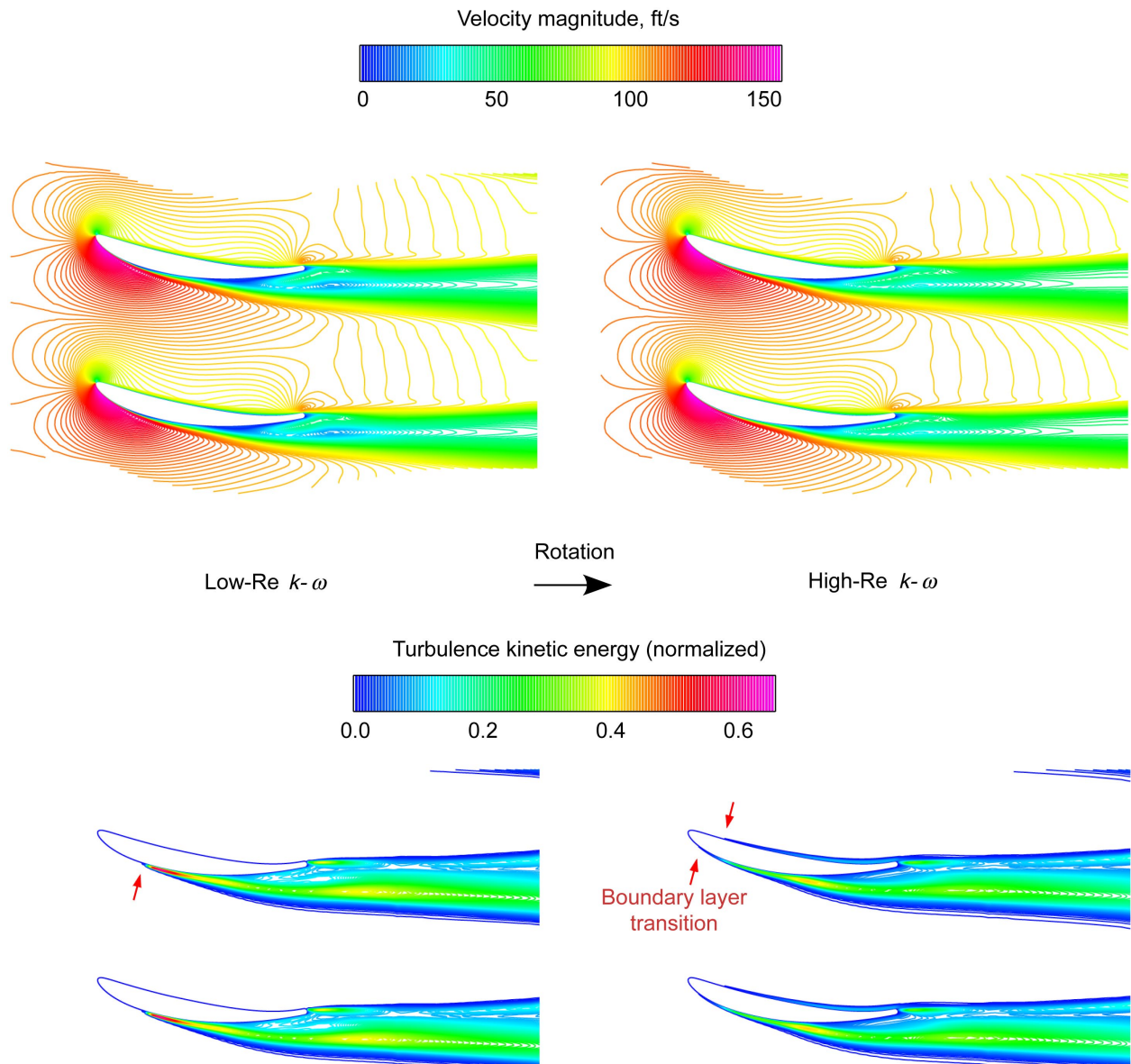


Figure 34(c).—Computed stator flow field for design operating conditions; 15 percent of passage flow.

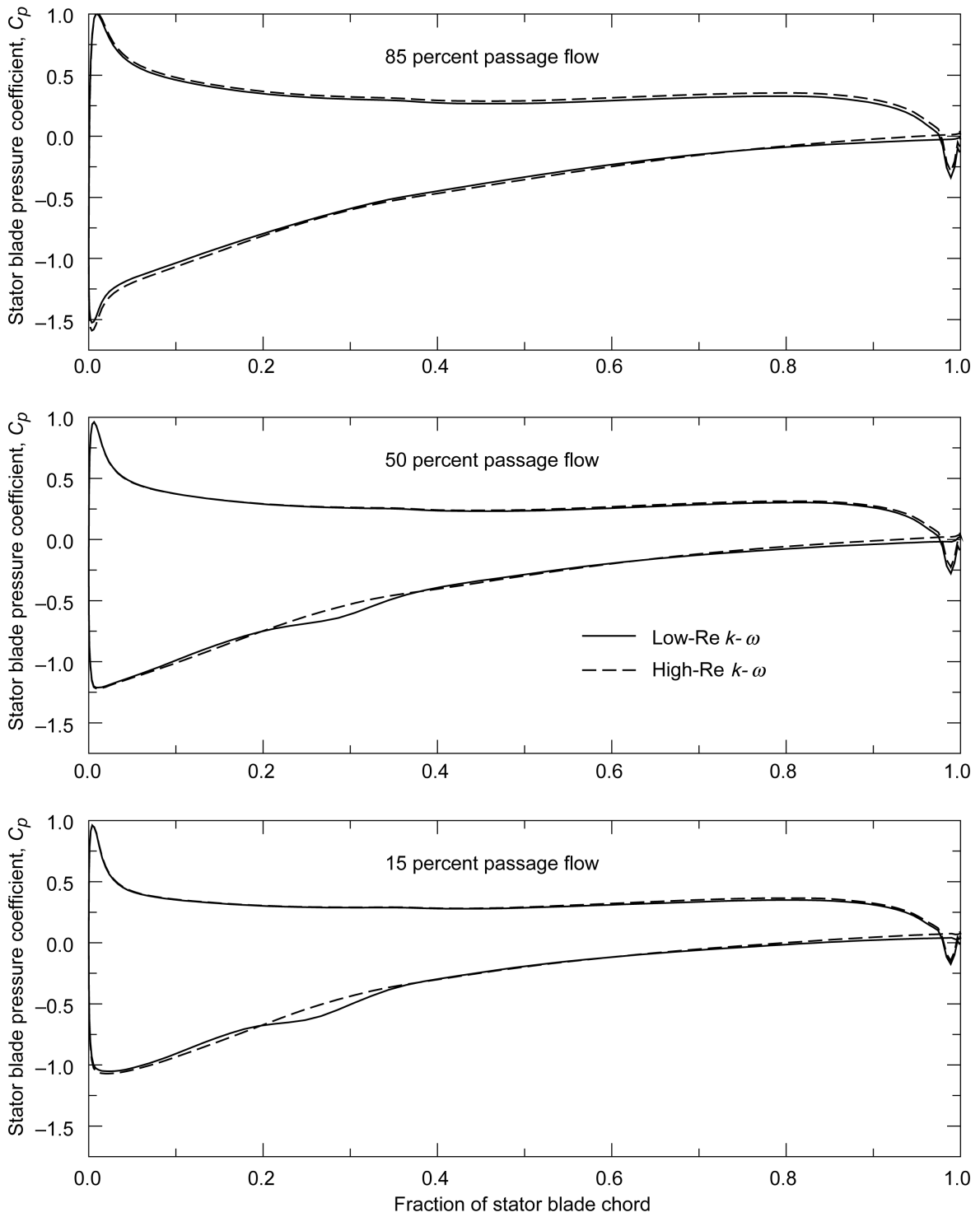


Figure 35.—Chordwise distributions of stator blade surface pressure coefficient.

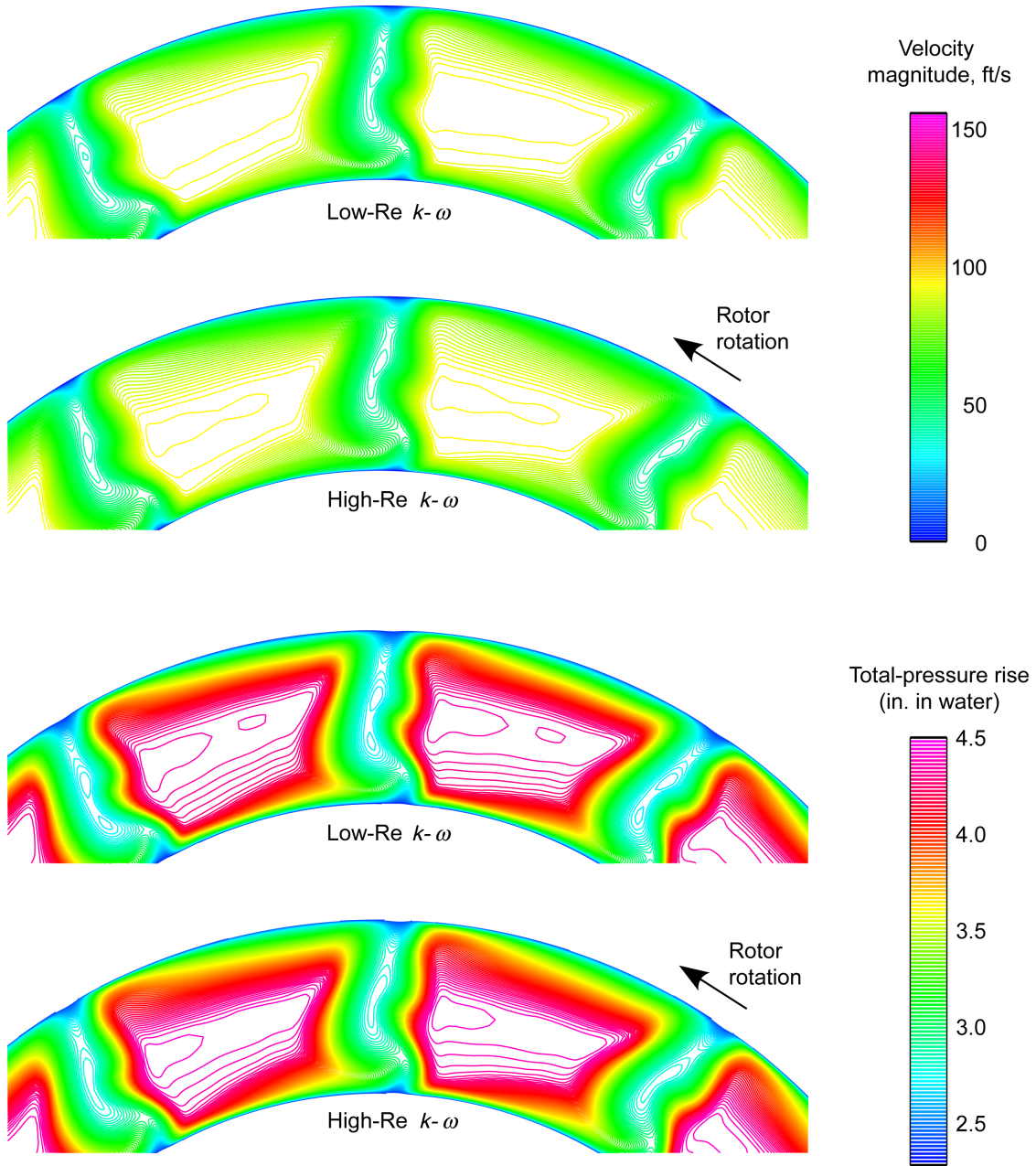


Figure 36(a).—Computed stator exit flow field for design operating conditions; station 3b.

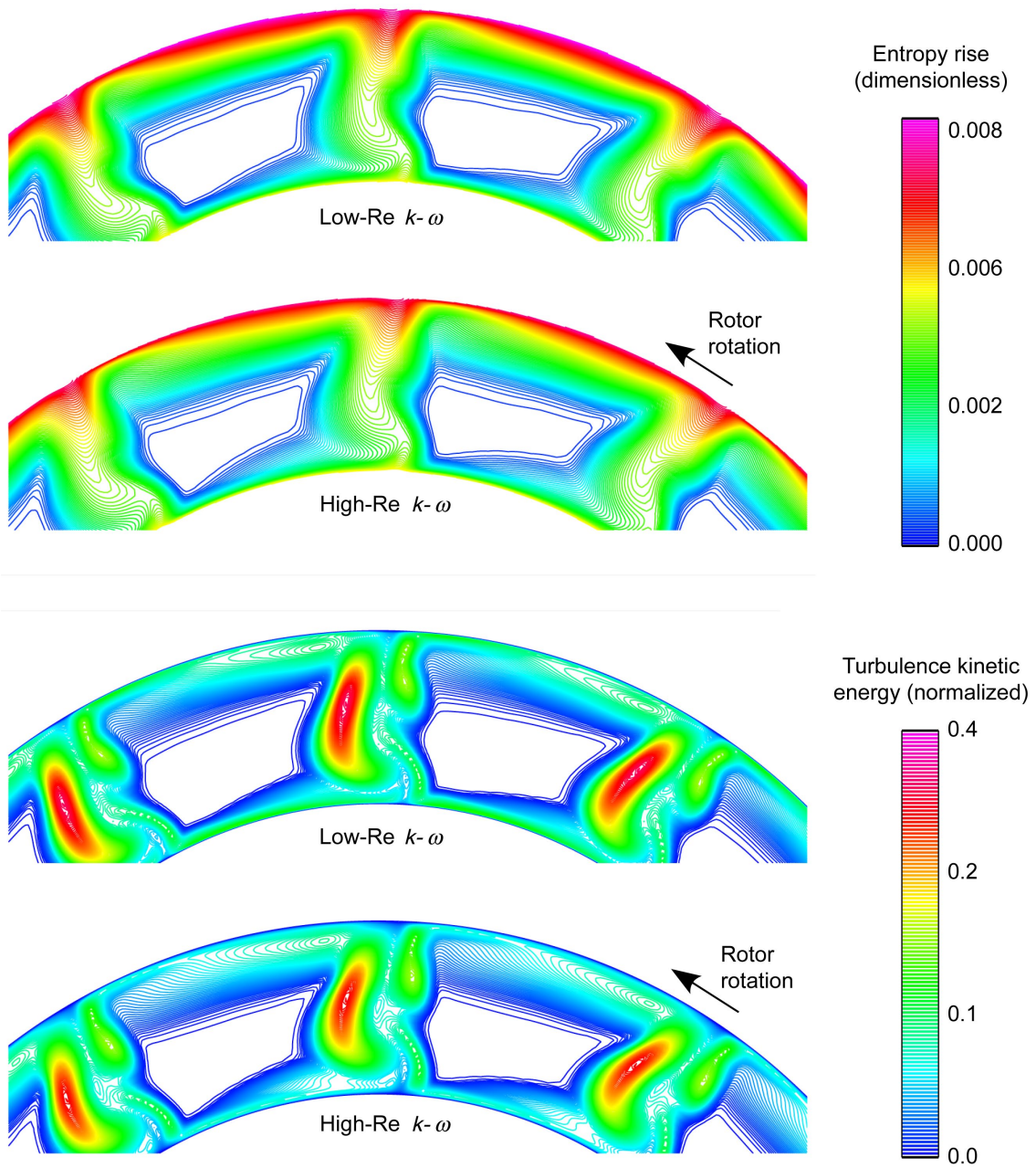


Figure 36(b).—Computed stator exit flow field for design operating conditions; station 3b.

REPORT DOCUMENTATION PAGE			Form Approved OMB No. 0704-0188		
<p>The public reporting burden for this collection of information is estimated to average 1 hour per response, including the time for reviewing instructions, searching existing data sources, gathering and maintaining the data needed, and completing and reviewing the collection of information. Send comments regarding this burden estimate or any other aspect of this collection of information, including suggestions for reducing this burden, to Department of Defense, Washington Headquarters Services, Directorate for Information Operations and Reports (0704-0188), 1215 Jefferson Davis Highway, Suite 1204, Arlington, VA 22202-4302. Respondents should be aware that notwithstanding any other provision of law, no person shall be subject to any penalty for failing to comply with a collection of information if it does not display a currently valid OMB control number.</p> <p>PLEASE DO NOT RETURN YOUR FORM TO THE ABOVE ADDRESS.</p>					
1. REPORT DATE (DD-MM-YYYY) 01-12-2010		2. REPORT TYPE Final Contractor Report		3. DATES COVERED (From - To)	
4. TITLE AND SUBTITLE Aerodynamic Design and Computational Analysis of a Spacecraft Cabin Ventilation Fan			5a. CONTRACT NUMBER NNC06BA07B		
			5b. GRANT NUMBER		
			5c. PROGRAM ELEMENT NUMBER		
6. AUTHOR(S) Tweedt, Daniel, L.			5d. PROJECT NUMBER		
			5e. TASK NUMBER Task 190		
			5f. WORK UNIT NUMBER WBS 439906.04.01.02.02		
7. PERFORMING ORGANIZATION NAME(S) AND ADDRESS(ES) AP Solutions, Inc., 5075 Everton Ave. Solon, Ohio 44139			8. PERFORMING ORGANIZATION REPORT NUMBER E-17263		
9. SPONSORING/MONITORING AGENCY NAME(S) AND ADDRESS(ES) National Aeronautics and Space Administration Washington, DC 20546-0001			10. SPONSORING/MONITOR'S ACRONYM(S) NASA		
			11. SPONSORING/MONITORING REPORT NUMBER NASA/CR-2010-216329		
12. DISTRIBUTION/AVAILABILITY STATEMENT Unclassified-Unlimited Subject Categories: 02 and 71 Available electronically at http://gltrs.grc.nasa.gov This publication is available from the NASA Center for AeroSpace Information, 443-757-5802					
13. SUPPLEMENTARY NOTES					
14. ABSTRACT Quieter working environments for astronauts are needed if future long-duration space exploration missions are to be safe and productive. Ventilation and payload cooling fans are known to be dominant sources of noise, with the International Space Station being a good case in point. To address this issue in a cost-effective way, early attention to fan design, selection, and installation has been recommended. Toward that end, NASA has begun to investigate the potential for small-fan noise reduction through improvements in fan aerodynamic design. Using tools and methodologies similar to those employed by the aircraft engine industry, most notably computational fluid dynamics (CFD) codes, the aerodynamic design of a new cabin ventilation fan has been developed, and its aerodynamic performance has been predicted and analyzed. The design, intended to serve as a baseline for future work, is discussed along with selected CFD results.					
15. SUBJECT TERMS Fans; Aerodynamics; Noise; Performance					
16. SECURITY CLASSIFICATION OF:			17. LIMITATION OF ABSTRACT UU	18. NUMBER OF PAGES 71	19a. NAME OF RESPONSIBLE PERSON STI Help Desk (email:help@sti.nasa.gov)
a. REPORT U	b. ABSTRACT U	c. THIS PAGE U			19b. TELEPHONE NUMBER (include area code) 443-757-5802

